Assessing Colloidal Stability of Pharmaceutical Suspensions with a Shadowgraphic Imaging Method

by

Hui Wang

A thesis submitted in partial fulfillment of the requirements for the degree of

Doctor of Philosophy

Department of Mechanical Engineering

University of Alberta

ABSTRACT

The colloidal stability of pharmaceutical suspensions is an important attribute that needs to be carefully characterized in order to ensure designed product quality. In the field of respiratory drug delivery, pharmaceutical suspensions contained in pressurized metered-dose inhalers (pMDIs) are the most widely used form of medication for the treatment of various airway diseases such as asthma and chronic obstructive pulmonary diseases (COPD). These inherently unstable drug suspensions can destabilize mainly by particle migration and particle agglomeration, which will cause severe problems such as poor consistencies in delivered drug doses, deviated particle size distribution from the optimum respirable range, off-target drug deposition, and so on. This thesis focuses on a newly developed technique for characterizing the colloidal stability of pressurized pharmaceutical suspensions and its application in the development of stable pharmaceutical suspensions.

CHAPTER 1 introduces the dispersed system, the applications of suspensions in the pharmaceutical field, the colloidal stability issues associated with solid suspensions, and the approaches that have been employed for the stabilization of these suspensions.

A shadowgraphic imaging method developed for the colloidal stability characterization of pharmaceutical suspensions, especially pressurized suspensions with relatively poor stability, is introduced in CHAPTER 2. Briefly, the instrument takes sequential shadowgraphic images of samples contained in transparent glass vessels in a bright field, and the images are analyzed for changes in transmission intensity profiles over time. Selected applications demonstrated the instrument's suitability as a routine tester for non-destructive stability monitoring of pressurized pharmaceutical suspensions with a wide range of stability. This technique offers features that are

not currently afforded by any commercially available instruments, namely simultaneous illumination of the complete suspensions, a high image resolution and acquisition rate, and parameters for convenient cross-sample comparison, making this new suspension tester a suitable and reliable instrument for investigating the stability of pressurized pharmaceutical suspensions.

With the developed shadowgraphic imaging technique, how to make meaningful stability measurements becomes important. CHAPTER 3 highlights the important effects of agitation method on the colloidal stability of pharmaceutical suspensions, which has rarely been discussed in the literature. Three different initial agitation methods—wrist action shaking, which simulates the manual shaking motion of pMDI users, vortex mixing, which delivers moderate shear rate, and ultrasonic agitation, which provides the most effective dispersing capability—were tested using different suspension formulations, and the results were compared. A clear dependence of the suspension stability on the employed initial agitation method was observed unanimously for multiple suspension formulations. It is suggested that colloidal stability testing of suspensions must be based on quantified initial agitation energy or at least consistent agitation method. Suspension stability analysis results must also be presented together with a detailed description of the applied agitation method for any measurement of suspension stability to be fully meaningful. As a promising approach forward, a prototyped built-in ultrasonic agitation device was applied to study the colloidal stability of a commercial pMDI, and results with good repeatability were achieved.

With the assistance of the shadowgraphic imaging technique, a systematic study of the effects of particle surface roughness on the colloidal stability of pressurized pharmaceutical suspensions is presented in CHAPTER 4. Effects of surface roughness on the colloidal stability of pressurized pharmaceutical suspensions were isolated and investigated using monodisperse spray-dried particles. A surface-active shell-former, trileucine, was used to produce particles with

different levels of surface roughness. More rugose particles were found to lead to more stable suspensions, and all of them showed better stability than suspensions containing pure trehalose particles with relatively smooth surfaces. Therefore, increasing the surface roughness of particles, for example, by using shell formers like trileucine, is a promising technique that can potentially be used to stabilize their suspensions. Moreover, because this technique is likely not very dependent on the type of propellant and does not require the use of a surfactant, it offers a new means of transitioning to more environmentally friendly pMDIs.

CHAPTER 5 summarizes the main conclusions of this work and suggests possible directions for further investigations.

PREFACE

This thesis is an original work conducted by Hui Wang under the supervision of Dr. Reinhard Vehring and Dr. David Nobes and contains published contents from the following peer-reviewed journal and conference publications.

Journal Publications:

1. **Wang, H.**, Bhambri, P., Ivey, J., Vehring, R., 2017. Design and pharmaceutical applications of a low-flow-rate single-nozzle impactor. *International Journal of Pharmaceutics, 533*(1), 14-25.
2. **Wang, H.**, Barona, D., Oladepo, S., Williams, L., Hoe, S., Lechuga-Ballesteros, D., Vehring, R., 2017. Macro-Raman spectroscopy for bulk composition and homogeneity analysis of multi-component pharmaceutical powders. *Journal of Pharmaceutical and Biomedical Analysis, 141*, 180-191.
3. **Wang, H.**, Tan, P., Barona, D., Li, G., Hoe, S., Lechuga-Ballesteros, D., Nobes, D.S., Vehring, R., 2018. Characterization of the suspension stability of pharmaceuticals using a shadowgraphic imaging method. *International Journal of Pharmaceutics, 548*(1), 128-138.
4. **Wang, H.**, Nobes, D.S., Vehring, R., 2019. Particle surface roughness improves colloidal stability of pressurized pharmaceutical suspensions. *Pharmaceutical Research*, 36(3), 43.

Conference Publications:

5. **Wang, H.**, Tan, P., Barona, D., Li, G., Hoe, S., Lechuga-Ballesteros, D., Nobes, D.S., Vehring, R., 2018. A new shadowgraphic imaging method for the suspension stability analysis of pressurized metered dose inhalers, *Respiratory Drug Delivery*, Tucson, Arizona, US.
6. **Wang, H.**, Nobes, D.S., Finlay, W.H., Vehring, R., 2019. Agitation method affects colloidal stability of pharmaceutical suspensions, *Respiratory Drug Delivery*, Lisbon, Portugal.
7. **Wang, H.**, Nobes, D.S., Finlay, W.H., Vehring, R., 2019. Increasing particle surface roughness as a promising strategy to improve colloidal stability of pharmaceutical suspensions, *Respiratory Drug Delivery*, Lisbon, Portugal.

CHAPTER 1 of this thesis includes contents from the introductory sections of publications 3 (Wang et al., 2018a) and 4 (Wang et al., 2019c). CHAPTER 2 consists of contents from research article 3 (Wang et al., 2018a) and conference proceeding 5 (Wang et al., 2018b). CHAPTER 3 consists of a full version of article 6 (Wang et al., 2019a) and the sections regarding a built-in ultrasonic bath for controlled initial agitation are drawn from research article 3 (Wang et al., 2018a). CHAPTER 4 consists of contents from articles 4 (Wang et al., 2019c) and 7 (Wang et al., 2019b). I was responsible for experimental design, data collection and analysis, and manuscript composition for these articles.

The single-nozzle impactor and associated methodology used in Sections 2.2.3 and 4.2.2 were designed by me and published in article 1 (Wang et al., 2017b) during the period of my Ph.D. studies as a continuation of an M.Sc. project. Their development is not systematically outlined here, but a detailed schematic of the impactor is provided in Appendix III. The macro-Raman system and associated methodology used in Sections 2.2.3 and 4.2.2 were developed by me and the other co-authors of article 2 (Wang et al., 2017a) also during this period. As with the impactor, the development of this system, not being directly related to the main topic of this thesis, is not included here; however, a CAD model is provided in Appendix IV. Interested readers are referred to the respective articles for a more detailed description of the instruments and associated methodologies. The research spray dryer and monodisperse spray drying technique used in Section 3.2.2 and 4.2.2 were developed by fellow graduate students in Dr. Vehring's and Dr. Finlay's research groups.

To my parents Rongxiang She and Laying Wang.

To my sister Wenwen She.

To my wife Jingsi Chen.

ACKNOWLEDGMENTS

This thesis would not have been possible without the help of many individuals.

My foremost gratitude goes to Prof. Reinhard Vehring, who patiently guided me through my graduate studies with not only solid expertise but also great care.

My sincere gratitude goes to Prof. David Nobes for inspiring me with creative ideas of optical instrument design, which made it possible for me to build a unique instrument from scratch.

I am thankful to all my colleagues in the Particle Engineering group, both past and present, for their support in times of need and their willingness to share insights and perspectives. My special thanks to Luba Slabyj.

Financial support in the form of scholarships generously provided by Alberta Innovates - Alberta Advanced Education, the Department of Mechanical Engineering, and Prof. Gerald W. Sadler is gratefully acknowledged.

Resources and facilities provided by the University of Alberta, the National Resource Council of Canada, the Government of Alberta, and AstraZeneca California are also gratefully acknowledged.

TABLE OF CONTENTS

ABSTRACT II

PREFACE V

ACKNOWLEDGMENTS VIII

TABLE OF CONTENTS IX

LIST OF TABLES XII

LIST OF FIGURES XIII

CHAPTER 1 INTRODUCTION 1

1.1. Dispersed System *1*

1.2. Pharmaceutical Suspensions *3*

1.3. Colloidal Stability of Solid Suspensions *4*

1.4. Stabilization of Suspensions *7*

CHAPTER 2 CHARACTERIZATION OF THE SUSPENSION STABILITY OF PHARMACEUTICALS USING A SHADOWGRAPHIC IMAGING METHOD 10

2.1. Introduction *10*

2.2. Materials and Methods *13*

2.2.1. Materials 13

2.2.1.1. Oil-in-water emulsions 13

2.2.1.2. Phospholipid particles 14

2.2.1.3. Pressurized suspensions 15

2.2.2. Suspension tester 16

2.2.2.1. Instrument design 16

2.2.2.2. Data processing 18

2.2.2.3. Uncertainty 22

2.2.3. Methods 25

2.2.3.1. Stability analysis 25

2.2.3.2. Morphological and spectroscopic analysis 25

2.3. Results and Discussion *27*

2.3.1. Determination of HLB of sunflower oil 27

2.3.2. Stability change of spray-dried DSPC suspension during storage 29

2.4. Conclusions *35*

CHAPTER 3 EFFECTS OF AGITATION METHOD ON PHARMACEUTICAL SUSPENSION STABILITY 37

3.1. Introduction *37*

3.2. Materials and Methods *40*

3.2.1. Materials 40

3.2.2. Methods ... 41
3.2.2.1. Monodisperse spray drying ... 41
3.2.2.2. Pressurized suspensions ... 43
3.2.2.3. Suspension stability measurement ... 44
3.2.2.4. Built-in ultrasonic agitation – a prototype ... 45
3.3. Results and Discussion ... 47
3.3.1. Monodisperse spray-dried particles ... 47
3.3.1.1. Morphological analysis ... 47
3.3.1.2. Particle size distribution ... 48
3.3.2. Effects of agitation methods ... 50
3.3.2.1. Suspension stability comparison by transmission profiles ... 50
3.3.2.2. Suspension stability comparison by instability index curves ... 52
3.3.2.3. Formulation and agitation dependent suspension stability ... 54
3.3.3. Built-in ultrasonic agitation for stability measurement ... 57
3.4. Conclusions ... 60
CHAPTER 4 PARTICLE SURFACE ROUGHNESS IMPROVES COLLOIDAL STABILITY OF PRESSURIZED PHARMACEUTICAL SUSPENSIONS ... 62
4.1. Introduction ... 62
4.2. Materials and Methods ... 64
4.2.1. Materials ... 64
4.2.2. Methods ... 65
4.2.2.1. Monodisperse spray drying ... 65
4.2.2.2. Particle design ... 66
4.2.2.3. Morphological and spectroscopic analysis ... 69
4.2.2.4. Particle size measurement ... 70
4.2.2.5. Specific surface area measurement ... 71
4.2.2.6. Pressurized suspensions ... 73
4.2.2.7. Suspension stability measurement ... 73
4.3. Results and Discussion ... 75
4.3.1. Morphological and spectroscopic analysis ... 75
4.3.2. Size distributions of spray-dried particles ... 80
4.3.3. Specific surface area analysis ... 85
4.3.4. Effects of particle size on the suspension stability ... 88
4.3.5. Improved suspension stability with surface modification ... 92
4.4. Conclusions ... 97
CHAPTER 5 CONCLUSIONS ... 99
5.1. Main Conclusions ... 99
5.2. Future Work ... 100

BIBLIOGRAPHY 102
APPENDICES 115
Appendix I Suspension Tester Design 115
I.1. Hardware 115
I.2. Custom-made components 118
I.3. Cable connection 123
Appendix II Calibration of Transmission Intensity 125
Appendix III Single-Nozzle Impactor Used for pMDI Particle Extraction 127
Appendix IV Macro-Raman Spectroscopy System 128
Appendix V Suspension Imaging Software 131
V.1. LabVIEW Front panel – Suspension Imaging 131
V.2. LabVIEW Block diagram – Suspension Imaging 134
V.3. Post-data processing 152

LIST OF TABLES

Table 1.1. Classification of dispersed systems based on the physical state of the interacting phases. 1

Table 2.1. Composition of prepared emulsions with surfactant mixtures of varying HLB values. 14

Table 2.2. Parameters used for spray drying of DSPC particles. 15

Table 2.3. Specifications and actual experimental settings of the suspension tester. 17

Table 3.1. Suspension formulations used for colloidal stability testing. Particle settling velocities (v_S) were calculated based on the measured aerodynamic particle sizes and propellant properties at 20 °C. 41

Table 3.2. Methods and settings used for initial agitation of suspensions. "Osc/min" stands for oscillation per minute; "RT" stands for room temperature. 45

Table 4.1. Parameters used for monodisperse spray drying. 65

Table 4.2. Feed solutions for monodisperse spray drying with calculated time for trileucine to reach surface saturation normalized by droplet lifetime, time for trehalose to reach true density normalized by droplet lifetime, and calculated true density of the mixture. 69

Table 4.3. Comparison of particle size distributions measured using different methods. 83

Table 4.4. Data used for the determination of particle specific surface area and BET constant. 86

Table I.1. Components used for the suspension tester. 116

Table IV.1. Key components in the excitation chamber of the macro-Raman spectroscopy 129

LIST OF FIGURES

Figure 1.1. Size-based classification of the dispersion systems in liquid with typical properties and examples within each size domain. Colloidal dispersion lies in the range between molecular and coarse dispersion. 2

Figure 2.1. CAD model of the new suspension tester for stability analysis of pressurized pharmaceutical suspensions. This instrument takes sequential shadowgraphic images of suspension samples at pre-determined settings such as frame rate, duration, exposure time, etc. 17

Figure 2.2. First step of shadowgraphic image processing: extraction of absolute transmission profiles, $T^{a}_{t,h}$, from the sequential shadowgraphic images. 18

Figure 2.3. Second step of the data processing: calculating the change of transmission intensity relative to the initial transmission profile. The initial relative transmission profile is a straight line at the transmission intensity of 0. 19

Figure 2.4. Normalization of the relative transmission profiles by its maximum possible value. 20

Figure 2.5. Transmission intensity map for different combinations of light source power in ampere and camera exposure time in milliseconds. The plot demonstrates a good linearity of the light intensity on the exposure time. 21

Figure 2.6. Derivation of the instability index, $\sigma(t)$, by integrating the normalized relative transmission profiles. ...22

Figure 2.7. A typical combination of camera exposure time (0.1 ms) and LED output power (1.0 A) was used to acquire the shadowgraphic images for 15 minutes. Relative intensity profiles show stable detectable light intensity by the camera with < 3% overall intensity fluctuation. 24

Figure 2.8. Bias error of the derived instability index caused by the fluctuation of the light intensity is demonstrated to be negligible (< 0.004) when the LED and camera were operated at 1.0 A and 0.1 ms respectively. 24

Figure 2.9. Normalized relative transmission profiles show different destabilization processes of emulsions prepared with surfactants of varying HLB values. Clarification and creaming are observed in all three cases. Direction of gravity is indicated by vector $\boldsymbol{g}$. 27

Figure 2.10. Instability indices σ (t = 3 h) for emulsions prepared with surfactants of varying HLB values. The most stable emulsion was achieved when the surfactant HLB matched the required HLB of oil between 6.5 and 7.5. Inset shadowgraphic images represent end state of the emulsions after 3 hours of settling. Intensity of each pixel is represented by different colors according to the color bar. 29

Figure 2.11. Normalized relative transmission profiles of the pressurized DSPC suspension changed significantly within the first 5 days after propellant filling. Level of clarification and thickness of the cream layer increased gradually. 30

Figure 2.12. The different instability index plots show significantly different destabilization processes in the DSPC suspension. Insets are the shadowgraphic images recorded at days 0, 2, 3 and 5 by the end of each stability measurement. Pixel intensities varied from 0 to 4096 as represented by the different colors from blue to red. .31

Figure 2.13. This figure shows the final instability indices σ (t = 15 min) for measurements at different time points of the aging study. The trend of the plot indicates a significant drop in suspension stability during the study. .32

Figure 2.14. SEM images of DSPC particles extracted from the fresh (a – b) and the aged (c – d) suspensions show significantly different morphologies and dimensions. 33

Figure 2.15. Raman spectra of fresh (t = 0 d) and aged (t = 5 d) DSPC particles compared to the more ordered DSPC standard precipitated from its ethanolic solution indicate increased solid phase order during aging of the suspension. Spectra are offset vertically for comparison purpose. 35

Figure 3.1. Schematic of the monodisperse micro-jet atomizer. The piezoelectric ceramic ring introduces vibration to the atomizer and forces the micro-jet to disintegrate regularly to monodisperse droplets. Dispersing gas supplied through the orifice cap prevents droplets from colliding into doublets or triplets. 42

Figure 3.2. Schematic layout of the new suspension tester with the built-in ultrasonic agitation device. 46

Figure 3.3. Monodisperse spray-dried trehalose and lactose particles show good uniformity and are spherical as expected. 47

Figure 3.4. Aerodynamic size distributions of the spray-dried trehalose and lactose particles show high monodispersity with narrow distributions (GSD < 1.2) and similar particle diameters. 48

Figure 3.5. Cumulative volume equivalent diameter distributions of the spray-dried trehalose and lactose particles measured directly from the SEM images based on more than 450 particles. 49

Figure 3.6. Normalized relative transmission profiles for different combinations of suspension formulation and applied agitation method. 51

Figure 3.7. Instability index plot, $\sigma(t)$, for different combinations of suspension formulation and applied agitation method. 53

Figure 3.8. Time for the instability index to reach 0.5, τ (σ = 0.5), plotted against the agitation method for different suspension formulations. Inset shadowgraphic images show the states of the suspensions after 5-minute observation. 55

Figure 3.9. Time for the instability index to reach 0.5, τ (σ = 0.5), plotted against particle setting velocity/propellant for different agitation methods. Inset shadowgraphic images show the states of the suspensions after 5-minute observation. 56

Figure 3.10. Normalized relative transmission profiles of pressurized suspension from a commercial pMDI show different stabilities when agitated differently. 58

Figure 3.11. Instability index plot for analysis of commercial pMDI suspension after wrist-action shaking and ultrasonic agitation. Inset shadowgraphic images represent different end states of the suspension. 59

Figure 4.1. Morphology of the spray-dried pure trehalose particles shows a high level of sphericity and good monodispersity. Particle size increased with the feed solution concentration. 76

Figure 4.2. Morphology of the monodisperse spray-dried particles gradually changed from smooth to highly rugose when the concentration of trileucine was increased from 0% to 5.0%. 77

Figure 4.3. Images of particles extracted from the propellant showing no significant changes of morphology. 78

Figure 4.4. Reference spectra of crystalline trehalose (c-Tre), amorphous trehalose (a-Tre), crystalline trileucine (c-Leu_3), and amorphous trileucine (a-Leu_3). The bottom trace is a residual spectrum (Res.) arrived at by subtracting amorphous trehalose from the spectrum of trileucine-modified trehalose particles (95.0%Tre-5.0%Tri), proving the amorphous state for both trehalose and trileucine. 80

Figure 4.5. Aerodynamic size distributions of the spray-dried trehalose particles show high monodispersity with narrow distributions (*GSD* < 1.2). The corresponding *MMAD* increased from 6.0 μm to 15.5 μm with increasing feed solution concentrations. 81

Figure 4.6. Cumulative volume equivalent diameter distributions of the spray-dried trehalose particles measured directly from the SEM images. The results agree well with the aerodynamic diameter distributions measured by the aerodynamic particle sizer. 83

Figure 4.7. Particle size distributions of the spray-dried trehalose-trileucine particles show high monodispersity for formulations with different trileucine mass fractions. The mass median aerodynamic diameters decreased slightly due to the increased particle rugosity caused by the increase in trileucine mass fraction from 0% to 5.0%. 84

Figure 4.8. Linear region of the krypton adsorption isotherm used for the determination of specific surface area and BET constant. 85

Figure 4.9. Surface rugosity ($f_r = A_r / A_g$) of the monodisperse spray-dried particles increased gradually as more trileucine was added to the feed solution. Insert table shows the real and geometric specific surface area used for the calculation of rugosity. Dotted base-line corresponds to a rugosity of 1.0 for perfectly smooth and spherical particles. 87

Figure 4.10. Normalized relative transmission profiles of the pressurized suspensions indicate that suspension stability strongly depends on the diameter of suspended particles. The suspension with large particles destabilized much more and much faster than those with smaller particles. 89

Figure 4.11. Instability index plots for suspensions of different trehalose particles show that larger particles lead to faster destabilization of the corresponding suspension. 90

Figure 4.12. Comparison of the final instability indices at 30 min, σ (t = 30 min), for different suspensions shows a strong dependence of suspension stability on particle diameter. Three independent suspension samples were prepared for each group of particles, and each suspension was measured three times for its suspension stability. Inset shadowgraphic images represent end state of the suspension after 30 minutes measurement. 91

Figure 4.13. Normalized relative transmission profiles indicate a slower destabilization process as more trileucine is added to the formulation and the suspended particles become more wrinkled. 93

Figure 4.14. Instability index plot for suspensions of particles with different rugosity show that the increased surface roughness by trileucine improves suspension stability and reduces the rate of the destabilization process. 94

Figure 4.15. Instability indices σ (t = 30 min) for suspensions with particles of different rugosity. The suspension stability improves as the particles become more wrinkled. Inset shadowgraphic images represent end state of the suspension after 30 minutes measurement. 95

Figure I.1. CAD model of the suspension tester with indexed component numbers. 115
Figure I.2. CAD drawing for the front door of the light-proof sample chamber. 118
Figure I.3. CAD drawing for the side wall of the light-proof sample chamber for the LED panel installation. 119
Figure I.4. CAD drawing for the side wall of the light-proof sample chamber with an optical window for the camera lens. 120
Figure I.5. CAD drawing for the top cover of the light-proof sample chamber. 121
Figure I.6. CAD drawing for the custom-made transparent ultrasonic bath for the controlled initial sample agitation. 122
Figure I.7. Schematic diagram of the suspension tester showing the connection of the power and data cables. The inset shows the configuration of the connector for triggering signal input. 123
Figure II.1. Slopes of the transmission intensity vs. exposure time curves in **Figure 2.5** shows a linear dependence on the applied LED power. 125
Figure II.2. Intercepts of the transmission intensity vs. exposure time curves in **Figure 2.5** shows a linear dependence on the applied LED power. 126
Figure III.1. A single-stage configuration of the single-nozzle impactor for extracting particles from pMDIs for spectroscopic and morphological analysis. 127
Figure IV.1. CAD model for the custom-built macro-Raman spectroscopy system. 128
Figure IV.2. Front and side view of the dispersive macro-Raman system signal collection chamber (dimension in millimeter). 129
Figure V.1. The Suspension Imaging software interface for data acquisition. 132
Figure V.2. The Suspension Imaging software interface for data processing. 133
Figure V.3. Fitting of the instability index plots with a hill function. The red fitting curves overlap very well with the measured instability index data points. 152
Figure V.4. Fitting parameters of the hill function. 153
Figure V.5. The front panel of the SI_Data_Analysis GUI code for post data processing. 154

CHAPTER 1 Introduction

1.1. Dispersed System

A dispersed system–also known as a dispersion system–is usually defined as a heterogeneous multiphase system consisting of phase I dispersed throughout another continuous phase II (Cosgrove, 2010; Lieberman et al., 1996). Depending on the physical state of the mixed phases, the dispersed systems can be classified into multiple categories as listed in **Table 1.1** (Hunter, 2001). Each of the dispersion systems has been studied extensively in the literature and has formed the basis for well-developed disciplines (Babick, 2016; Hinds, 2012; Leal-Calderon et al., 2007; Stevenson, 2012). However, it is the sol system, which features particulate matter as the dispersed phase I and liquid as the dispersing phase II, that falls within the scope of the present study and is considered here.

Table 1.1. Classification of dispersed systems based on the physical state of the interacting phases.

Dispersed Phase (I) → Dispersing Phase (II) ↓	**Gas**	**Liquid**	**Solid**
Gas	-	Liquid Aerosol e.g. cloud, mist	Solid Aerosol e.g. dust, smoke
Liquid	Foam e.g. soda pop, whipped cream	Liquid Emulsion e.g. milk, blood, oil-in-water	**Sol** e.g. paints, suspensions
Solid	Solid Foam e.g. lava, pumice, foamed alloy	Solid Emulsion e.g. cold cream, cheese	Solid Sol e.g. alloy, carbon steel

Dispersion systems with a liquid dispersing phase can be further classified according to the size of the dispersed phase I as shown in the schematic in **Figure 1.1** (Kulshreshtha et al., 2010). Stable and homogeneous solutions in the form of molecular dispersion are achieved when the

dispersed particulate matter approaches the size of individual molecules in the nanometer to sub-nanometer range (Huang and Dai, 2014). Relatively heterogeneous and unstable coarse dispersions as suspensions or emulsions are obtained when the dispersed phase becomes coarse particles or droplets in the size range of larger than tens of micrometers. Colloidal dispersions, where multiple disciplines cross paths, bridge the nanometer and the micrometer range of the dispersed phase and have been a research hotspot for the past few decades (Cosgrove, 2010; Israelachvili, 2011). Despite the various classifications, the boundaries between these systems are becoming increasingly difficult to define with the ongoing development of such novel dispersed systems as nanosuspensions (Rabinow, 2004) and colloids of macromolecules (Janes et al., 2001).

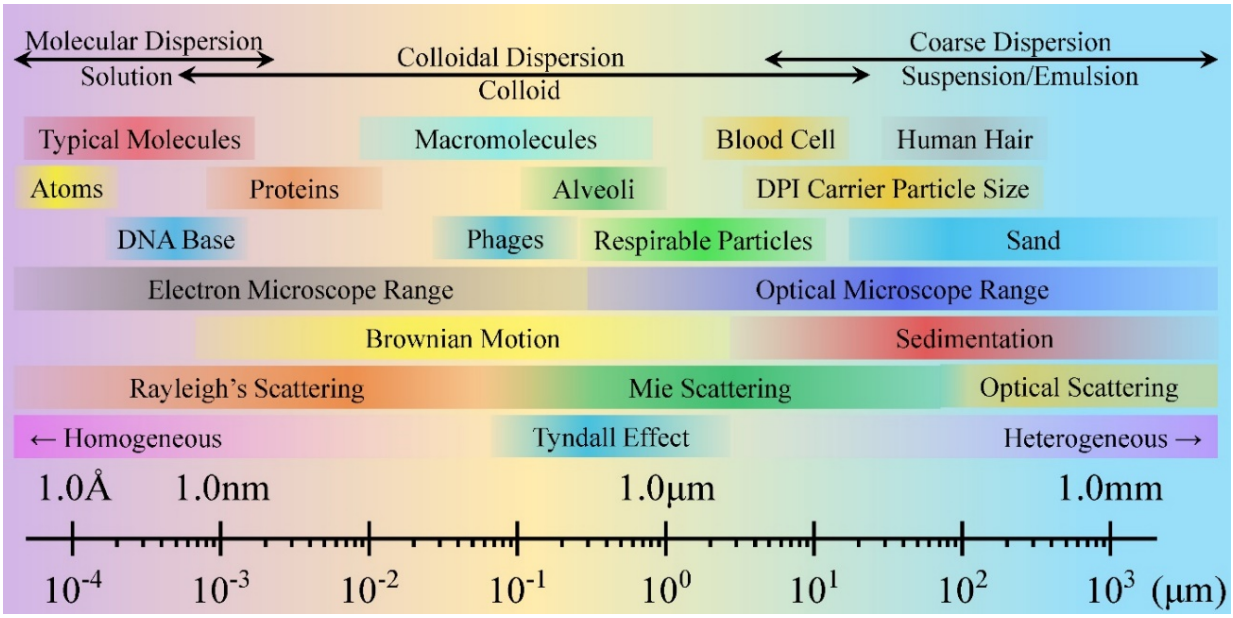

Figure 1.1. Size-based classification of the dispersion systems in liquid with typical properties and examples within each size domain. Colloidal dispersion lies in the range between molecular and coarse dispersion.

1.2. Pharmaceutical Suspensions

Suspensions consisting of solid particles dispersed in a continuous liquid phase have been widely used for drug delivery purposes for various reasons. One of them is that the insolubility of pharmaceutical active ingredients, which has emerged as one of the most challenging issues in the development of new formulations and which can affect the formulation stability and also lead to poor drug bioavailability, can now be circumvented by using solid dispersions (Kipp, 2004; Vasconcelos et al., 2007). The solid suspension system has also been proven to be a good platform for drug loading and controlled drug release (Huang et al., 2006; Müller et al., 2000). The suspensions may also be designed with the addition of excipients to control dissolution rate in physiological conditions, with the intent to decrease variability in dissolution and absorption, improve bioavailability, or extend drug delivery (Patravale and Kulkarni, 2004; Vasconcelos et al., 2007). Solid drug suspensions are now available in various forms such as oral suspensions, pulmonary dosage forms, and injectables (Kulshreshtha et al., 2010; Nielloud, 2000).

Among the various forms of pharmaceutical suspensions, drug particles suspended in pressurized liquids gained its popularity in the field of respiratory drug delivery. This form of medication is ideal for regionally targeted drug delivery in the human respiratory system because the drug particles can come into direct contact with the airway upon aerosolization and inhalation (Heyder, 2004; Kleinstreuer et al., 2008). Pressurized metered dose inhalers (pMDIs) containing pharmaceutical suspensions are the most widely prescribed form of medication for the treatment of airway diseases such as asthma and chronic obstructive pulmonary disease (Ooi et al., 2015). A pMDI device consists of a metering valve that connects a fixed-volume metering chamber, which is typically filled with a drug suspension, to the environment, releasing a burst of fast-evaporating suspension droplets when actuated. Instantly dried respirable particles typically have aerodynamic

diameters in the range of 1 – 5 μm and can be inhaled directly into the deep lung (Myrdal et al., 2014). The pressurized pharmaceutical suspension is the subject of the present study and will be discussed in depth, but many of the concepts presented here can be universally applied to other suspension systems.

1.3. Colloidal Stability of Solid Suspensions

Stable drug suspensions are almost always desirable for pharmaceutical applications. However, stability issues associated with pharmaceutical suspensions are frequently encountered and can be grouped into two general categories: chemical and physical. Chemical stability issues for solid drug suspensions refer to chemical reactions and degradations of the suspended material and are usually drug-specific (Waterman and Adami, 2005). Due to the limited solubility of drug particles in the liquid phase, chemical stability of pharmaceutical suspensions is usually less of a concern when compared to their physical stability issues (Wu et al., 2011).

The common physical stability–also referred to as colloidal or suspension stability–issues of the solid suspensions, including particle migration by creaming or sedimentation and particle size change by agglomeration, are considered here (Ooi et al., 2015; Wu et al., 2011). Other physical stability issues such as particle growth by Ostwald ripening (Verma et al., 2011), solid state transition between amorphous and crystalline forms as well as between different polymorphs (Wang et al., 2013), and change of particle morphologies (Raghavan et al., 2003) are also briefly discussed from time to time but do not constitute a major research subject of the current study.

Suspensions with poor colloidal stability in pharmaceutical applications can cause serious issues. For example, in respiratory drug delivery, collective particle migration can lead to large variations between drug doses delivered from the metering valve (Ivey et al., 2015; Stein et al.,

2014), while particle aggregation can cause the size distribution of suspended drug particles to deviate from the optimum respirable range towards the larger end and eventually affect both the amount and the site of drug deposition in the airways (Finlay, 2001; Myrdal et al., 2014). It has also been demonstrated in the literature that the dose uniformity of pMDIs can be directly related to the stability of applied drug suspensions (Ivey et al., 2015). This colloidal stability issue is the exact reason why patients prescribed pMDI medications are instructed to shake the canisters 'vigorously' before actuation and why failure to do so accounts for most of the incorrect use of inhalation devices (Arora et al., 2014). Similar issues arise in other drug delivery systems using suspensions; for example, in injectables, the suspensions must be stable after reconstitution to achieve the designed therapeutic efficacy.

Particle migration by upward creaming or downward sedimentation is caused by buoyancy due to the density difference between the particles and the liquid in which they are suspended. The settling velocity of an individual particle, v_s, with a volume equivalent diameter of d_{ve} or an aerodynamic diameter of d_a can be described by Stokes' law as (DeCarlo et al., 2004):

$$v_s = \frac{(\rho_P - \rho_F)g}{18\mu\chi} d_{ve}^2 = \frac{(\rho_T - \rho_F)(1-\phi)g}{18\mu\chi} d_{ve}^2 = (1 - \frac{\rho_F}{\rho_T}) \frac{\rho_0 g}{18\mu} d_a^2 \quad (1.1)$$

where ρ_P is the effective particle density, ρ_F and ρ_T are the density of the fluid and the true density of the suspended particle, ρ_0 is the standard reference particle density at 1000 kg/m^3, ϕ is the porosity of the particle, g is the gravitational acceleration, μ is the dynamic viscosity of the medium, and χ is the dynamic shape factor to account for non-spherical particles. Therefore, particles with a higher true density than the liquid will settle to the bottom of the suspension while particles with a lower true density than the liquid will exhibit upward velocity and eventually

accumulate at the top, forming a cream layer. Smaller liquid-particle density difference, structured particles with high porosity, and smaller particles can all help reduce the particle settling velocities and stabilize the suspensions. In real applications, situations involving only individual particles are rarely seen and, for this reason, the effects of agglomeration need to be included in this discussion.

Particle agglomeration, which is also known as flocculation or aggregation, is a combined effect of both attractive and repulsive forces present in the suspension system. The forces between particles in colloidal systems are usually described by the classic Derjaguin-Landau-Verwey-Overbeck (DLVO) theory (Israelachvili, 2011), in which attractive van der Waals forces and repulsive double-layer forces are considered. Usually for pressurized suspensions, the repulsive electrostatic double-layer forces are usually weak and negligible due to the low dielectric constant and conductivity of the propellants. The van der Waals forces between macroscopic particles are caused by the collective inter-molecular forces from the interacting particles, and they drive the adhesion and cohesion of particles. For two perfectly spherical particles of radii R_1 and R_2, the macroscopic Van der Waals force, F_{VDW}, can be described by (Israelachvili, 2011):

$$F_{\mathrm{VDW}} = -\frac{A_{\mathrm{H}}}{6D^2}\left(\frac{R_1 R_2}{R_1 + R_2}\right) \quad (R_1, R_2 \gg D) \tag{1.2}$$

in which A_{H} is the Hamaker constant that depends on the materials of the two interacting particles. D is the minimum separation distance of the two particles at which the attractive and repulsive molecular forces are balanced, and its values are substance-dependent with a typical value of 0.4 nm. Accordingly, larger particles will show stronger attraction forces. In a suspension system, the larger particles also demonstrate higher collision frequencies because of their larger cross-section area and higher settling velocities. The collision frequency can be further enhanced by the

stronger attractive van der Waals forces between larger particles, leading to the growth of the large particles or agglomerates through the attraction of the other particles and consequently faster settling velocities.

1.4. Stabilization of Suspensions

Because of the inherent instability of solid suspensions, various approaches have been developed to improve the colloidal stability of pharmaceutical suspensions for better performance. According to **Eqn.(1.1)**, hollow-porous particles by increasing the particle porosity ϕ (Dellamary et al., 2000; Hirst et al., 2002) and nanosuspensions by reducing the size of suspended particles d_V (Patravale and Kulkarni, 2004; Rabinow, 2004) have been two of the most commonly used strategies to minimize the settling velocities of suspended particles in order to achieve stable suspensions. Particles with hollow-porous structures allow the propellant to permeate freely into the particles, minimizing the particle-liquid density difference and reducing their settling velocities. Nanosuspensions are colloidal dispersions of nanoparticles that either exhibit low settling velocities or may never completely settle because of the counteracting effect of Brownian motion (Lieberman et al., 1996). Propellant blends with densities close to the true densities of suspended particles have also been demonstrated to be able to stabilize suspensions (Smyth, 2003; Williams et al., 1998).

Surfaces of the suspended particles can also become charged through various mechanisms, such as ionization or dissociation of surface groups, or adsorption or binding of ions from solution; in such cases the net surface charges are balanced by a layer of counterions, forming a diffuse electric double-layer (Israelachvili, 2011). Particles with similarly charged surfaces repel each other electrostatically when approaching each other, causing the suspensions to stabilize.

However, the repulsive electrostatic forces originating from the electric double-layers are usually considered insignificant in preventing particles from aggregating in non-aqueous suspension systems where the liquid phases have low conductivities and dielectric constants, as is the case for pharmaceutical suspensions contained in pressurized metered dose inhalers (Johnson, 1996; Rogueda, 2005). Therefore, suspension-based pMDIs with non-aqueous propellants are mainly governed by the attractive van der Waals forces and are inherently unstable.

Due to the absence of electrostatic double layers, polymeric surfactants are also commonly used to introduce steric repulsion forces between particles to stabilize suspensions (Ashayer et al., 2004; Wang et al., 2013; Wu et al., 2011). The surfactants are usually amphiphilic non-ionic polymer molecules with long tails that can adsorb onto the surface of the drug particles and form a molecular layer of barrier that prevents the particles from approaching each other, thereby stabilizing the suspensions. Surfactants commonly used in pMDI suspensions include lecithin, oleic acid, and sorbitan trioleate because of their relatively good solubility in the propellant. Unfortunately, the mandated switch from chlorofluorocarbon propellants to "ozone-friendly" hydrofluoroalkane (HFA) propellants over the past 20 years has resulted in unexpected formulation challenges because of the incompatibility between the HFA propellants and traditional surfactants (Selvam et al., 2006). Such incompatibility is expected to become more of an issue as newer propellants with lower global warming potential are actively developed in the pharmaceutical industry (Myrdal et al., 2014).

This thesis starts with an introduction to the dispersed system, the applications of suspensions in the pharmaceutical field, the colloidal stability issues associated with solid suspensions, and the approaches that have been employed for the stabilization of these suspensions, followed by the introduction to the development of a new shadowgraphic imaging

method for the qualitative and quantitative analysis of colloidal stability of, but not limited to, pressurized pharmaceutical suspensions. With the developed shadowgraphic imaging technique, an important factor that has been overlooked during stability assessment, the effect of initial agitation, is then evaluated by comparing various agitation methods using different suspension formulations. With the assistance of the shadowgraphic imaging technique, a systematic study of the effects of particle surface roughness on the colloidal stability of pressurized pharmaceutical suspensions is conducted to evaluate the applicability of this surfactant-free and propellant-independent approach of suspension stabilization. Impact of the work conducted in this thesis is iterated in the end with a few directions for further study.

CHAPTER 2 Characterization of the Suspension Stability of Pharmaceuticals Using a Shadowgraphic Imaging Method

A new shadowgraphic imaging method and an associated instrument for analyzing the colloidal stability of pharmaceutical suspensions are introduced in this chapter. The new suspension tester consists mainly of a high-resolution camera that takes sequential shadowgraphic images of emulsions or suspensions and a 2D collimated LED for simultaneous whole-sample illumination in a bright field, and the acquired images are analyzed for changes in transmission intensity profiles over time. Suspension stability testing results in the form of normalized transmission profile and instability index plot provide both qualitative and quantitative description of the entire destabilization processes. Simultaneous illumination of the complete suspension, a high image acquisition rate, and convenient cross-sample comparison are features that make this new suspension tester a suitable and more reliable instrument for investigating the stability of pressurized pharmaceutical suspensions, filling the blank left by the missing technique dedicated to the stability analysis of pressurized pharmaceutical suspensions.

2.1. Introduction

In seeking to overcome the challenges of developing stable pharmaceutical suspensions for reliable and consistent drug delivery, researchers have employed various indirect stability characterization techniques as a means of improving formulation development (Ooi et al., 2015). Atomic force microscopy is one such technique widely used to measure the interaction forces between drug particles and the various components of a pMDI system, e.g. other drug particles, the canister, and surfactants. This technique has identified the presence of strong interaction forces between different pMDI components as a factor responsible for physical instability and even poor

re-dispersibility due to particle flocculation (Ashayer et al., 2004; D'Sa et al., 2014; Rogueda et al., 2011; Wu and da Rocha, 2007).

Although being typically weak in non-aqueous systems, the zeta potential of various propellant suspension systems has also been extensively investigated (Jones et al., 2006; Kayes, 1977; Sidhu et al., 1993); such measurements, however, do not correlate well with final suspension stability (Johnson, 1996; Rogueda, 2005). Particle size measurement by cascade impactors has been used as yet another indirect means of characterizing potential particle agglomerations (Dellamary et al., 2000; Jones et al., 2006). For suspensions prone to rapid phase separation by creaming or sedimentation, the concentration of drug re-filling the pMDI metering chamber after the release of a preceding dose may be substantially different from the overall drug concentration in the propellant. Thus, dose uniformity becomes a problem (Weers and Tarara, 2014). Dose uniformity analysis evaluating the consistencies between the actuated doses has in fact confirmed the presence of creaming or sedimentation in suspensions (Dellamary et al., 2000; Vehring et al., 2012).

More promising for the stability analysis of suspensions are characterization techniques allowing direct *in situ* assessment. Among these, optical methods are favored because they are fast, non-destructive, and easily adaptable to pressurized systems. Jones et al. (Jones et al., 2005; Jones et al., 2006) successfully measured the particle size distribution of suspended drug particles in pressurized propellant using a modified laser diffraction sizing system. However, this technique failed to reveal any information about the migration of suspended particles. Brindley (Brindley, 1999) proposed an optical suspension characterization set-up called OSCAR, which utilized pairs of infrared emitter/detector probes to measure the light transmission intensity at different positions of tested samples. Although the method was able to identify rapid suspension changes, the

transmission measurement was limited to only two positions, thus making cross-sample comparisons difficult.

Among commercial instruments designed for direct characterizing techniques, Turbiscan (Mengual et al., 1999a; Mengual et al., 1999b) and LUMiSizer (Lerche and Sobisch, 2007, 2014) have been widely used in the stability analysis of emulsions and suspensions. The TurbiScan instrument consists mainly of a platform equipped with a near-infrared laser as light source and two synchronous detectors that scan up and down along a flat-bottomed glass sample vial to measure transmitted and backscattered light intensity during measurement. A major shortcoming of the TurbiScan lies in the fact that its maximum scan rate of 1 min/scan is too slow for analysis of relatively unstable samples (Dellamary et al., 2000). The LUMiSizer is a multi-sample analytical centrifuge equipped with a built-in light source and a linear CCD sensor that allows measurement of transmitted light intensity over the entire sample length simultaneously. Unfortunately, it only permits the use of square glass cuvettes without pressurization, and the centrifugal acceleration makes it suitable only for accelerated studies on relatively stable samples. In suspension samples where both the method and extent of initial agitation used to re-disperse the suspended particles can greatly affect the resultant stability of tested suspensions (Mayer et al., 2002; Sesis et al., 2013), neither the Turbiscan nor the LUMiSizer is capable of controlling the initial agitation of the suspension samples.

In the absence of appropriate techniques for characterizing the stability of pressurized suspensions, qualitative visual observation is still frequently used in the literature to compare the stability of different samples (Engstrom et al., 2009; Li and Seville, 2010; Wu and da Rocha, 2007, 2011). In this chapter, a new suspension tester that meets the requirements for stability analysis of pressurized suspensions, i.e. a fast acquisition rate, quantitative analysis, and compatibility with

pressurized sample vessels, was developed. Selected applications in the stability analysis of pharmaceutical suspensions are presented to demonstrate its capabilities. Not limited to pressurized pharmaceutical suspensions, the shadowgraphic imaging method presented in this chapter can be easily applied to other multiphase systems where stability is of importance, e.g., poorly water-soluble micro and nanosuspensions, cosmetics, emulsions, oil and sand systems, and food and beverages.

2.2. Materials and Methods

2.2.1. Materials

2.2.1.1. Oil-in-water emulsions

Since emulsions are well-studied systems that behave similarly to suspension systems (Schramm, 2014), a series of oil-in-water emulsions containing different mixtures of oil and surfactants were tested to determine the required hydrophilic-lipophilic balance (HLB) of the oil as a means of verifying the new instrument. Pure sunflower oil (Loblaws Inc., Toronto, Ontario, Canada) and surfactant mixtures were used to prepare oil-in-water emulsions. Tween^{TM} 80 and Span^{TM} 80 (Sigma-Aldrich Canada Co., Oakville, ON, Canada) with individual HLBs of 15 and 4.3 were used to prepare the surfactant mixtures. HLBs of surfactant mixtures (Pasquali et al., 2008) are calculated according to:

$$\phi_{\mathrm{Mix}} = x\phi_{\mathrm{T}} + (1-x)\phi_{\mathrm{S}} \tag{2.1}$$

where ϕ_{T} and ϕ_{S} are the HLB values of Tween 80 (15.0) and Span 80 (4.3), with their corresponding mass fraction being x and $(1-x)$ respectively. ϕ_{Mix} is the HLB value of the resultant surfactant mixture. The mixing ratio of the two non-ionic surfactants was adjusted to produce surfactant mixtures with different HLB values from 6.0 to 8.0 at a step of 0.5. As listed in

Table 2.1, five groups of emulsions were prepared, and the emulsion in each group was prepared and measured for stability independently three times. Mass concentrations of oil and surfactant in all emulsions were kept constant at 5% and 2% respectively. Emulsification of oil in water was achieved using a phase inversion point method (Liu et al., 2006). The mixture of oil, Span, and Tween was first mixed by gentle magnetic stirring at 350 rpm and room temperature. While the mixture was stirred, demineralized water was added at a constant rate of 1 mL/min, using a syringe pump (HD Ultra, Harvard Apparatus, Holliston, MA, USA) to force a phase inversion from water-in-oil to oil-in-water emulsion. The emulsions were then transferred to glass vials for stability analysis.

Table 2.1. Composition of prepared emulsions with surfactant mixtures of varying HLB values.

Group	Oil (g)	Span (g)	Tween (g)	Water (g)	Total (g)	HLB	Replicate
1	2.5	0.84	0.16	46.5	50.0	6.0	×3
2	2.5	0.79	0.21	46.5	50.0	6.5	×3
3	2.5	0.75	0.25	46.5	50.0	7.0	×3
4	2.5	0.70	0.30	46.5	50.0	7.5	×3
5	2.5	0.65	0.35	46.5	50.0	8.0	×3

2.2.1.2. Phospholipid particles

Phospholipid microparticles were prepared by spray drying an ethanolic solution of 1,2-distearoyl-sn-glycero-3-phosphocholine (DSPC; Lipoid GMBH, Germany) using a modified Büchi B-191 lab-scale spray drier (Büchi Labortechnik AG, Flawil, Switzerland). An ethanolic solution of DSPC as the liquid feedstock was supplied to a twin-fluid atomizer by a peristaltic pump (Masterflex® L/S®, Cole-Parmer, Montreal, Quebec, Canada) and then dried in a glass

chamber. To guard against the flammability of ethanol, nitrogen was supplied as the drying gas. More detailed parameters used for the spray drying are given in **Table 2.2**. The spray dried DSPC particles were collected with a glass cyclone and their mass median aerodynamic diameter (*MMAD*) and geometric standard deviation (*GSD*) were determined to be 3.0 – 3.5 μm and 1.8 using a time-of-flight aerodynamic particle sizer (3321, TSI, Shoreview, MN, USA). The collected powders were further dried in a vacuum desiccator for three days to remove any residual solvent and then used to prepare the pressurized DSPC suspension. A DSPC standard with a more ordered solid phase (Marsh, 2013) was prepared using a solvent evaporation method (Weyna et al., 2009) that allows slow evaporation of the ethanol and precipitation of the dissolved lipid molecules in a vacuum and at room temperature.

Table 2.2. Parameters used for spray drying of DSPC particles.

Spray-drying parameter	Value
Feed solution concentration (mg/mL)	25
Atomizing gas flow rate (L/min)	5.4 ± 0.7
Drying gas flow rate (L/min)	453 ± 14
Feedstock flow rate (mL/min)	5.0 ± 0.1
Inlet temperature (°C)	50.0 ± 1.0
Outlet temperature (°C)	35.7 ± 0.2

2.2.1.3. Pressurized suspensions

A pressurized DSPC suspension was prepared by weighing 50 mg ± 2 mg of the spray-dried DSPC powder into a glass vial, crimping an aluminum metering valve (DF30, Valois Pharma, Congers, NY, USA) onto the glass vial, and then using a benchtop pMDI production station (2005/21, Pamasol Willi Mäder AG, Pfäffikon, Switzerland) to pressure-fill 25 g of HFA-134a

propellant (1,1,1,2-tetrafluoroethane, GDR134a, Gregg Distributors Ltd., Edmonton, Alberta, Canada) through the valve and into the vial. The suspension was sonicated for 1 min to break up any aggregated particles and then transferred for stability monitoring in a 5-day aging study under ambient conditions ($T = 23 \pm 2$ °C).

2.2.2. Suspension tester

2.2.2.1. Instrument design

The instrument designed in this study for stability analysis is a shadowgraphic imaging system, with its CAD model shown in **Figure 2.1**. The main components include a 12-bit high-resolution (2560×2048 pixel) monochrome CCD camera (SP-5000M-PMCL, JAI Inc., San Jose, CA, USA) equipped with a 16mm fixed-focal length lens (86-571, Edmund Optics Inc., NJ, USA), a 2D collimated LED backlight (CX0404-0530C5, Advanced Illumination Inc., Rochester, VT, USA) connected to a high-output strobe controller (Pulsar 320, Advanced Illumination Inc., Rochester, VT, USA), and a two-channel function generator (AFG1022, Tektronix Inc., Beaverton, OR, USA) that synchronizes the camera and the LED backlight. Two 'Power over Camera Link' data cables are used to connect the camera to an installed frame grabber (PCIe-1433, National Instruments Corp., Austin, TX, USA), enabling direct power supply from the data cable and fast image acquisition rate up to 120 fps. Round, flat-bottomed borosilicate glass vials (Adams & Chittenden Scientific Glass, Berkeley, CA, USA) measuring 75.5 mm in height and 27.5 mm in outer diameter, and featuring a > 9 bar pressure rating, a crimpable glass top, and good transmissivity are used as the standard sample vessels for stability measurement in this study. These vessels allow us to study the behavior of suspended particles in a pressurized liquid contained in a cylindrical volume that is similar to a commercial pMDI; however, the potential particle-wall and particle-valve interactions associated with pMDIs are beyond the scope of this

study. To avoid interference from ambient and reflected stray light, all optical components were enclosed in a light-proof sample chamber, the interior of which is covered with a light-absorbing material. In summary, this instrument acquires sequential shadowgraphic images of a sample at a set of predetermined settings as listed in **Table 2.3**. These images are then processed to extract transmission information for the suspension stability analysis.

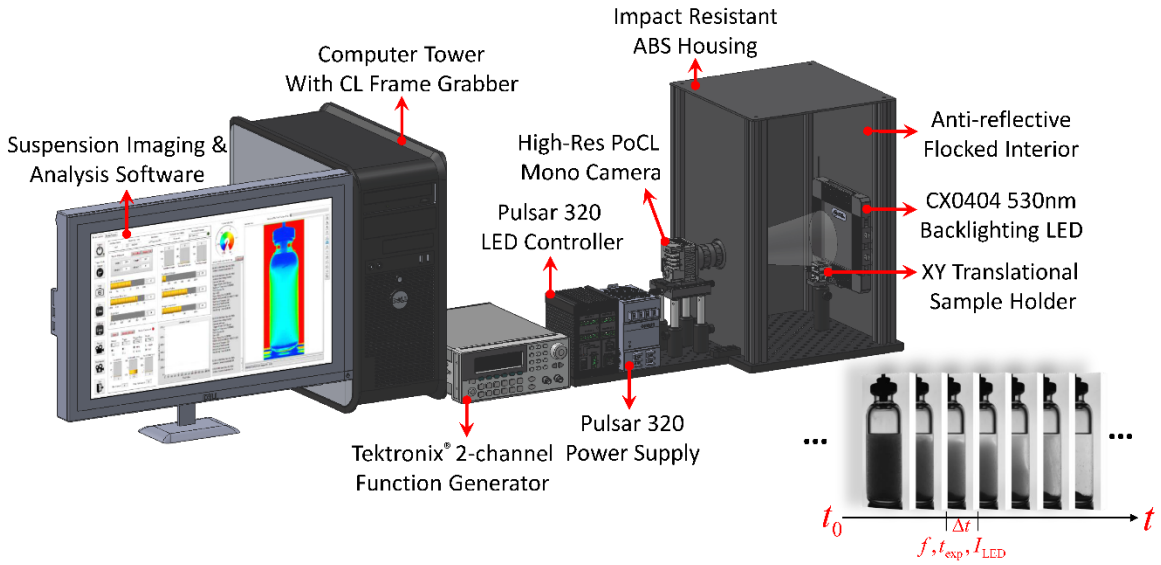

Figure 2.1. Schematic of the new suspension tester for stability analysis of pressurized pharmaceutical suspensions. This instrument takes sequential shadowgraphic images of suspension samples at pre-determined settings such as frame rate, duration, exposure time, etc.

Table 2.3. Specifications and actual experimental settings of the suspension tester

Experiment Settings	Specification	Emulsion	DSPC Suspension
Camera frame rate (Hz)	0.001 – 100	0.02	1.0
Camera exposure time (ms)	0.001 – 1000	0.50	0.12
Camera digital gain	100 – 1000	100	100
Backlight driving current (A)	0.1 – 10	1.0	1.0
Backlight pulse width (ms)	0.01 – 100	1.0	1.0
Total acquisition time (hh:mm)	-	03:00	00:15

2.2.2.2. Data processing

The acquired sequential images were processed as follows. With each of the shadowgraphic images, an absolute transmission profile, $T^{a}_{t,h}$, as a function of time (t) and positioning in the sample (h), was obtained as shown in **Figure 2.2**. The raw transmission intensity at a specific height h was calculated by summing up the intensity of that specific row of pixels, and the summed intensity for each row of pixels was then plotted along the height of the suspension to obtain the transmission profiles. Therefore, sequential shadowgraphic images acquired at different time points of the measurement also produce sequential transmission profiles.

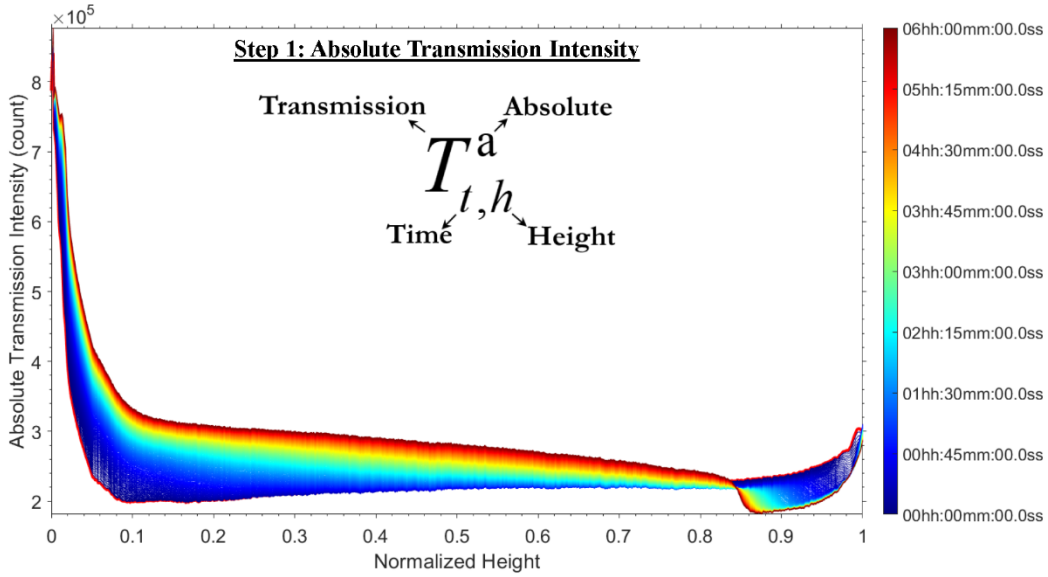

Figure 2.2. First step of shadowgraphic image processing: extraction of absolute transmission profiles, $T^{a}_{t,h}$, from the sequential shadowgraphic images.

To quantify the transmission change over time, a relative transmission, $\Delta T_{t,h}$, was calculated by subtracting the initial transmission profile, $T^{a}_{t_0,h}$, from all the subsequent profiles, $T^{a}_{t,h}$, as

follows, making the initial relative transmission profile a straight line at corresponding to a transmission intensity of 0, as demonstrated in the following **Figure 2.3**.

$$\Delta T_{t,h} = T^{\mathrm{a}}_{t,h} - T^{\mathrm{a}}_{t_0,h} \tag{2.2}$$

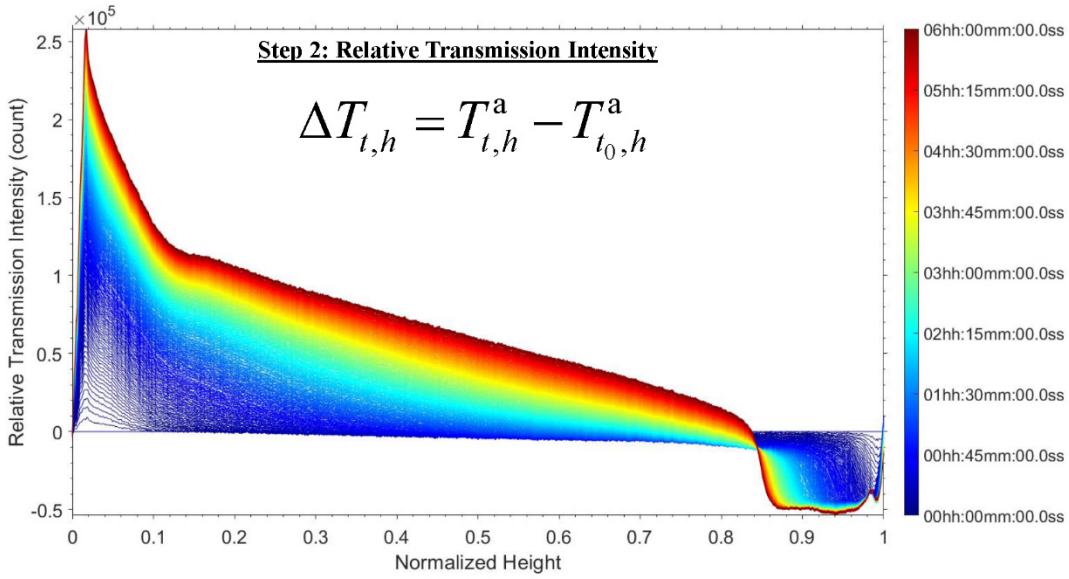

Figure 2.3. Second step of the data processing: calculating the change of transmission intensity relative to the initial transmission profile. The initial relative transmission profile is a straight line at the transmission intensity of 0.

Therefore, the transmission change is a joint effect of particle size change caused by flocculation and concentration change due to collective particle migration. Transmission intensity distribution along each row of pixels as a means of identifying flocculation is not considered in this study. The relative transmission, $\Delta T_{t,h}$, was then normalized by its maximum possible value, $\Delta T^{\mathrm{Max}}_{t,h}$, which is the difference between the transmission for clear propellant contained in a standard glass vial, $T^{\mathrm{a}}_{\mathrm{Clear}}$, and the initial transmission of the sample being tested, $T^{\mathrm{a}}_{t_0,h}$, as

demonstrated in **Figure 2.4**. The normalized relative transmission profiles, $\Delta T_{t,h}^{\mathrm{N}}$, describe how a tested sample destabilizes during the stability analysis and are defined as:

$$\Delta T_{t,h}^{\mathrm{N}} = \frac{\Delta T_{t,h}}{\Delta T_{t,h}^{\mathrm{Max}}} = \frac{\Delta T_{t,h}}{T_{\mathrm{Clear}}^{\mathrm{a}} - T_{t_0,h}^{\mathrm{a}}} \tag{2.3}$$

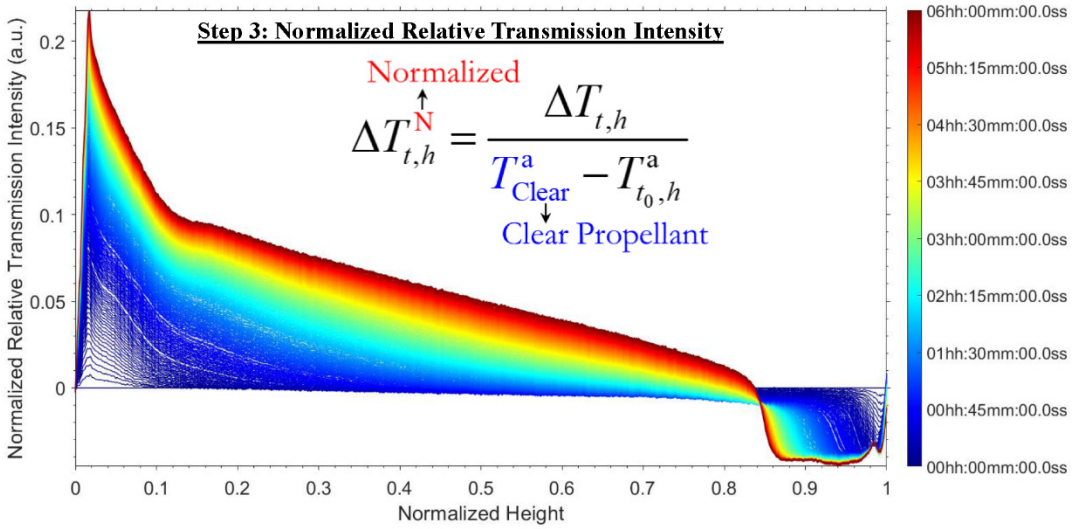

Figure 2.4. Normalization of the relative transmission profiles by its maximum possible value.

An intensity map for the transmission intensity through clear propellant, $T_{\mathrm{Clear}}^{\mathrm{a}}$, was generated by measuring a set of shadowgraphic images using different combinations of LED power and camera exposure time. Good linearity is observed for the transmission intensity on the exposure time as shown in **Figure 2.5**. Slopes and intercepts of the curves are also linearly dependent on the LED power settings. Therefore, a universal equation was produced to predict the transmission intensity at arbitrary LED and camera settings by linearly fitting the slopes and intercepts, especially when intensities higher than the full well capacity of the pixels (4096) are needed for highly concentrated suspensions. Details of the fitting and the derived equation can be

found in Appendix II. The pixel intensity equation needs to be calibrated everytime when the configuration of the imaging system is changed.

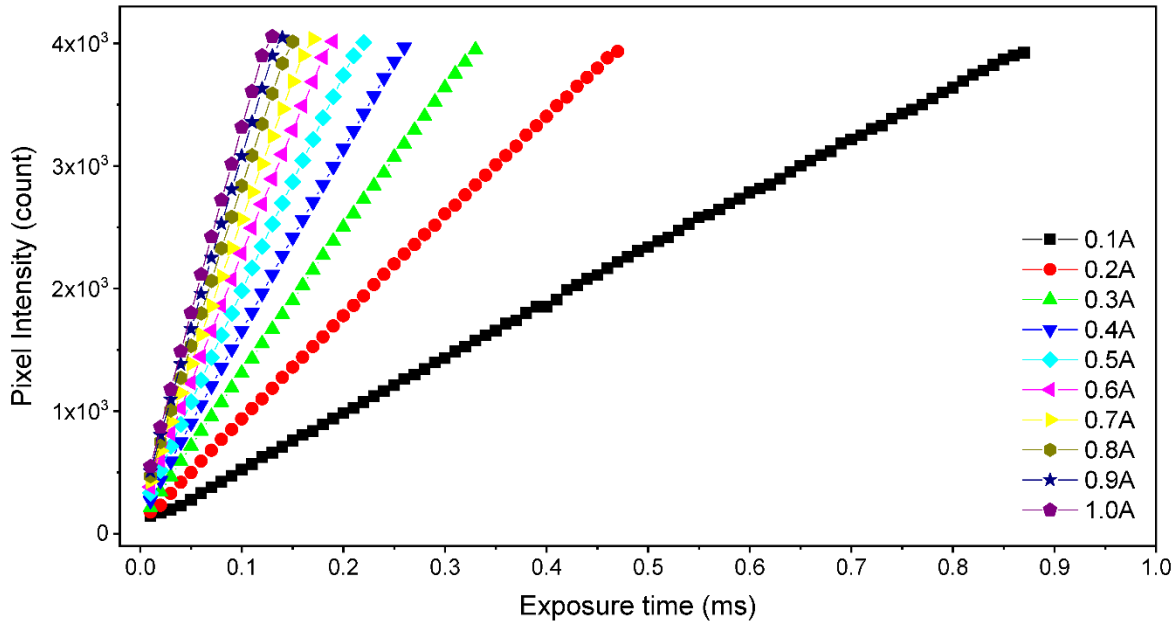

Figure 2.5. Transmission intensity map for different combinations of light source power in ampere and camera exposure time in milliseconds. The plot demonstrates a good linearity of the light intensity on the exposure time.

By integrating the normalized relative transmission profile, $\Delta T_{t,h}^{\mathrm{N}}$, along the sample height, h, an instability index function, $\sigma(t)$, was obtained such that:

$$\sigma(t) = \int_{h=0}^{h=1} \left| \Delta T_{t,h}^{\mathrm{N}} \right| \tag{2.4}$$

which accounts for the overall transmission change over time (Detloff et al., 2013; Lesaint et al., 2009). Based on this derivation, the instability index is a dimensionless number ranging from 0 to 1 that starts from 0 for all stability studies. A suspension sample that creams or settles completely to its clear propellant and forms an infinitely thin opaque layer would have its final instability

index approaching 1.0. The slope of the instability index plot as a function of time, $d\sigma(t)/dt$, describes the rate of destabilization. All equations here are expressed in their continuous forms for explanatory purposes while the sample height and time variables have been discretized pixel- and frame-wise respectively in the actual calculations. The instability index can be used to quantitatively compare and rank-order suspensions with different stabilities.

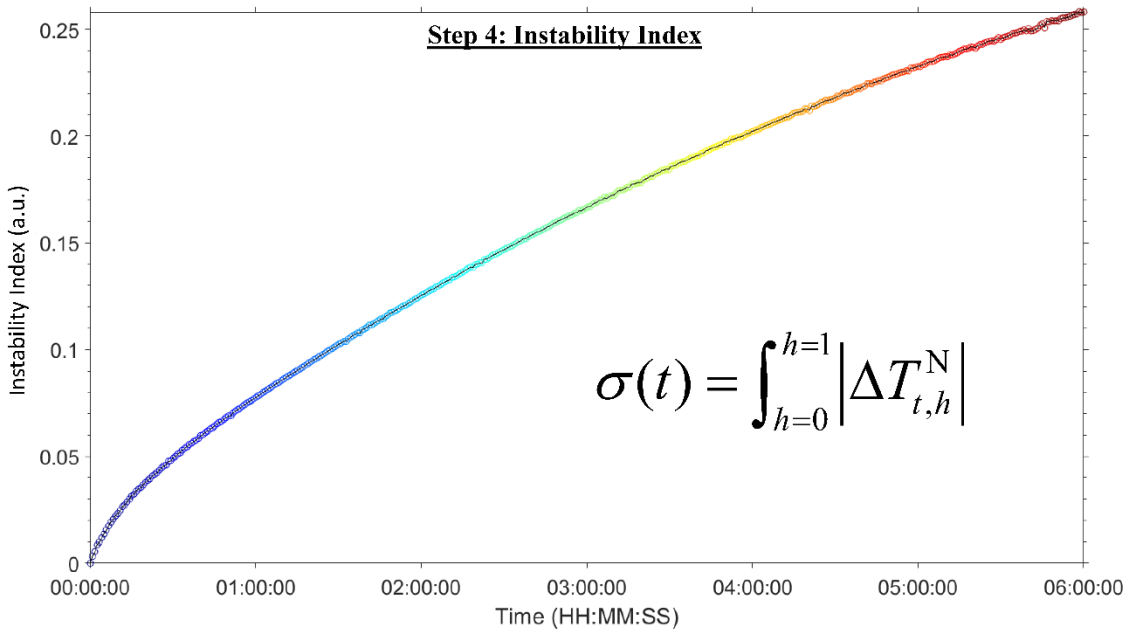

Figure 2.6. Derivation of the instability index, $\sigma(t)$, by integrating the normalized relative transmission profiles.

2.2.2.3. Uncertainty

As an imaging technique, the optical components used in the system, including the CCD sensor of the camera, the polarizing filter, lens, and the back-illuminating LED panel, can potentially introduce systematic errors to the results of suspension stability measurements. To determine the stability of the overall detectable light intensities, a typical combination of the camera exposure time and LED output power (0.1 ms - 1.0 A) was used to acquire shadowgraphic

images of the LED panel without samples for 15 minutes, and the resultant relative intensity profiles based on **Eqn.(2.5)** are presented in **Figure 2.7**. Over the 15 minutes observation, the detectable light intensity fluctuates within ± 0.3%, demonstrating both stable light output from the LED panel and consistent performance of the imaging components including the polarizing filter, lens, and camera. By using a black initial image, the instability index curve for the acquired sequential images was also derived. Since no sample was loaded during the image acquisition, the instability indices shown in **Figure 2.8** can be equally treated as the bias error of the shadowgraphic imaging system. Under the current camera and LED setting, the bias error for the instability index is on the magnitude of 0.001, which is negligible considering that the instability index approaches 1.0 for relatively unstable samples. Therefore, the systematic errors caused by the fluctuation of light intensity can be neglected. This also proves that the instrument calibration presented in Appendix II provides an accurate prediction of the maximum transmission intensity under the given experiment settings.

$$\Delta T_{t,h}^{\mathrm{e}} = \frac{\Delta T_{t,h}}{T_{t_0,h}^{\mathrm{a}}} \times 100\% \tag{2.5}$$

A major source of random error can be traced back to the initial agitation of the samples to be tested. When manual shaking is used to re-disperse the suspended particles, of which the magnitude cannot be quantitatively controlled, the level of dispersion may vary between different operators and even different shaking motions. Different agitation methods such as wrist action shaking, vortex mixing, and ultrasonic agitation, can also significantly change the destabilization process of the suspensions, especially when particle agglomeration is involved, leading random errors to the results of suspension stability analysis. The effect of agitation method on suspension stability will be discussed in the next chapter.

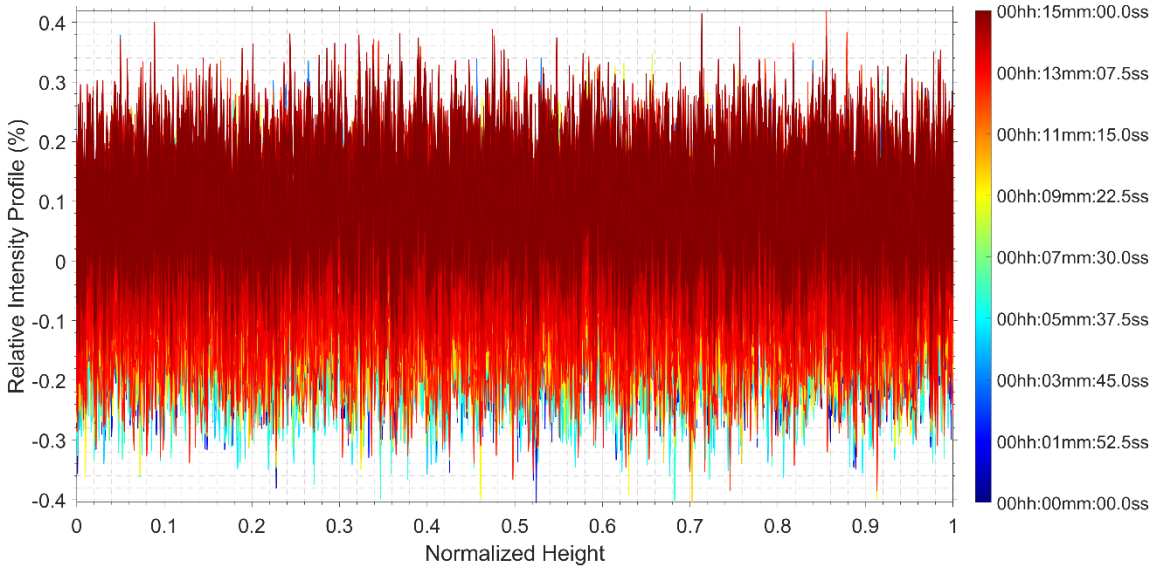

Figure 2.7. A typical combination of camera exposure time (0.1 ms) and LED output power (1.0 A) was used to acquire the shadowgraphic images for 15 minutes. Relative intensity profiles show stable detectable light intensity by the camera with < 3% overall intensity fluctuation.

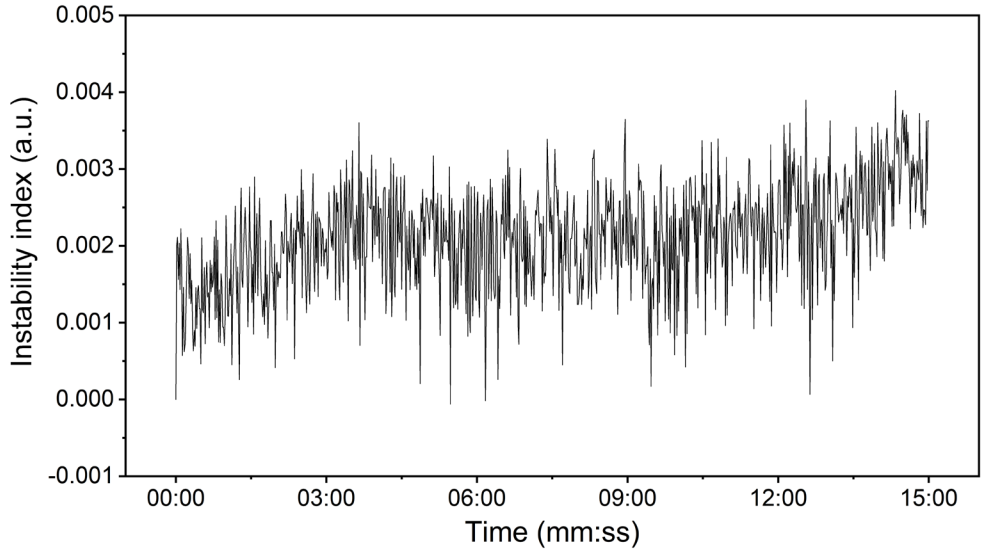

Figure 2.8. Bias error of the derived instability index caused by the fluctuation of the light intensity is demonstrated to be negligible (< 0.004) when the LED and camera were operated at 1.0 A and 0.1 ms respectively.

2.2.3. Methods

2.2.3.1. Stability analysis

To verify instrument methodology, the stability of each of the five groups of oil-in-water emulsions listed in **Table 2.2** was measured. Each sample was measured for three hours immediately after preparation. Normalized relative transmission profiles for the emulsions were derived to compare their destabilization processes, and instability indices at the end of the 3-hour stability study were used to rank the different groups of emulsions.

To evaluate the suitability of the new suspension tester for routine pharmaceutical suspension stability testing, the pressurized suspension of spray dried DSPC particles in HFA-134a propellant was monitored for its stability in a 5-day aging study after propellant filling. The suspension was stored under room conditions between each measurement, and its stability was measured for 15 minutes every 24 hours. Immediately before each measurement, the suspension was agitated for 10 s in an external small-scale ultrasonic bath (M1800H, Fisher Scientific Comp., Ottawa, ON, Canada).

2.2.3.2. Morphological and spectroscopic analysis

Suspended DSPC particles in the fresh (t = 0 day) and aged (t = 5 days) suspension were both analyzed using a scanning electron microscope (EVO M10, Zeiss, Oberkochen, Germany) and a custom-built Raman spectrograph (Wang et al., 2017a) to detect any morphological or structural changes. The particles contained in the pressurized suspension were extracted by actuating several doses into a low-flow-rate single-nozzle impactor (Wang et al., 2017b) that uses standard SEM stubs as its impaction plates in a drying chamber. A single-stage configuration of the impactor consisting of the first stage, the middle stage with a nozzle diameter of 1.00 mm, and the final stage was used for the aerosolized particle collection. Operating the impactor at a low

volume flow rate of 0.5 L/min gives a theoretical cut-off diameter of the collection stage at 1.84 μm, which is smaller than the *MMAD* of the produced lipid particles and enables collection of them with good efficiency. The evaporation of propellant from the droplet results in dry particles impacted on the SEM stubs. Particles collected for spectroscopic analysis were transferred directly from the naked stub to a 0.2 μL conical Raman sample holder while particle collected for morphological analysis were first coated with gold-sputtering (Desk II Sputter Coater, Denton Vacuum, NJ, USA) prior to SEM analysis. A detailed configuration of the impactor used for the particle extraction from the pMDI can be also found in Appendix III.

For spectroscopic analysis, the Raman system utilized a 671 nm diode-pumped laser (Ventus 671, Laser Quantum, UK) with a maximum power of 500 mW, and the samples were kept under a nitrogen atmosphere (< 3% RH) at room temperature (21 ± 1 °C) during spectrum acquisition. A more detailed description of the Raman measurement methodology has been discussed elsewhere (Wang et al., 2017a; Wang et al., 2014).

2.3. Results and Discussion

2.3.1. Determination of HLB of sunflower oil

As an instrument verification example, a series of oil-in-water emulsions prepared with surfactants varying in their HLB values were tested and their stabilities compared. Normalized relative transmission profiles for the five groups of emulsions with HLB values ranging from 6.0 to 8.0 are shown in **Figure 2.9**.

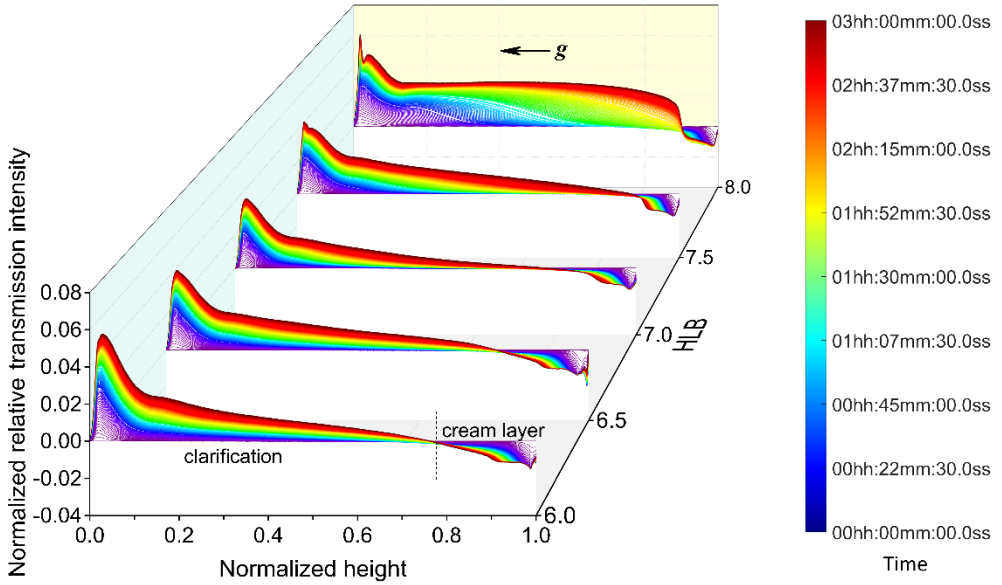

Figure 2.9. Normalized relative transmission profiles show different destabilization processes of emulsions prepared with surfactants of varying HLB values. Clarification and creaming are observed in all three cases. Direction of gravity is indicated by vector ***g***.

The transmission profiles represent how the emulsions developed during a three-hour observation. The profiles start at the bottom of the vial, at a normalized height of 0, and end at the top of the suspension, at a normalized height of 1. In all cases, cream layers formed at the top of the emulsions, as indicated by the reduced transmission intensity at the top of the vials. Clarification of the emulsions was observed as the transmission intensity increased in the bottom

regions of the emulsions An isosbestic point at which the transmission intensity does not change at all could also be detected, thereby giving the whole-sample illumination and acquisition method an advantage over single-point measurement methods like OSCAR (Brindley, 1999).

On the whole, the emulsions with HLB values of 6.0 to 7.5 destabilized similarly with only slight differences in the degree of clarification and creaming as indicated by the differences in the transmission intensity. However, they destabilized quite differently from the emulsion with a higher HLB value of 8.0, which clarified much more completely than the other cases. The transition from the clarified part to the opaque cream layer is more abrupt and is separated by a clearly defined boundary line. A clear separation line can be also observed from the inset shadowgraphic image of the corresponding emulsion. In order to rank-order the stability of the emulsions with HLB values of 6.0 to 7.5, the more quantitative instability index is needed.

The instability indices and corresponding shadowgraphic images at the 3-hour time point for all the measured emulsions are presented in **Figure 2.10**. The inset images show only small visual differences, especially between the four relatively stable samples at HLB values of 6.0, 6.5, 7.0, and 7.5. According to the corresponding indices, emulsion stabilities are not linearly related to the HLB values of the surfactants ranging from 6.0 to 7.5. However, the instability index agrees with the transmission profile that the surfactant with a high HLB value of 8.0 led to the most unstable emulsions, and the most stable emulsion corresponds to an intermediate case with a surfactant HLB value around 7.0. We can conclude that the required HLB of sunflower oil is between 6.5 and 7.5 since matching of the surfactant HLB to the required HLB of oil can lead to the most stable emulsion as a result of the lowest interfacial tension and smallest initial oil droplet size (Liu et al., 2006). This measured required HLB value also agrees very well with the reported sunflower oil property of 7.0 – 7.5 (Rahate and Nagarkar, 2007). In being able to measure the required HLB

value of oil, this new suspension tester together with the developed instability index shows itself to be more widely applicable for stability characterizations with good repeatability, high precision, and a fast acquisition rate. Moreover, the whole-sample illumination and image acquisition with high spatial resolution provides much more detail about the destabilization processes without any delay.

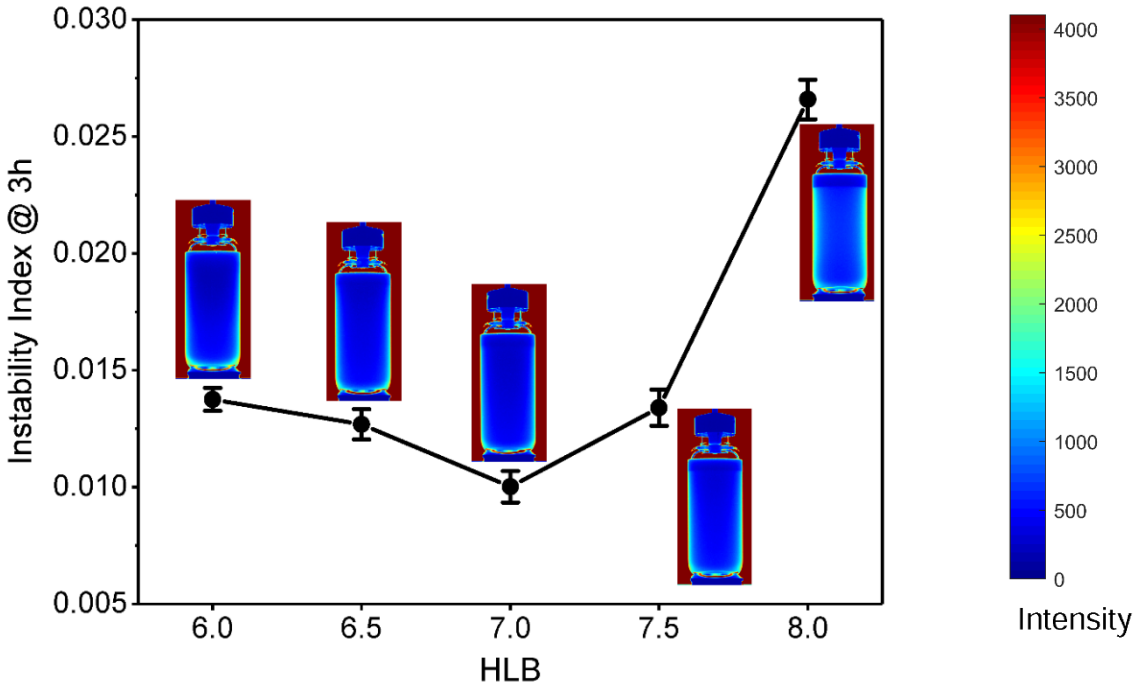

Figure 2.10. Instability indices σ (t = 3 h) for emulsions prepared with surfactants of varying HLB values. The most stable emulsion was achieved when the surfactant HLB matched the required HLB of oil between 6.5 and 7.5. Inset shadowgraphic images represent end state of the emulsions after 3 hours of settling. Intensity of each pixel is represented by different colors according to the color bar.

2.3.2. Stability change of spray-dried DSPC suspension during storage

The stability of the pressurized DSPC suspension was monitored for five days after propellant filling. Transmission profiles of the suspension at different time points are shown in **Figure 2.11**. The fresh suspension was stable during the 15 minutes of observation with only minor

clarification at the bottom of the vial and a weak indication of creaming. The level of clarification increased rapidly as the aging study progressed. The bottom half of the suspension clarified to up to 80% of its maximum possible transmission after 4 days of aging. Cream layers formed at the top of the aged suspension were indicated by the reduced transmission intensity. The thickness of the cream layer also increased gradually, as the boundary line indicated by the abrupt transmission transition moved towards the bottom.

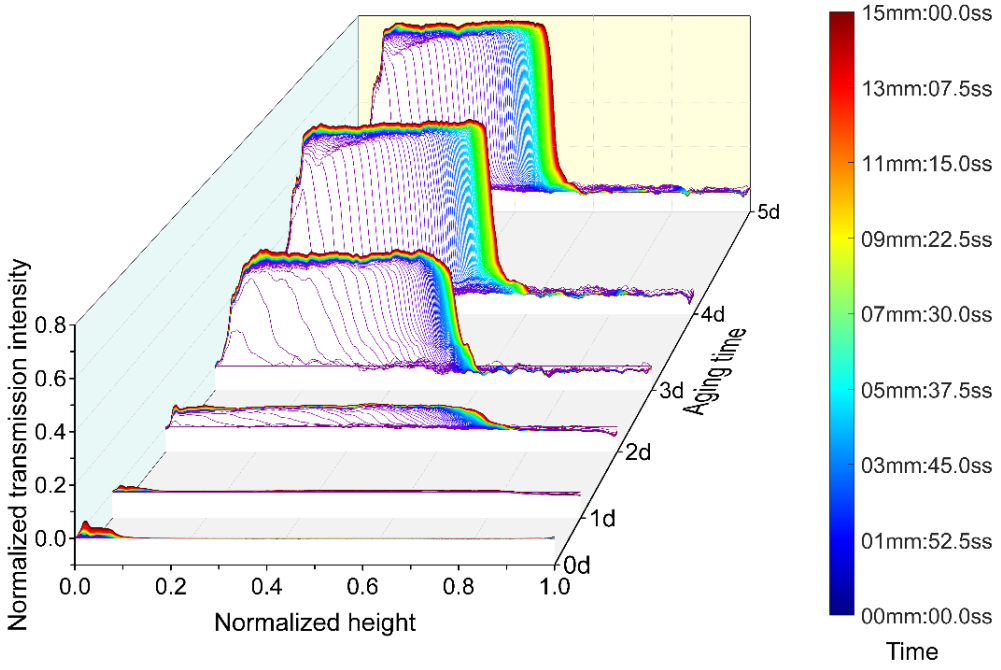

Figure 2.11. Normalized relative transmission profiles of the pressurized DSPC suspension changed significantly within the first 5 days after propellant filling. Level of clarification and thickness of the cream layer increased gradually.

Shown in **Figure 2.12** are the corresponding instability index plots for these measurements, which also show the suspension experiencing significant changes during the aging period. Initially, the fresh DSPC suspension was relatively stable within the first 24 hours. However, from day 1 to day 4, the stability of the suspension decreased quickly. Due to the sensitivity of the instability

index to minor suspension changes, the slopes of the instability index plots indicate that a rapid destabilization process started at the beginning of the measurement and was mostly completed within the first 3 minutes for the aged suspensions. In combination with the transmission profiles shown in **Figure 2.11**, different levels of clarification and creaming can also be observed in the inset shadowgraphic images.

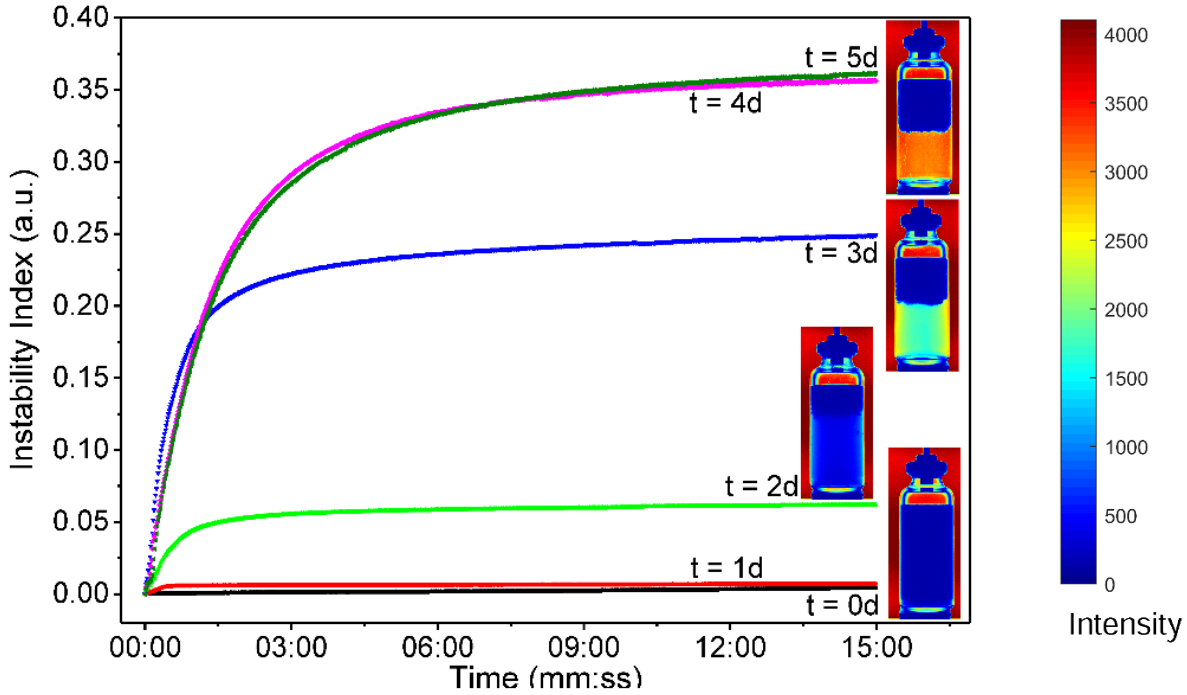

Figure 2.12. The different instability index plots show significantly different destabilization processes in the DSPC suspension. Insets are the shadowgraphic images recorded at days 0, 2, 3 and 5 by the end of each stability measurement. Pixel intensities varied from 0 to 4096 as represented by the different colors from blue to red.

By plotting the final instability indices at the end of the 15 min stability measurement, the trend of the suspension stability change is presented more clearly in **Figure 2.13**. The whole aging process can be roughly divided into three ranges: 0 – 1 d, 1 – 4 d, and > 4 d. The fresh suspension of spray dried phospholipid particles was stable for at least 15 minutes at days 0 and 1. The

suspension stability decreased significantly in the following time period from day 1 to day 4. After 4 days, the decrease in stability slowed down. Therefore, the semi-quantitative transmission profiles together with the quantitative instability indices make it very straightforward to reproduce the whole destabilization process, as well as comparing the stabilities of multiple samples.

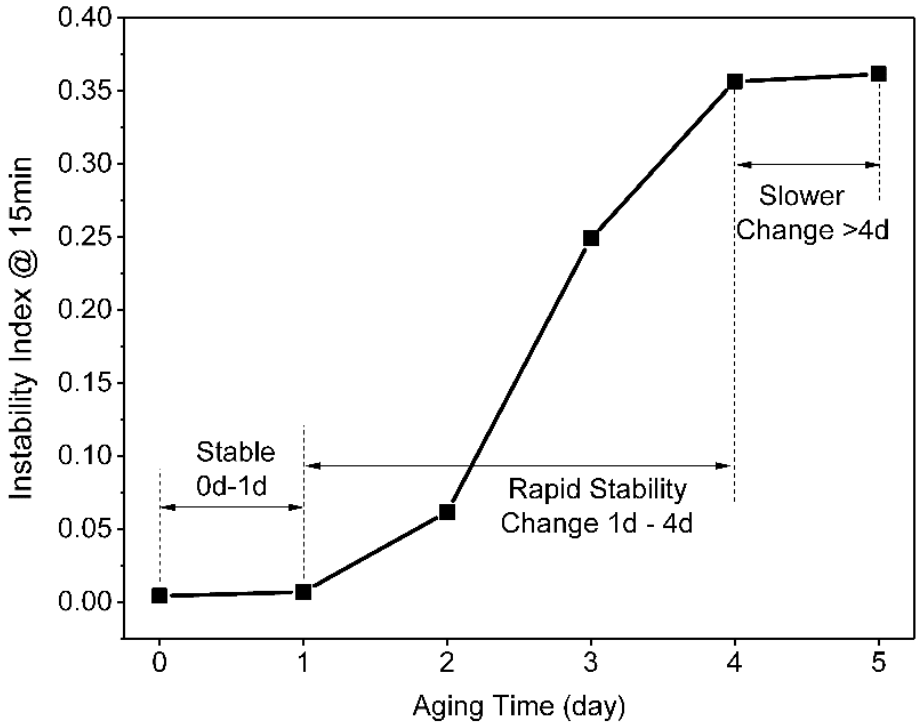

Figure 2.13. This figure shows the final instability indices σ (t = 15 min) for measurements at different time points of the aging study. The trend of the plot indicates a significant drop in suspension stability during the study.

Morphological and spectroscopic analysis was conducted on the particles extracted from both the fresh and aged suspension to find the reason for the change in suspension stability. Electro-micrographs of the fresh and aged DSPC particles are displayed in **Figure 2.14**. DSPC particles went through significant morphological changes during the aging study. Well-dispersed wrinkled particles with irregular surface morphologies were observed for the fresh lipid particles.

The wrinkled particle morphology is formed mainly through the accumulation of the DSPC on the surfaces of solution droplets during the drying processes (Vehring, 2008). Geometric sizes of the freshly spray dried lipid particles from the SEM images are in accordance with the particle size characteristics measured by the aerodynamic particle sizer. By contrast, thin sheets of lipid instead of well-defined particles were found for the aged suspension. The dimensions of the lipid sheets were as large as 10 μm along their long axes – much larger than the original particles.

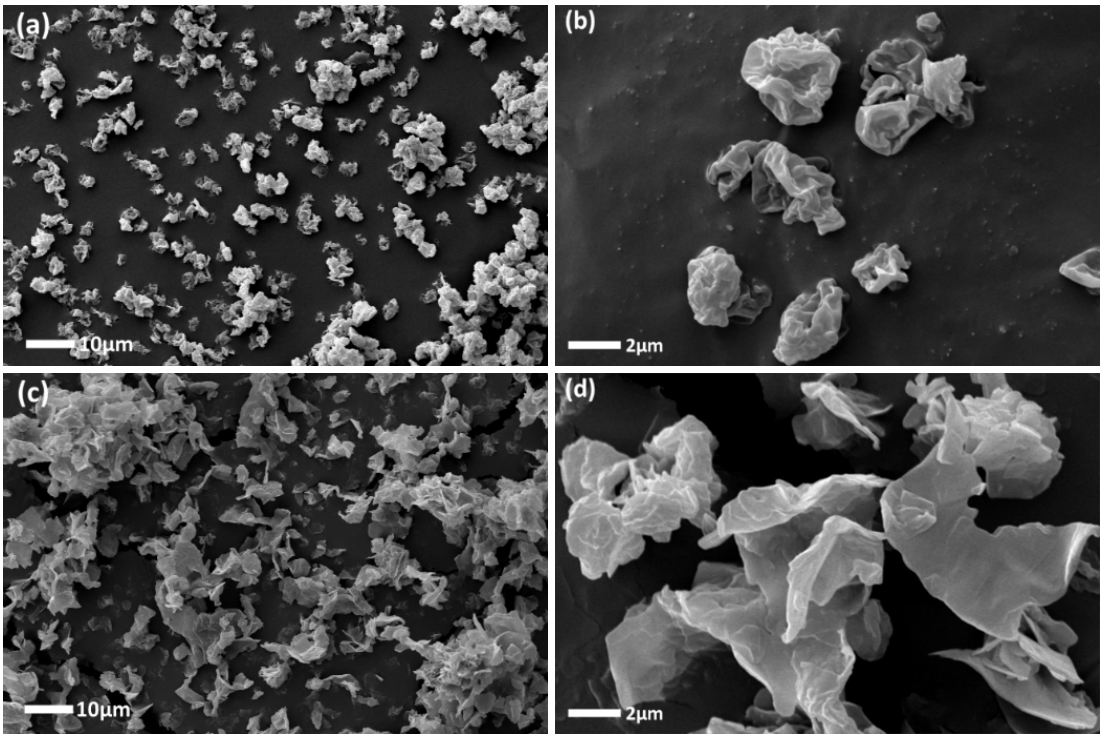

Figure 2.14. SEM images of DSPC particles extracted from the fresh (a – b) and the aged (c – d) suspensions show significantly different morphologies and dimensions.

Particles before and after aging were also measured with Raman spectroscopy and compared to the spectrum of DSPC precipitated from its solution. Recorded Raman spectra are presented in **Figure 2.15**. Differences in the measured Raman spectra verify that the phospholipid particles underwent structural changes during the aging study. In a comparison between the fresh, aged, and

precipitated DSPC particles, spectra of the aged and slowly precipitated DSPC particles showed sharper peaks in the fingerprint region (200 – 1000 cm^{-1}), indicating a more ordered structure, while broadened peaks observed in the spectrum of the freshly spray dried particles represent a greater level of disorder (Wang et al., 2014). An increase of the peak intensity ratio of the peaks at 1460 cm^{-1} and 1436 cm^{-1} in the CH_2 deformation region (1400 – 1500 cm^{-1}) from 0.73 to 0.79 during the aging study further proves an increase of lattice order in the lipid particles (Goodrich et al., 1991). The greater level of disorder in the fresh DSPC particles was likely caused by the rapid spray drying process in which the DSPC molecules, reaching saturation concentration in evaporating ethanol droplets, did not have enough time to achieve their most stable solid phase before collection of the dried particles (Vehring et al., 2007). While suspended in the propellant, the DSPC molecules gained a certain level of mobility and reoriented to form their more favored layered structure, as shown in the SEM images.

The dimensions of the lipid sheets are much larger than the originally spray dried particles. As a consequence, these re-formed now larger particles cream much faster, mostly because of the dependence of settling velocity on particle size described in **Eqn.(1.1)**. Even though the suspension destabilized rapidly within minutes, the new suspension tester was still able to provide an adequate resolution (1.0 fps) and instability indices with high sensitivity to suspension stability changes to resolve the whole creaming and clarification processes, a capability not currently afforded by any commercially available instruments.

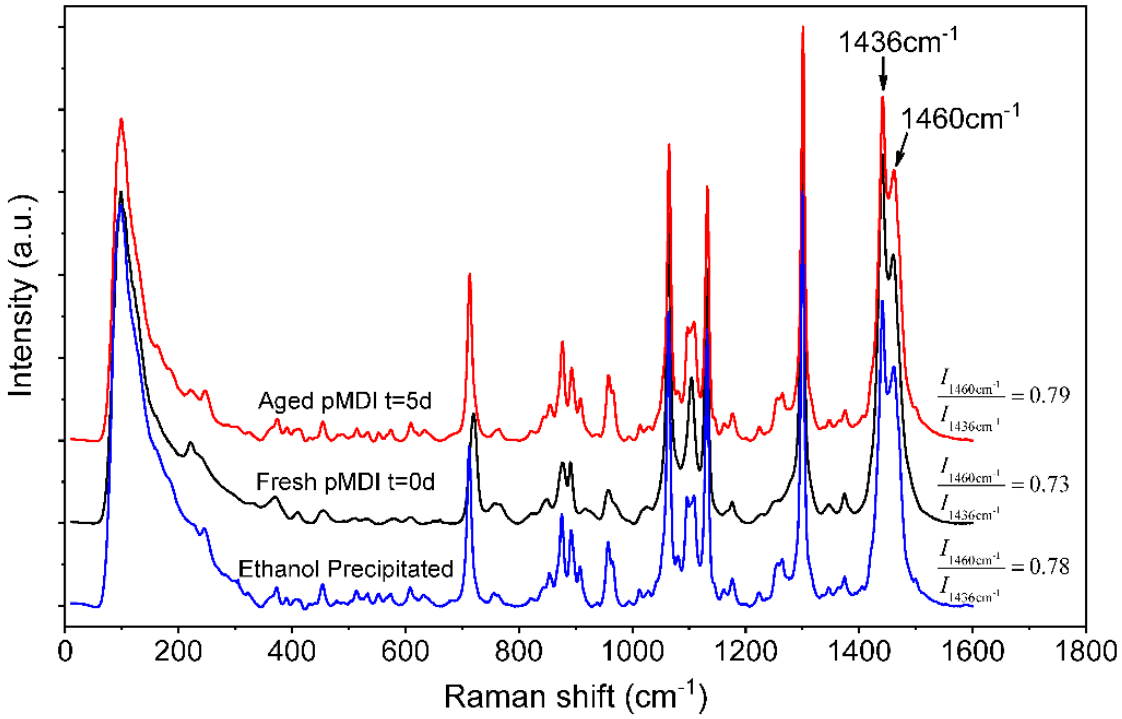

Figure 2.15. Raman spectra of fresh (t = 0 d) and aged (t = 5 d) DSPC particles compared to the more ordered DSPC standard precipitated from its ethanolic solution indicate increased solid phase order during aging of the suspension. Spectra are offset vertically for comparison purpose.

2.4. Conclusions

In this chapter, a new instrument based on shadowgraphic imaging and associated procedures that allow quantitative stability analysis of pressurized pharmaceutical suspensions was introduced. The designed setup offers a wide range of temporal resolution from 0.001 to 100 Hz that is suitable for measuring both stable samples and, most importantly, suspensions that destabilize relatively quickly within minutes, an objective currently very difficult to achieve with any other stability analysis instruments. Furthermore, the high spatial resolution enables simultaneous whole-sample illumination and image acquisition without any delay while still recording destabilization processes with abundant local details. The developed normalized relative transmission can now be used to quantitatively describe the detailed destabilization processes of

suspensions. The instability index provides a single parameter that accounts for the transmission changes during the sample destabilization and is especially useful in comparing and rank-ordering the stabilities of multiple samples. Selected applications of the pressurized pharmaceutical suspensions demonstrate the instrument's suitability as a routine tester of physical stability, having the advantages of simultaneous illumination, fast acquisition rate, convenient cross-sample comparison, which can be a very valuable characterizing technique in the development of stable pharmaceutical suspensions. Its accurate determination of the required HLB value of sunflower oil not only verifies the shadowgraphic imaging methodology but also proves that the technique can be applied to the stability analysis of emulsion systems with confidence, thereby demonstrating a potential that extends well beyond the analysis of pharmaceutical suspensions. It can be expected that the new stability characterizing technique will have great value in areas where multiphase systems are frequently encountered and their stabilities are of great importance, for example, the food and beverage industry, the cosmetic industry, and the oil sands industry.

CHAPTER 3 Effects of Agitation Method on Pharmaceutical Suspension Stability

With the shadowgraphic imaging technique developed in CHAPTER 2, effects of the initial agitation method are discussed here to ensure that standardized and comparable colloidal stability testing results can be produced. Three agitation methods, wrist action shaking, vortex mixing, and ultrasonic agitation, were used to disperse custom-made model suspensions with a wide range of colloidal stability. It was demonstrated that the measured suspension stability is highly dependent on the employed agitation method, with ultrasonic agitation being the most efficient in dispersing the aggregated particles to their primary sizes in order to achieve their desired suspension stability. It is therefore recommended that cross-sample stability comparisons be based on consistent initial agitation and that suspension stability analysis results be presented together with a detailed description of the applied agitation method for any measurement of suspension stability to be fully meaningful. From the perspective of instrument design, a built-in ultrasonic bath was prototyped for controlled and quantified sample agitation and is presented with its application to commercial pMDI suspension stability testing.

3.1. Introduction

The colloidal stability of pharmaceutical suspensions contained in pressurized metered dose inhalers (pMDIs) is a crucial attribute for considerations of dosing uniformity (Ivey et al., 2015) and subsequent product quality. It is essential that the colloidal stability of the suspensions be carefully characterized during the stage of formulation development. Due to the inherently unstable nature of suspensions, especially pharmaceutical suspensions in non-polar propellants, any suspension stability measurements must be preceded by a redispersion process to agitate the

creamed or settled particles. Commercial instruments including Turbiscan (Mengual et al., 1999b) and LUMiSizer (Lerche and Sobisch, 2007) have been widely applied to colloidal stability testing, but the impact of initial agitation on the resultant suspension stability has rarely been discussed, and neither of these instruments offers controlled initial agitation for test samples. The dispersion mechanisms of commonly used agitation devices are reviewed here.

Patients prescribed with suspension-based medications such as injectables, pMDIs, and nasal sprays are usually instructed to shake the drug containers vigorously before application. The shaking motion disperses aggregated particles by creating turbulence in the continuous liquid medium that exerts temporary instantaneous drag forces on the agglomerates in different directions to pull them apart (Wang et al., 2018a). Vigrous shaking also creates different patterns of turbulence, exposing the aggregates to eddies that accelerate the aggregates along rapidly changing directions. These accelerations, when large enough, may create internal forces within the aggregates that are larger than the particle adhesive forces, leading individual particles to break off from the aggregates (Finlay, 2001). The magnitude of the drag forces depends on the turbulent fluctuating velocities. A wrist action shaker is a lab-scale instrument commonly used to simulate the mild manual shaking motions with relatively good reproducibility.

A vortex mixer, or vortexer, is another lab-scale device commonly used to mix liquids, solutions, and suspensions in small vials. Vortex mixing of suspensions creates vortices inside the liquid phase, causing shear rates and exerting drag forces on the aggregated particles that can be much larger than the forces created by a simple shaking motion (Kundu et al., 2012). Usually, the vortexer has variable speed settings ranging from 100 to more than 3000 rpm to adjust the output dispersing energy.

Ultrasonic agitation, or ultrasonication (Taurozzi et al., 2011), is the most widely used technique for the dispersion of a wide range of suspended materials in the fields of medicine, biotechnology, energy, environmental remediation, and so on. Ultrasonication is usually referred to as the application of acoustic waves in the ultrasonic frequency range, typically 20 – 40 kHz, to suspended materials in a liquid phase for various purposes such as dispersion (Sato et al., 2008), dissolution (Passerini et al., 2006), cleaning (Lamminen et al., 2004), and catalysis (Ramachandran et al., 2013). Regardless of the configuration of the sonication device—whether as a probe, bath, or cup—there must be a piezoelectric transducer that converts electrical energy to vibrational mechanical energy, which is then transmitted to the liquid medium as acoustic waves in alternating high and low-pressure cycles (Ensminger and Bond, 2011). Micro-turbulences caused by the fluctuation of the alternating pressures can lead to limited aggregate dispersion; more important to the highly effective dispersion of ultrasonication is the process called cavitation (Sesis et al., 2013). Small vacuum bubbles can be generated during the low-pressure cycles when a cavitation threshold is exceeded by the acoustic energy. These microscale bubbles can penetrate into the gaps between the aggregated particles or even be generated in-situ, and then collapse and implode during the high-pressure cycles (Ensminger and Bond, 2011). The high-intensity energy and shock waves released by the implosion can create localized extreme conditions such as temperatures up to 10,000 K, rapid temperature change > 10^5 K/s, pressure bursts up to MPa, and liquid jet streams up to 400 km/h (Taurozzi et al., 2011), resulting in to the effective dispersion of aggregates.

In this Chapter, three different initial agitation methods—wrist action shaking (WAS), which simulates the manual shaking motion of pMDI users, vortex mixing (VM), which delivers moderate shear rate, and ultrasonic agitation (UA), which provides the most effective dispersing capability—are tested using different formulations and the results compared. Monodisperse spray-

dried saccharide particles are used to make model suspensions for testing to avoid the potential complications introduced by polydisperse particles, and three commonly used propellants with different liquid densities are used to make suspensions with a wide range of colloidal stabilities to prove universal applicability.

3.2. Materials and Methods

3.2.1. Materials

Two disaccharides commonly used as an excipient in respiratory drug delivery, D-(+)-trehalose dihydrate (177613, Fisher Scientific Co., Ottawa, ON, Canada) and α-lactose monohydrate (L3625, Sigma–Aldrich Corp., St. Louis, MO, USA), were selected to spray dry spherical and solid model particles (Vehring et al., 2007) for the suspension stability testing. Three propellants with different liquid densities, HFO1234ze (Solstice® R1234ze, Honeywell Int. Inc., Buffalo, NY, USA), HFA134a (GDR134a, Gregg Distributors Ltd., Edmonton, AB, Canada), and HFA227ea (Solkane® 227, Hannover, Germany), were used to prepare suspensions with different particle settling velocities and therefore different suspension stabilities. The densities of the saccharides (Elversson and Millqvist-Fureby, 2005; Kaialy et al., 2011; Zhang and Zografi, 2001) and propellants (Myrdal et al., 2014) are listed in **Table 3.1** and were used to calculate the particle settling velocities according to Stokes' law as described in **Eqn.(1.1)**.

Table 3.1. Suspension formulations used for colloidal stability testing. Particle settling velocities (v_S) were calculated based on the measured aerodynamic particle sizes and propellant properties at 20 °C.

Particle	Propellant	ρ_P (g/cm^3)	ρ_L (20°C, g/cm^3)	*MMAD* (µm)	*GSD*	v_S (mm/min)	Replicates
Trehalose	227ea	1.53±0.02	1.41	10.60	1.10	1.08	×2
	134a		1.23			3.41	×2
	1234ze		1.18			4.08	×2
Lactose	227ea	1.52±0.05	1.41	10.90	1.13	1.10	×2
	134a		1.23			3.61	×2
	1234ze		1.18			4.32	×2

3.2.2. Methods

3.2.2.1. Monodisperse spray drying

To avoid the potential complications introduced by polydisperse particles, a monodisperse spray drying technique (Azhdarzadeh et al., 2016) was used to prepare uniform model particles for the suspension stability testing. The experimental setup for monodisperse spray drying includes a custom-designed micro-jet atomizer (Azhdarzadeh et al., 2016) integrated with a custom laboratory scale spray dryer (Ivey et al., 2018). As shown in the schematic in **Figure 3.1**, the micro-jet atomizer was used to generate monodisperse droplets of feed solution. A pressurized liquid solution was supplied to the nozzle head from the feed line and fed through a micro-orifice to form a liquid micro-jet. Since the random breakup of liquid jets due to surface tension usually leads to polydisperse droplets, a piezoelectric ceramic ring (105261, Meggitt A/S, Denmark) was attached to the nozzle head to force regular disintegration of the liquid jet into monodisperse droplets

(Sirignano and Mehring, 2000). The piezoelectric transducer was driven by a function generator (DS340, Stanford Research Systems, CA, USA) supplying square waves with a peak-to-peak voltage of 20 V and frequencies ranging from 120 kHz to 160 kHz. The dispersing gas supplied through the orifice cap was used to disperse the droplet chain to avoid droplet collisions. A more detailed description of the atomizer can be found elsewhere (Azhdarzadeh et al., 2016). The generated monodisperse droplets were then dried in a lab-scale spray dryer and the resulting particles collected using a stainless-steel cyclone.

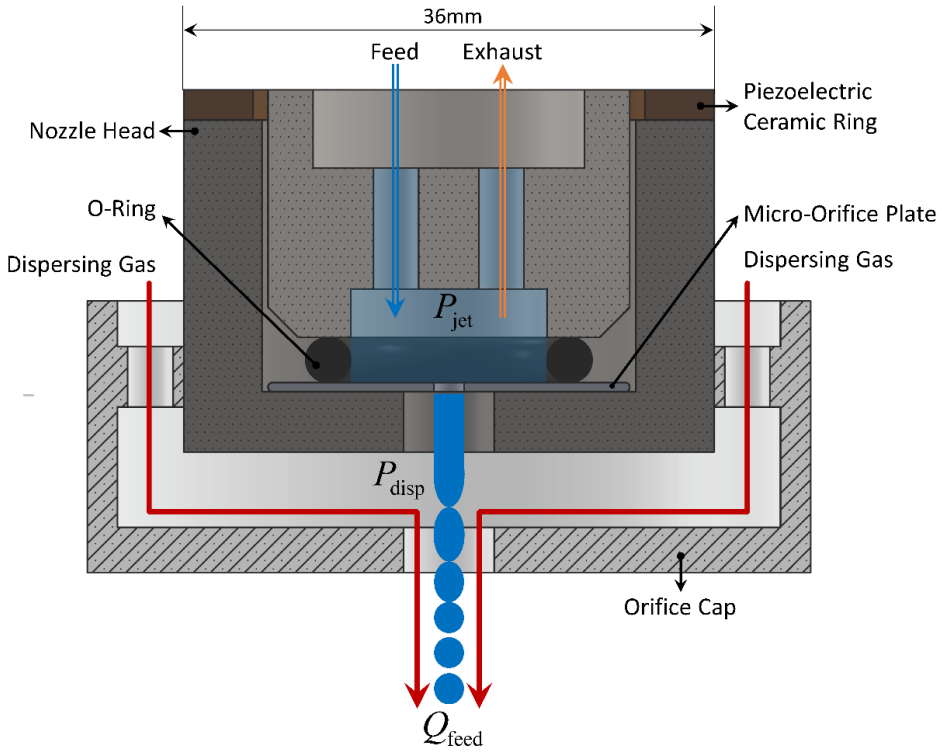

Figure 3.1. Schematic of the monodisperse micro-jet atomizer. The piezoelectric ceramic ring introduces vibration to the atomizer and forces the micro-jet to disintegrate regularly to monodisperse droplets. Dispersing gas supplied through the orifice cap prevents droplets from colliding into doublets or triplets.

To prepare particles used for this study, aqueous solutions of pure trehalose and lactose at a fixed concentration of 5 mg/mL were pressure-fed (500 ± 50 kPa) through a 30 µm orifice to form

the liquid micro-jet which subsequently disintegrated into monodisperse droplets. The inlet temperature of the drying chamber was set to 70 °C and the drying gas flow rate to 600 L/min for particle drying. Dispersing gas at a pressure of 240 kPa was supplied through a 3mm orifice to prevent the droplets from colliding. Particles collected by the cyclone were dried in a vacuum desiccator to remove any residual moisture and then transferred for further study. The aerodynamic particle size distribution and morphology of the dried particles were characterized using a time-of-flight aerodynamic particle sizer (APS, 3321, TSI, Shoreview, MN, USA) and scanning electron microscopy (SEM).

3.2.2.2. Pressurized suspensions

Pressurized suspensions consisting of different combinations of particles and propellants were prepared by first filling 50 mg ± 0.5 mg of the monodisperse spray-dried disaccharide particles into pressure-rated glass vessels. These were subsequently pressure filled with 18 mL ± 0.4 mL of propellants using a Pamasol propellant filler. A duplicate sample was prepared and tested for each combination of particle and propellant. All suspensions were sonicated for 30 s to break up any aggregated particles and then transferred for stability measurement.

A pressurized suspension contained in a commercial pMDI, Flixotide® 125 (125 µg/act fluticasone propionate in HFA-134a; Allen & Hanburys Ltd., Hertfordshire, UK), was also extracted for stability characterization. The original aluminum canister was first submerged in liquid nitrogen to freeze the propellant, and then the metering valve was quickly removed from the canister using a tubing cutter. Next, the frozen suspension was transferred to a standard glass vial and then crimped with the same Valois DF30 metering valve used for the DSPC suspensions. This suspension sample will hereafter be referred to as the ‘commercial suspension’.

3.2.2.3. Suspension stability measurement

The shadowgraphic imaging technique introduced in CHAPTER 2 (Wang et al., 2018a) that detects time-dependent changes in transmission intensity across the suspensions contained in transparent glass vials in a bright field was used for the suspension stability characterization. All the suspensions were observed for 30 minutes at 0.5 Hz for suspension stability immediately after 30 s agitation with the camera exposure time set to 0.12 ms and LED power set to 1.0 A. Each sample was tested three times for each agitation method. Detailed descriptions of the agitation process applied before each stability measurement are listed in **Table 3.2**. The normalized relative transmission profiles, $\Delta T_{t,h}^{N}$, introduced in **Eqn.(2.3)** and the dimensionless instability index, $\sigma(t)$, described in **Eqn.(2.4)**, were derived for each sample. The transmission profiles were used to reveal the destabilization process, while the instability index provides a single parameter that accounts for the transmission changes up to a specific time point of the destabilization and is especially useful in comparing and rank-ordering the stabilities of multiple samples.

For better comparison between multiple samples, the time for the instability index to reach 0.5, $\tau(\sigma = 0.5)$, was used as a quantitative suspension stability indicator, with the corresponding time constants for stable samples being longer than those for unstable ones. For the cases in which the instability indices did not exceed 0.5, a hill function in the form of **Eqn.(3.1)** was used to fit the instability index plot in which σ_{Max} is the predicted maximum instability index, and k and n are two fitting parameters controlling the shape of the plot. More details about the fitting are included in Appendix V. In all cases, a theoretical upper limit of 1.0 was set for the σ_{Max} during the fitting. Therefore, the time constant $\tau(\sigma = 0.5)$ was obtained directly by solving $\sigma(t) = 0$. Good fittings with adjusted R-squared values of $R^2 > 0.99$ were achieved for all cases. Standard deviation of the time constants for each sample was compared.

$$\sigma(t) = \sigma_{\text{Max}} \cdot \frac{t^n}{k^n + t^n} \tag{3.1}$$

Table 3.2. Methods and settings used for initial agitation of suspensions. "Osc/min" stands for oscillation per minute; "RT" stands for room temperature.

Agitation Method	Setting	Time (s)	Brand	Model
Wrist Action Shaking	385 Osc/min @ 15°, RT	30	Burrell Sci.	75-CC
Vortex Mixing	3200 rpm, RT	30	Fisher Sci.	02215365
Ultrasonic Agitation	100 Watts @ 42kHz, RT	30	Branson	2510-R-MTH

3.2.2.4. Built-in ultrasonic agitation – a prototype

Instead of using external devices for the initial agitation of the suspension samples, a built-in transparent ultrasonic bath was designed to provide controlled ultrasonic agitation to the samples of interest. Laser-cut thin sheets of clear cast acrylic (8560K257, McMaster-Carr, Cleveland, OH, USA) with a thickness of 3.2 mm were used as the front and back walls of the ultrasonic bath for their lower optical interference. The bottom and side walls of the tank were made with 4.8 mm-thick acrylic sheets (8560K219, McMaster-Carr) for greater mechanical strength. A piezoelectric ultrasonic transducer (BJC2560T-59HS-PZT-4, Beijing Ultrasonic Co. Ltd., Beijing, China) with a rated power of 60 W and a resonance frequency of 25 kHz was glued to the side wall of the acrylic tank to provide the ultrasonic agitation. As shown in the schematic in **Figure 3.2**, along with the suspension tester design introduced in CHAPTER 2, the ultrasonic bath is positioned in between the camera and the backlighting LED and is filled with 2.2 L of water during the experiment. A second output channel of the function generator, in combination with an RF amplifier (2100L, Electronics and Innovation Ltd, Rochester, NY, USA), supplies adjustable driving power to the transducer.

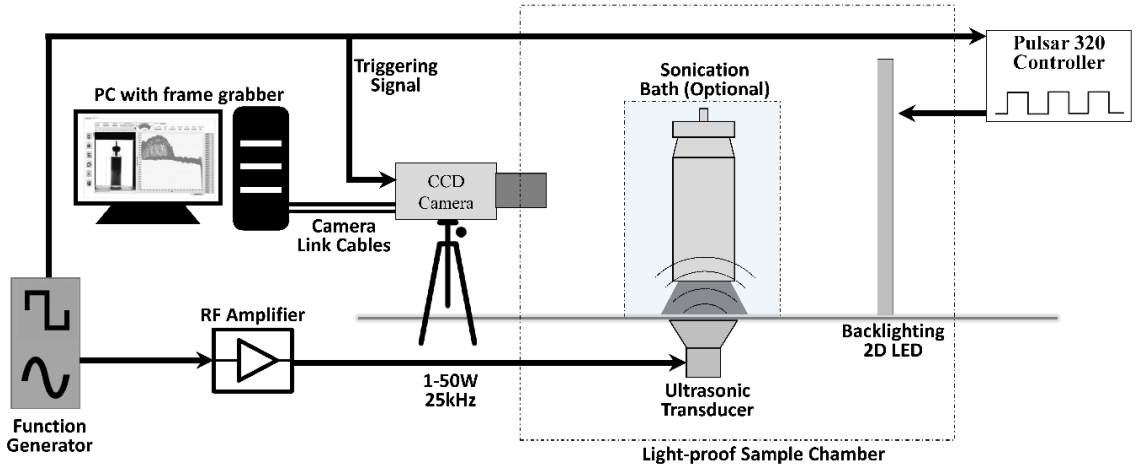

Figure 3.2. Schematic layout of the new suspension tester with the built-in ultrasonic agitation device.

The commercial suspension was tested as a proof of concept for suspension stability characterization based on in situ ultrasonic agitation and also to demonstrate the effects of initial agitation on the stability of suspensions, this time using the customized ultrasonic bath. Two sets of measurements with different agitation methods were conducted and their results compared. In one case, the suspension was first re-dispersed by continuous shaking on a wrist action shaker (Model 75, Burrell Sci., Pittsburgh, PA, USA) for 30 s to simulate the manual shaking motion of pMDI users, and the sample was then quickly submerged in the water bath immediately prior to measurement. In the other case, the suspension was first submerged in the water bath and then continuously agitated for 30 s by the ultrasonic transducer prior to measurement. The transducer was driven by a fixed input power of 42 W from the RF amplifier at its resonance frequency of 25 kHz. In both cases, the suspension stability was measured for 10 minutes at 1.0 Hz immediately after agitation with the camera exposure time set to 0.15 ms and LED power set to 1.0 A. Three repeated measurements were conducted for each agitation method.

3.3. Results and Discussion

3.3.1. Monodisperse spray-dried particles

3.3.1.1. Morphological analysis

According to the SEM images shown in **Figure 3.3**, spherical saccharide particles were produced from both trehalose and lactose solutions as expected, and their morphology resembles that of typical spray-dried sugar particles (Vehring et al., 2007). Therefore, uniform particles with the same size and morphology were produced using the monodisperse spray drying technique. Solid particles with little or no internal void space and particle densities close to the true densities of the raw materials are expected for both cases because of the low Peclet number ($Pe < 1$), which is a ratio of the solvent evaporation rate to the diffusion rate of solute commonly used as an indicator to predict the final particle morphology.

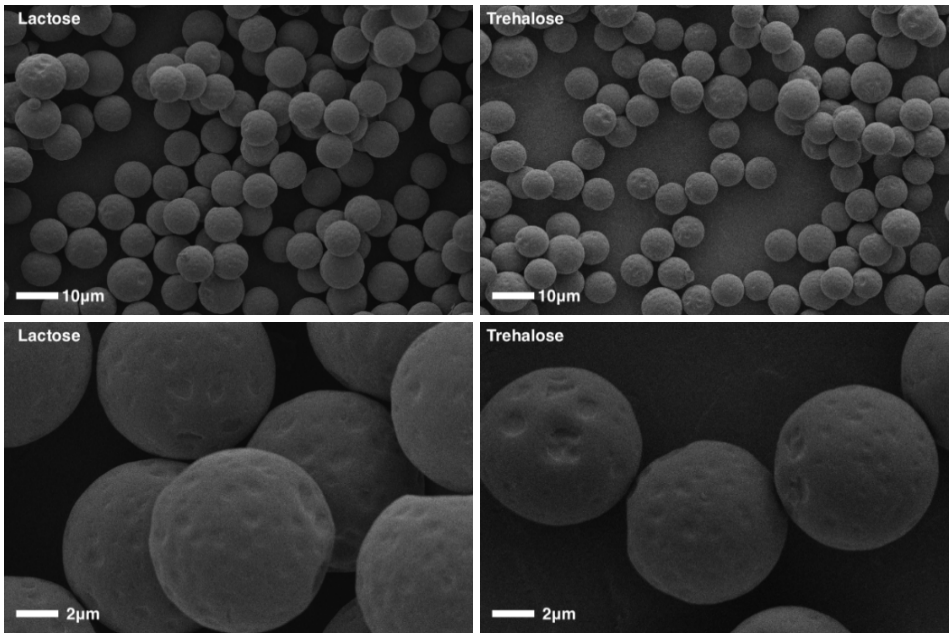

Figure 3.3. Monodisperse spray-dried trehalose and lactose particles show good uniformity and are spherical as expected.

3.3.1.2. Particle size distribution

Aerodynamic particle size distributions measured in-line by the time-of-flight aerodynamic particle sizer are presented in **Figure 3.4**. Both cases show very narrow geometric standard deviations (*GSD* < 1.2), proving that uniform particles with good monodispersity were produced and that these are also in good agreement with the morphological analysis results by SEM. Since the same 30 µm-orifice and a fixed 5 mg/mL solution concentration were used for the spray drying, both the trehalose and the lactose particles show close primary particle diameters.

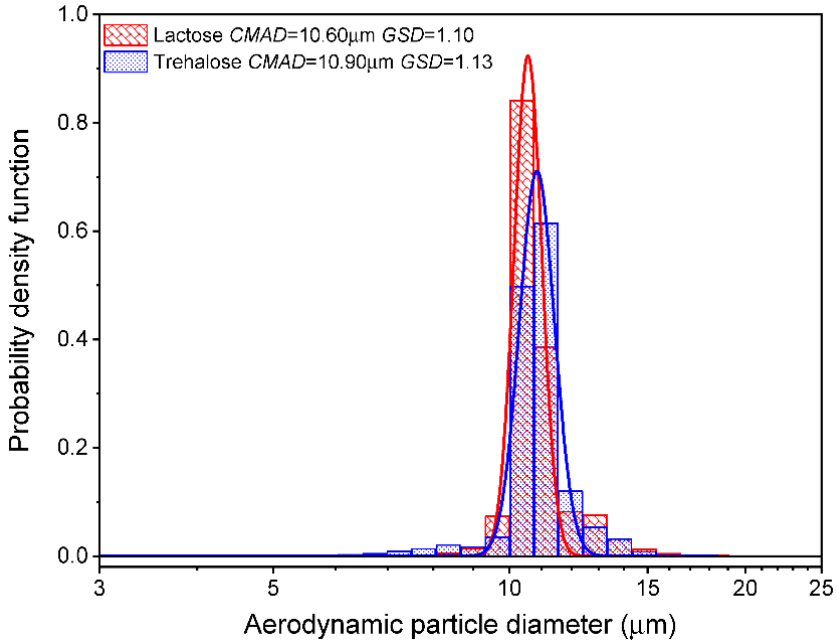

Figure 3.4. Aerodynamic size distributions of the spray-dried trehalose and lactose particles show high monodispersity with narrow distributions (*GSD* < 1.2) and similar particle diameters.

As an independent method of verifying the particle size distributions of the spray-dried particles, geometric diameters of more than 450 particles were measured from the SEM images of both trehalose and lactose by fitting the particle edges using circles (ImageJ 1.52d, NIH, MD, USA); the cumulative distributions are plotted in **Figure 3.5**. To compare the two independent size measurement results, the rearranged form of **Eqn.(1.1)** in the form of **Eqn.(3.2)** was used first to

convert the count-based volume equivalent diameters, d_{ve}, to the aerodynamic diameters, d_a, in which ρ_P is the particle density, ρ_0 is the unit density, and solid spherical particles were assumed ($\phi = 0$, $\chi = 1$). The aerodynamic diameters were calculated to be 10.8 µm and 10.4 µm based on the volume equivalent diameters for lactose and trehalose respectively, which also agrees well with the APS measurement, proving that the particles were monodisperse and their sizes were correctly measured separately. Particles smaller than the primary particle size are observed in the geometric size distribution of lactose and are likely caused by the formation of satellite droplets by the droplet generator, a known issue for the monodisperse spray drying technique (Ivey et al., 2018).

$$d_a = \sqrt{\frac{\rho_P}{\rho_0}} d_{ve} \tag{3.2}$$

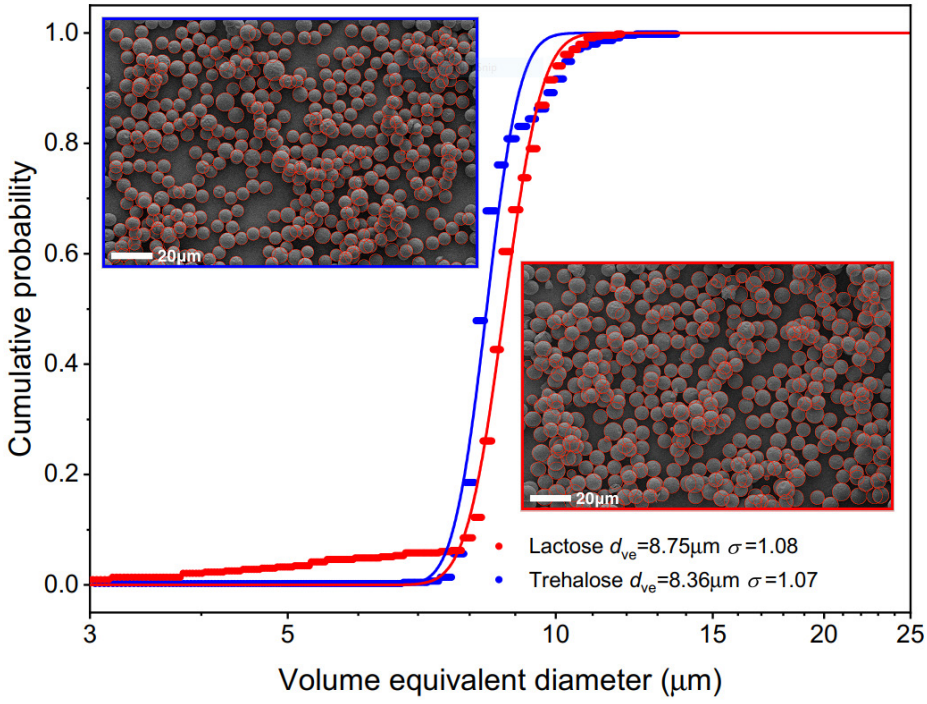

Figure 3.5. Cumulative volume equivalent diameter distributions of the spray-dried trehalose and lactose particles measured directly from the SEM images based on more than 450 particles.

3.3.2. Effects of agitation methods

3.3.2.1. Suspension stability comparison by transmission profiles

Both trehalose and lactose particles were suspended separately in three different propellants, HFA227, HFA134a, and HFO1234ze, producing the 6 different suspensions. Each suspension was tested three times in duplicate after each initial agitation method, i.e., the mild wrist action shaking, intermediate vortex mixing, and vigorous ultrasonic agitation. The normalized relative transmission profiles for the different combinations of suspension formulation and applied agitation method are presented in **Figure 3.6**, demonstrating the destabilization processes for each case. The change in transmission intensity at different time points of the stability measurement up to 30 minutes is represented by the different colors indexed in the color bar. Based on the profiles, sedimentation of particles happened in all cases as indicated by the reduced transmission intensities at the bottom of the vials. Clarification of the suspensions was also observed as the transmission intensity increased in the top regions of the samples for all cases. These results were expected since both trehalose and lactose have densities higher than the liquid propellants.

A notable dependence of the extent of clarification on the agitation method after 30 minutes was observed for the suspensions in HFA227, whose normalized transmission intensity changed the most: up to ~ 80% after wrist action shaking. However, the normalized change in transmission intensity was lower than 50% after ultrasonic agitation. Also, no such dependence was found for the suspensions is the other propellants, meaning a similar end state of the suspensions after 30 minutes regardless of the applied agitation method.

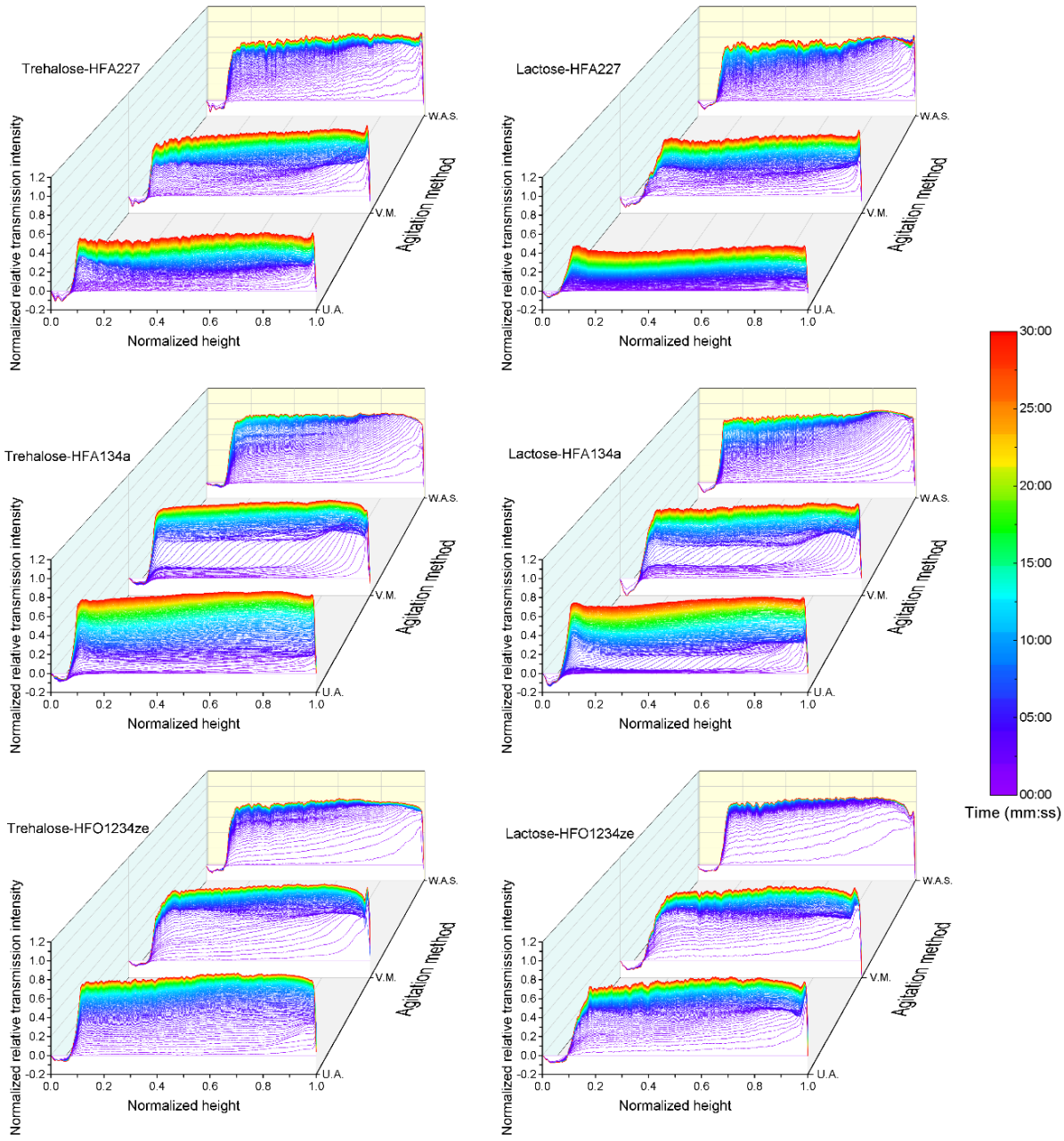

Figure 3.6. Normalized relative transmission profiles for different combinations of suspension formulation and applied agitation method.

The dispersion of the color profiles can be used as a qualitative way to evaluate the different rates of destabilization. Take the suspension with trehalose in HFA227 as an example: the evolving profiles stopped increasing 5 minutes after wrist action shaking, as indicated by the dominant

purple profiles in the plot. However, after vortex mixing and ultrasonic agitation, the profiles kept evolving for a longer time, as indicated by the more dispersed color profiles. A similar pattern was observed for all the other samples. Therefore, as anticipated, more agitation energy applied to the suspensions by different agitation methods did indeed slow down the rate of destabilization, especially for the samples in HFA227. The wavy profiles for some of the samples, e.g., lactose/trehalose-HFA227-WAS, indicate that aggregated particles adhered to the glass vials and did not settle to the bottom of the sample vessels, while smooth profiles, e.g., trehalose/lactose-HFA134a-VM/UA, indicate that no such glass wall adhesion was observed. These differences are likely related to the properties of the propellants. Thus, the transmission profiles can be used to reconstruct the destabilization processes of the suspensions in abundant detail.

3.3.2.2. Suspension stability comparison by instability index curves

Corresponding instability index plots derived from the above normalized relative transmission profiles are presented in **Figure 3.7**. Each combination of suspension formulation and applied agitation method was measured three times in duplicate, hence the 6 curves. The instability index values at a specific time point demonstrate the overall extent of destabilization for each sample and can be used for a stability comparison between different samples. The slopes of the instability index curves stand for the rate of destabilization. For all the cases, the instability index plots overlap well for repeated measurements, proving good repeatability of the samples and methods. Due to the whole-sample illumination configuration of the suspension tester and the high frame rate (0.5 Hz) used for the shadowgraphic image acquisition, the rapid destabilization process was well-resolved with high temporal resolution even for the suspensions in HFO1234ze, where the destabilization was completed within 1 – 2 minutes.

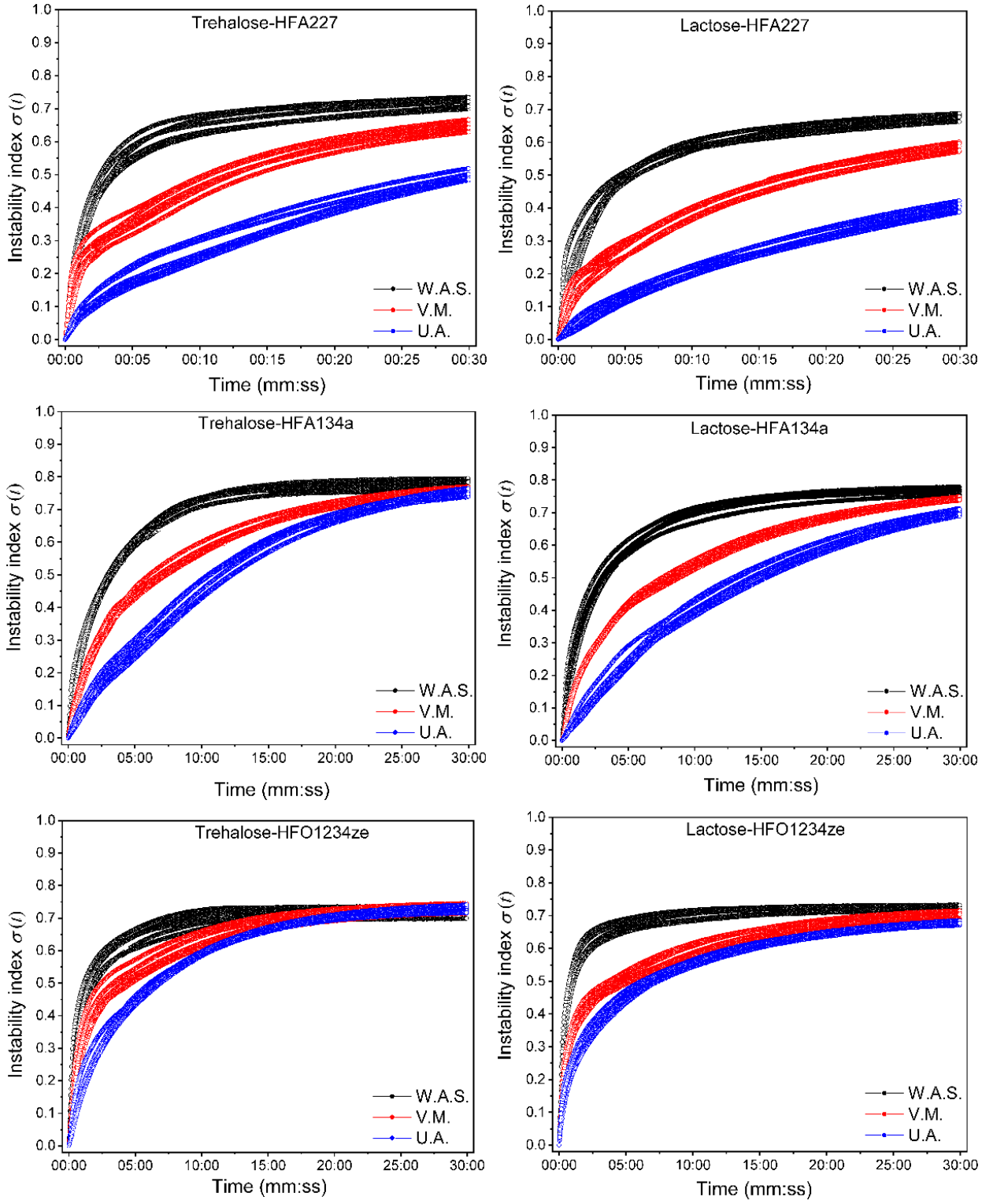

Figure 3.7. Instability index plot, $\sigma(t)$, for different combinations of suspension formulation and applied agitation method.

There is a clear dependence of the destabilization process on both the agitation method and the suspension formulation. In agreement with the observation from the transmission profiles, the instability indices after 30 minutes observation, $\sigma(t = 30\,\text{min})$, decreased substantially when more agitation energy was applied by switching from wrist action shaking to vortex mixing and ultrasonic agitation for the suspensions in HFA227, indicating improved colloidal stability. However, this parameter, $\sigma(t = 30\,\text{min})$, was not affected by the agitation method for the suspensions in HFA134a and HFO1234ze, implying a similar state of the samples after 30 minutes. Differences become more evident when all the instability index curves are compared. The rate of destabilization for all the suspensions slowed down to some extent when the agitation energy was increased, as indicated by the decreased slope $d\sigma(t)/dt$. The exact extent to which the suspension stability was affected by the agitation method varied from formulation to formulation: for example, the suspensions in HFO1234ze were less affected than the samples in HFA227. Therefore, the instability index plots are especially useful for quantitatively comparing the states of the suspensions at specific time points of the measurements and their rates of destabilization.

3.3.2.3. Formulation and agitation dependent suspension stability

In addition to the normalized transmission profiles for the detailed destabilization process comparison and the instability index plots for the quantitative rate of destabilization comparison, a time constant defined as the time for the instability index to reach 0.5, $\tau(\sigma = 0.5)$, was used as the single suspension colloidal stability indicator. Presented in **Figure 3.8** is a summary of the derived time constants for all the tested suspension formulations after different agitation methods. For more direct comparison, inset shadowgraphic images were added to show the states of the suspensions after 5 minute of observation.

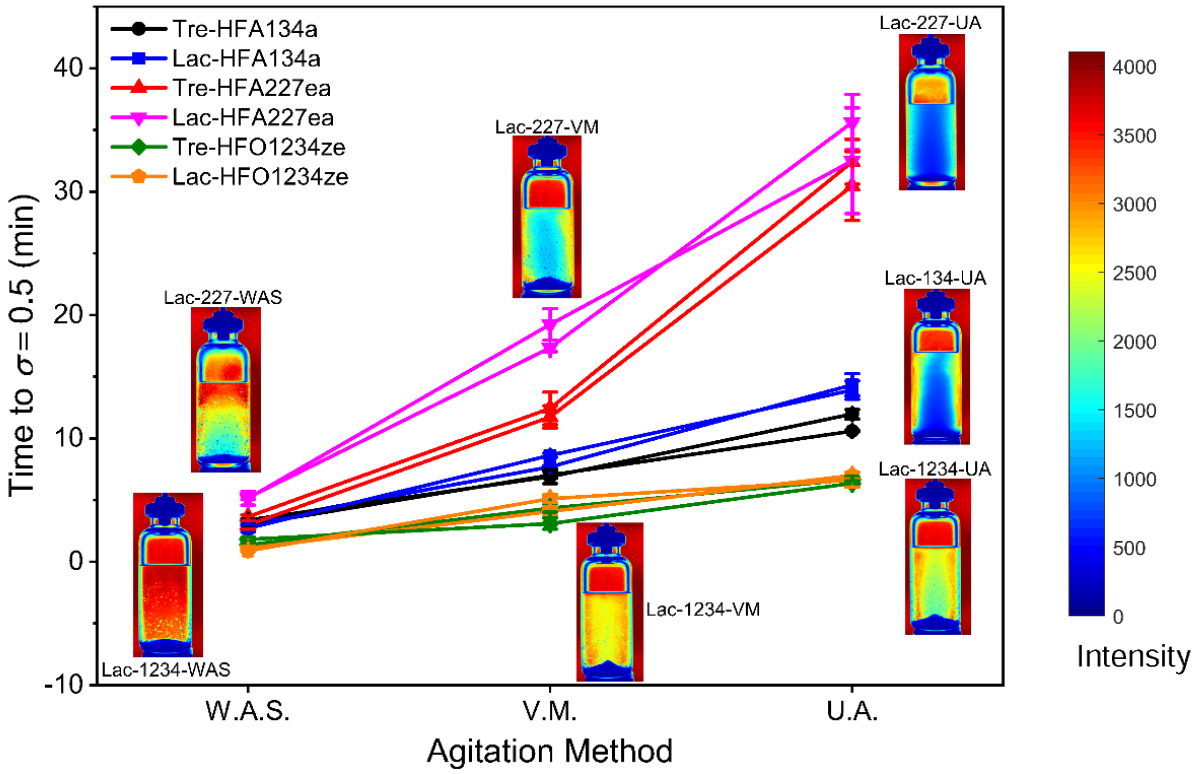

Figure 3.8. Time for the instability index to reach 0.5, τ (σ = 0.5), plotted against the agitation method for different suspension formulations. Inset shadowgraphic images show the states of the suspensions after 5-minute observation.

A clear dependence of suspension stability on the agitation method was observed when considering each suspension formulation. After wrist action shaking, all suspensions show similarly low stability, likely because aggregated particles were not fully dispersed and thus settled at high velocities regardless of the propellant type. Increasing the agitation energy by vortex mixing and ultrasonic agitation led to improved suspension stability, especially for the suspensions in HFA227ea. For these, the time constants increased from 4 min ± 1 min after wrist action shaking to 33 min ± 6 min after ultrasonic agitation, indicating a significantly improved suspension stability. Because ultrasonic agitation is much more efficient than shaking in breaking up large agglomerates, the greater extent of de-agglomeration introduced by the ultrasonic agitation led to

more stable suspensions. Less improvement of colloidal stability by higher agitation energy was observed for suspensions in HFA134a and HFO1234ze, likely because of the higher settling velocities for primary-sized particles in these propellants.

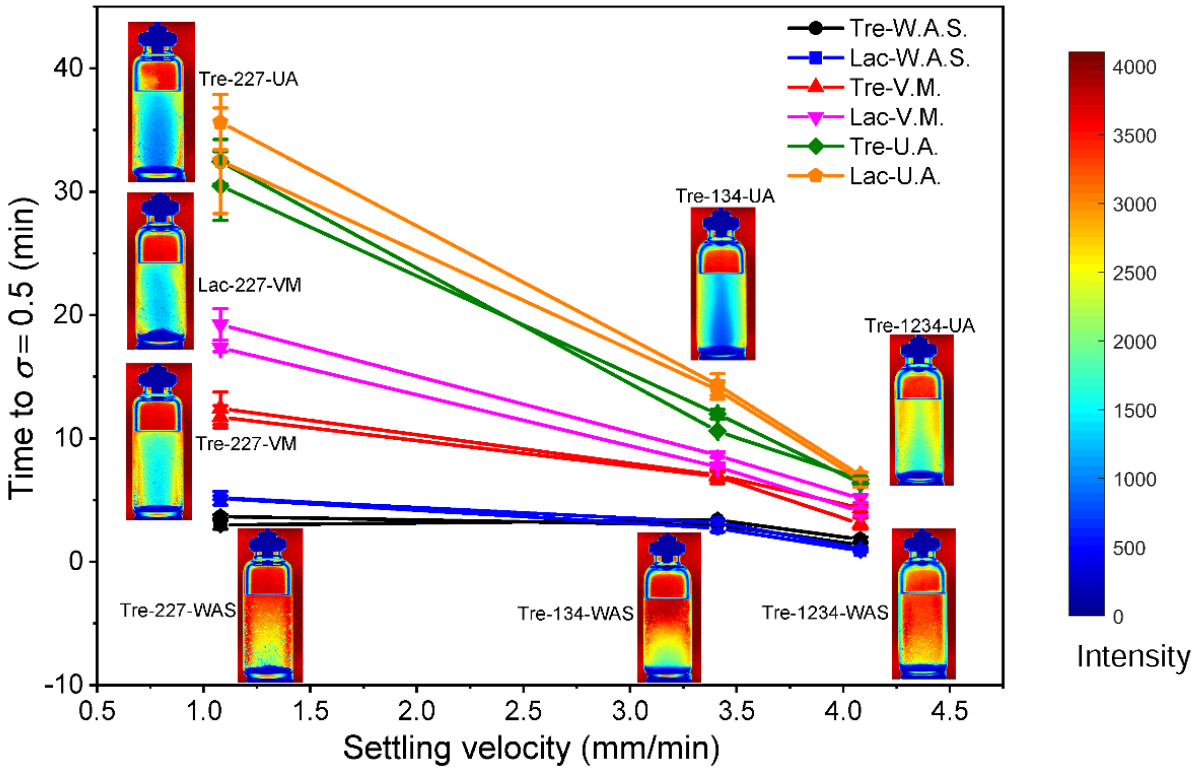

Figure 3.9. Time for the instability index to reach 0.5, τ ($\sigma = 0.5$), plotted against particle setting velocity/propellant for different agitation methods. Inset shadowgraphic images show the states of the suspensions after 5-minute observation.

By plotting the time constants against the particle settling velocity, which is equivalent to propellant type, as shown in **Figure 3.9**, a clear dependence of suspension stability on the propellant type can be observed when the same agitation method was applied. Lower particle settling velocities in HFA227 were correlated with more stable suspensions, especially when the particles were fully dispersed to their primary sizes using ultrasonic agitation. Such stability dependence on primary particle settling velocity was weakened when the suspensions were not

agitated enough using vortex mixing or wrist action shaking because larger particle aggregates settle at a significantly higher speed according to **Eqn.(1.1)**. The trehalose and lactose particles behaved similarly when suspended in the same propellant and agitated using the same method, indicating similar particle-propellant surface interactions.

3.3.3. Built-in ultrasonic agitation for stability measurement

It has been demonstrated that agitation method is crucial to the colloidal stability of suspensions. A built-in agitation device offering controlled ultrasonic agitation to the samples was prototyped and tested for an application. The single-component suspension (fluticasone propionate in HFA-134a) extracted from the commercial pMDI to the glass vial was agitated using two different methods and analyzed for 10 minutes to test the effects of the initial agitation method on its physical stability. Normalized relative transmission profiles for the two different scenarios of wrist-action shaking and ultrasonic agitation are plotted in **Figure 3.10**. The suspension destabilized rapidly after initial agitation by the wrist action shaker, with the top of the suspension quickly clarifying to ~ 60% of its maximum transmission intensity and the suspended particles settling to the bottom of the glass vial. The destabilization process was almost complete within the first minute even after 30s of vigorous wrist-action shaking. This timescale of suspension destabilization is comparable to that of a pMDI patient use scenario, meaning that the rapid destabilization can potentially cause inconsistencies between delivered doses if the pMDI is not agitated properly. To prevent such inconsistencies, the delivery devices need to be actuated shortly (< 10s) after shaking the pMDI canister to ensure that a representative aliquot of the bulk suspension fills the valve metering chamber for the subsequent dose. By comparison, the same suspension after ultrasonic agitation with the built-in transducer at 42 W for 30 s showed improved stability through weaker clarification, indicating much slower settling speed of suspended

particles; less than 10% of the maximum transmission intensity was reached at the end of the 10 min measurement.

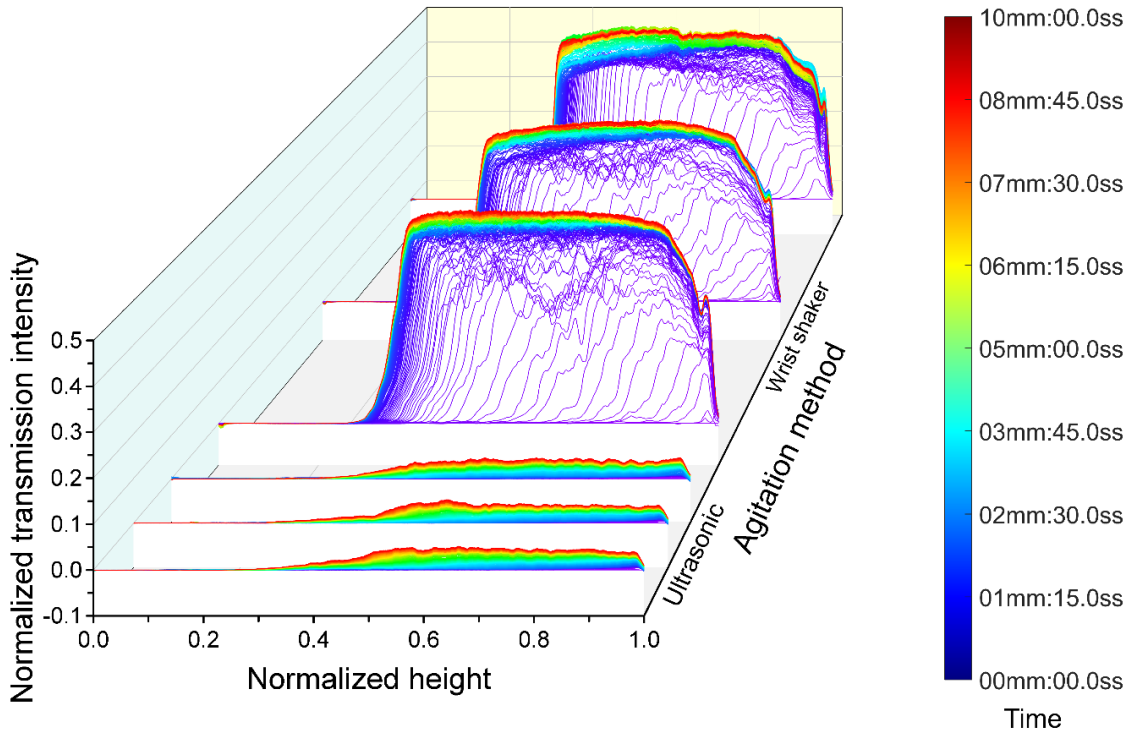

Figure 3.10. Normalized relative transmission profiles of pressurized suspension from a commercial pMDI show different stabilities when agitated differently.

As the instability index plots show in **Figure 3.11**, the suspension stability is significantly different after agitation by different methods. The improved suspension stability is likely due to the higher level of de-agglomeration after ultrasonic agitation. Wrist action shaking as an agitation method disperses agglomerated particles by creating turbulence in the propellant that exerts drag forces on the aggregates along different directions to pull the aggregates apart (Finlay, 2001). By contrast, dispersion by ultrasonic agitation is a consequence of microscale turbulence caused by the fluctuation of high and low pressures and, most importantly, cavitation. Cavitation refers to the phenomenon by which gas bubbles formed during low-pressure cycles collapse violently in high-pressure cycles (Sesis et al., 2013). Such bubbles can penetrate even into the void space of

loose aggregates. The extremely high-intensity energy released locally as microscale shockwaves during the bubble implosions can be very effective in disrupting suspended particle agglomerates (Taurozzi et al., 2011).

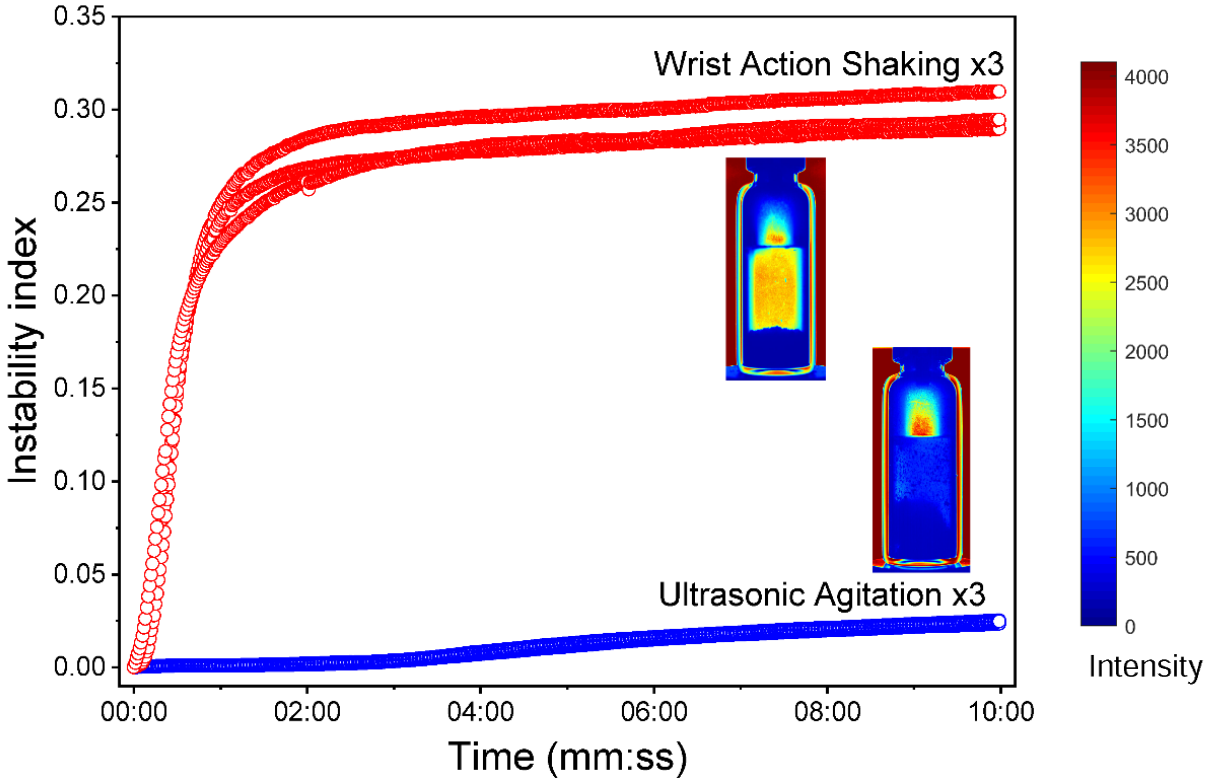

Figure 3.11. Instability index plot for analysis of commercial pMDI suspension after wrist-action shaking and ultrasonic agitation. Inset shadowgraphic images represent different end states of the suspension.

Since ultrasonic agitation is much more efficient in breaking up large agglomerates than is shaking, it is likely that the greater extent of de-agglomeration introduced by the ultrasonic agitation process led to smaller aggregates and particles. According to **Eqn.(1.1)**, these smaller particles move at much lower terminal settling velocities in the propellant than the less disassociated and larger agglomerates after wrist action shaking, hence the better suspension stability after ultrasonic agitation as presented in **Figure 3.11**. This example demonstrates that the

initial method of agitation can greatly affect the resultant suspension stability. Therefore, it is important that stability analysis be based on suspensions that have been agitated with quantifiable and controllable energy in order to produce reliable and comparable results of stability analysis, which, currently, cannot be achieved by any other instruments.

3.4. Conclusions

The effects of initial agitation method on suspension stability were assessed using the shadowgraphic imaging method introduced in CHAPTER 2. Three agitation methods delivering different dispersing energies were evaluated to study their effects on the colloidal stability of custom-made model pMDI suspensions. A clear dependence of the suspension stability on the employed initial agitation method was observed. The same suspension can have significantly different colloidal stabilities when agitated differently. Therefore, it can be concluded that colloidal stability testing of suspensions must be based on quantified initial agitation energy or at least consistent agitation method. Moreover, suspension stability analysis results must be presented together with a detailed description of the applied agitation method for any measurement of suspension stability to be fully meaningful. As a solution, a built-in ultrasonic agitation bath was prototyped and tested using a commercial pMDI. The new suspension tester provides adjustable and controllable ultrasonic agitation to disperse the samples of interest, a feature crucial for producing consistent and reproducible stability analysis results. However, due to the high intensity of the localized forces involved with cavitation, the potential of particle fracture needs to be considered when this method is applied in routine stability analysis. Consistent stability testing results were obtained, proving this approach to providing controlled agitation for suspension stability measurements to be a promising one. However, measuring transmission intensities with the suspensions submerged in a liquid bath inevitably led to light transmitting multiple mediums

with different refractive indices—e.g., air, water, glass tube, acrylic wall—before being detected by the detector.

CHAPTER 4 Particle Surface Roughness Improves Colloidal Stability of Pressurized Pharmaceutical Suspensions

Selected effects of particle morphology on the colloidal stability of pressurized pharmaceutical suspensions are investigated in this chapter using monodisperse spray-dried particles produced by a custom-designed micro-jet atomizer. Suspension stabilities of the model suspension systems with pure trehalose particles were measured and compared to study the effects of particle size. It was found that suspension stability improved significantly as the particle size decreased. The surface properties of trehalose particles were then systematically changed by adding different amounts of trileucine as a shell former to the feed solutions while maintaining the particle size with a constant total solids concentration. The spray-dried particles became increasingly corrugated as the trehalose-trileucine concentration ratio decreased. With the stability change caused by particle size difference taken into consideration, the stability of suspensions with more rugose particles was found to be much higher than that of particles with smoother surfaces. Therefore, surface modification was demonstrated to be a promising method of improving the stability of pharmaceutical suspensions in pressurized metered dose inhalers.

4.1. Introduction

Despite the various approaches that have been developed to improve the colloidal stability of suspensions, the impact of particle morphology, including surface roughness, on suspension stability has received relatively little study. For dry powder inhalers, it has been demonstrated that the increased microparticle surface roughness was able to significantly reduce the particle adhesion and eventually improve their in vitro aerosolization performance (Adi et al., 2008). The adhesive and cohesive forces between particles have been measured using atomic force microscopy and

correlated to the stability of corresponding suspensions (Traini et al., 2005; Traini et al., 2007; Young et al., 2003). A study carried out by D'Sa et al. (D'Sa et al., 2014) demonstrated that spray-dried particles designed to contain greater numbers of internal void structures resulted in larger specific surface area, weaker inter-particle forces, and eventually suspensions with better physical stability in a model propellant.

Recently, it has also been shown that surface roughness is a major factor determining the cohesiveness of particles (Baldelli and Vehring, 2016). The cohesion forces between microparticles of differing roughness were measured and compared with various theoretical models, proving that surface roughness is the dominant factor affecting the cohesion forces between microparticles. This is because for real particle interactions, the protrusions and indentations on the particle surfaces that are larger than intermolecular spacings but smaller than the particle sizes can cause the actual interaction force to deviate significantly from the theoretical prediction described in **Eqn.(1.2)**, which assumes particles with perfectly smooth surfaces. A modified version is described in **Eqn.(4.1)**,

$$F_{\mathrm{VDW}} = -\frac{A_{\mathrm{H}}}{6D^2}\sum_{k=1}^{N}\left(\frac{r_1 r_2}{r_1 + r_2}\right) \quad (r_1, r_2 \gg D) \tag{4.1}$$

where r_1 and r_2 stand for the radii of the kth of the N total interacting asperities from two separate particles, shows that the van der Waals forces between two imperfect particles can be significantly reduced by the particle surface roughness as $\left(\frac{R_1 R_2}{R_1 + R_2}\right) \gg \sum_{k=1}^{N}\left(\frac{r_1 r_2}{r_1 + r_2}\right)$ for particles without elastic deformation, which is the case for particles in suspensions and are in loose contact (Finlay, 2001). Therefore, particles with high surface roughness will become orders of magnitude less cohesive. Since surface roughness can significantly reduce the attractive forces between two

interacting particles, the suitability of stabilizing pharmaceutical suspensions by intentionally introducing different levels of surface roughness to the suspended particles is investigated.

Studying the stability of suspensions with conventionally manufactured, polydisperse particles is complicated because the various size-dependent particles properties–e.g., settling velocity (DeCarlo et al., 2004), optical properties (Mengual et al., 1999b), and level of deaggregation upon agitation (Voss and Finlay, 2002)–can make it relatively difficult to analyze the effects of each individual factor on the suspension stability. To avoid the potential complication introduced by polydisperse particles, for the first time, with the help of a monodisperse spray drying technique, we modify the surface properties of the particles, in particular the rugosity, to study the effects of surface roughness on the colloidal stability of pressurized pharmaceutical suspensions. Findings of this work can be used as an effective approach to improve the colloidal stability of, but not limited to, pressurized pharmaceutical suspensions.

4.2. Materials and Methods

4.2.1. Materials

Trehalose is a disaccharide that can be spray dried into spherical, solid particles (Vehring et al., 2007). D-(+)-trehalose dihydrate (177613, Fisher Scientific Co., Ottawa, ON, Canada) was first dissolved in demineralized water to prepare feed solutions for subsequent spray drying of monodisperse particles. Trileucine is a surface-active amino acid that has been used to modify the morphology of spray-dried particles to produce low-density and non-cohesive particles for dry powder inhalers (Lechuga-Ballesteros et al., 2008). The crystalline trileucine used for feed solution preparation in this study was obtained directly from the supplier (BCBP2254V, Sigma-Aldrich Corp., St. Louis, MO, USA).

4.2.2. Methods

4.2.2.1. Monodisperse spray drying

The monodisperse spray drying technique introduced in CHAPTER 3 is also used here to produce particles as designed. Detailed spray drying parameters are listed in **Table 4.1**. The selected 30 µm micro-jet orifice in this study can be used to produce droplets in the range of 50 µm – 65 µm (Azhdarzadeh et al., 2016), depending on the liquid properties, piezoelectric ceramic driving frequency, pressure difference across the orifice, etc. The drying gas flow rate and drying temperature were set to ensure that the droplets were completely dried, and the cut-off size of the cyclone was smaller than the dried particles. A time-of-flight aerodynamic particle sizer (3321, TSI, Shoreview, MN, USA) was used in-line to check the monodispersity of dried particles during the spray drying process and to measure the aerodynamic size distributions of the produced particles (Ivey et al., 2018). All collected particles were dried in a vacuum desiccator to remove any residual moisture before preparation of pressurized suspensions for subsequent stability analysis.

Table 4.1. Parameters used for monodisperse spray drying.

Spray-drying parameter	Value
Micro-jet pressure	500 ± 50 kPa
Feed solution flow rate	0.8 ± 0.1 mL/min
Micro-orifice diameter	30 µm
Inlet temperature	70 °C
Outlet temperature	52 ± 0.5 °C
Disperser orifice diameter	3.0 mm
Dispersing gas pressure	240 kPa
Drying gas flow rate	600 L/min
Piezoelectric driving frequency	120 - 160 kHz

4.2.2.2. Particle design

Monodisperse solid model particles with similar surface morphology but of different sizes were first needed to study the effects of particle size on the suspension stability. Particles with different surface rugosity and of similar size were then designed to further study the effects of surface roughness on the colloidal stability of pressurized suspensions. The theory of particle formation during spray drying (Vehring, 2008; Vehring et al., 2007) was used to determine the compositions and process conditions required to achieve these targets.

During the drying process of solution droplets, a dimensionless Peclet number such that:

$$Pe_{\mathrm{i}} = \frac{\kappa}{8D_{\mathrm{i}}} \tag{4.2}$$

which is a ratio of the solvent evaporation rate, κ, to the diffusion rate of solute, D_{i}, and is usually used as an indicator to predict the final particle morphology. The Peclet number can be directly used to derive the surface enrichment for each component E_{i}:

$$E_{\mathrm{i}} = \frac{c_{\mathrm{s,i}}}{c_{\mathrm{m,i}}} \approx 1 + \frac{Pe_{\mathrm{i}}}{5} + \frac{Pe_{\mathrm{i}}^2}{100} - \frac{Pe_{\mathrm{i}}^3}{4000} \quad (0 \le Pe_{\mathrm{i}} \le 20) \tag{4.3}$$

which is defined as the ratio of the surface concentration, c_{s}, to the mean droplet concentration, c_{m}, with good accuracy for relatively low Peclet numbers (< 20). More substantial discussion of the relation between the Peclet number and surface enrichment can be found elsewhere (Boraey and Vehring, 2014). Depending on the nature of the solute, once a critical concentration, $c_{\mathrm{c,i}}$, e.g., saturation concentration or solubility ($c_{\mathrm{sol,i}}$) for crystallizing systems, true density ($\rho_{\mathrm{t,i}}$) for non-crystallizing systems, at the droplet surface is reached, the droplet solidification process will be triggered. The time it takes for each component to reach the critical concentration at the droplet

surface, $\tau_{c_{c,i}}$, depends on the droplet drying time, τ_D, and the ratio of these time scales can be defined in terms of the surface enrichment, E, and initial concentration, c_0 as:

$$\frac{\tau_{c_{c,i}}}{\tau_D} = \left[1 - \left(\frac{c_{0,i} \cdot E_i}{c_{c,i}} \right)^{\frac{2}{3}} \right] \tag{4.4}$$

in which the droplet drying time, τ_D, depends on the initial droplet diameter, d_0, and evaporation rate of the liquid phase, κ, as $\tau_D = d_0^2 / \kappa$.

Surface composition and morphology of particles produced in the spray drying process can therefore be predicted according to **Eqn.(4.2)**, **(4.3)** and **(4.4)**. A high Peclet number solute usually leads to high surface enrichment, early surface saturation, and subsequently hollow particles. Depending on the properties of the shell, the hollow particles may buckle or collapse to form wrinkled particles. The outcome for low-Peclet number systems differs: a component with a low Peclet number and high solubility will produce small surface enrichment throughout the whole droplet lifetime and eventually form homogeneous solid particles, as is the case for trehalose used in the current study. The characteristic time for the droplet to solidify is close to the droplet lifetime, making the dried particle density close to the true density of the solutes. However, for solution droplets with low Peclet number components but also low solubility, e.g., trileucine, the time to saturation, $\tau_{c_{sol},i}$, or true density, $\tau_{\rho_t,i}$, is short compared to the droplet lifetime, τ_D. Hence, the droplet surface becomes supersaturated early, leading to the nucleation of a solid phase and early formation of a surface shell. The shell may also later collapse in the drying process through lack of mechanical strength, forming wrinkled particles.

The two components used in this study, trehalose and trileucine, both have relatively low Peclet numbers ($Pe \approx 1$) under the spray drying conditions listed in **Table 4.1**. The difference is that trehalose is highly soluble in water with a solubility at 690 mg/mL, while trileucine has a very low solubility at 7 mg/mL. Three feed solutions of pure trehalose with different concentrations at 1 mg/mL, 5 mg/mL and 30 mg/mL, as listed in **Table 4.2**, were prepared and spray dried. The characteristic times for trehalose to reach its true density on the droplet surface are indeed close to the droplet lifetime with $\tau_{\rho_{t,\mathrm{Tre}}} / \tau_D > 90\%$ for all the cases. According to the particle formation theory introduced earlier, solid spherical trehalose particles are expected and to be used as model particles.

Feed solutions with a fixed total solids concentration of 5 mg/mL but different trehalose-trileucine ratios of 99.6:0.4, 99.0:1.0, and 95.0:5.0 were also spray dried to introduce different levels of surface roughness to the dried particles. The case with 0.4% trileucine and 99.6% trehalose corresponds to a special case in which the surface concentration of trehalose reaches its true density almost at the same time as trileucine reaches saturation on the droplet surface, meaning that the particle solidifies at the same time as the trileucine surface concentration reaches supersaturation. As presented in **Table 4.2**, trileucine reaches its saturation concentration at the end of the droplet drying process at 97.7% of the droplet lifetime, which is right after trehalose reaches its true density at the droplet surface at 97.5% of the droplet lifetime. Neglecting the effects of trileucine surface activity, trileucine is expected to form a thin film of layer on the surface at the exact time point when trehalose starts to solidify at the surface. Relatively smooth particles with a layered structure are expected for this case. According to the calculation, the other cases with more trileucine are expected to force earlier shell formation and produce particles with more surface rugosity.

Table 4.2. Feed solutions for monodisperse spray drying with calculated time for trileucine to reach surface saturation normalized by droplet lifetime, time for trehalose to reach true density normalized by droplet lifetime, and calculated true density of the mixture.

Feed Solution #	Trehalose (mg/mL)	Trileucine (mg/mL)	$\tau_{c_{sol,Tri}}/\tau_D$ (%)	$\tau_{\rho_{t,Tre}}/\tau_D$ (%)	$\rho_{t,mix}$ (g/cm^3)
1	1	-	-	99.1	1.53
2	5	-	-	97.5	1.53
3	30	-	-	91.7	1.53
4	4.98	0.02	97.7	97.5	1.53
5	4.95	0.05	95.7	97.5	1.52
6	4.75	0.25	87.4	97.6	1.50

4.2.2.3. Morphological and spectroscopic analysis

All monodisperse spray-dried particles before and after suspension in the propellant were analyzed using a scanning electron microscope (EVO M10, Zeiss, Germany) to confirm particle morphology For electron microscopy, all spray-dried particles were sampled on standard SEM pin mounts (Ted Pella Inc., USA) covered with double-sided adhesive carbon tape as substrates and further sputter-coated with gold nanoparticles (Desk II Sputter Coater, Denton Vacuum, NJ, USA). Particles suspended in the propellant were also extracted for SEM morphological analysis using a single-nozzle impactor designed for direct sampling of aerosol particles for subsequent characterization in a configuration shown in Appendix III (Wang et al., 2017b). A custom-designed macro-Raman spectrograph, which is similar to the spectroscopic system presented in Appendix IV, was used to verify the solid state of the dried particles (Wang et al., 2017a). Briefly, particles were loaded into the 0.2 μL-cavity of an aluminum sample holder. The Raman system

utilized a 671 nm diode-pumped laser (Ventus 671, Laser Quantum, UK) with a maximum power of 500 mW. All measurements were conducted under a nitrogen atmosphere at room temperature (21 ± 1 °C) and in dry conditions (< 3% RH). Raw materials received from the manufacturers were measured directly as the reference materials for crystalline leucine and trileucine, and spray dried trileucine and trehalose were used as their corresponding amorphous reference materials. A deconvolution process was used to determine the contributions of each component as summarized in **Eqn.(4.5)**, in which S_{Res} is the residual spectrum after subtracting all components, S_{Raw} is the raw spectrum of the mixture, B is the background signal, and $S_{i,\mathrm{N}}$ is the normalized reference spectrum of the pure component. The background signal is usually approximated as a linear function of Raman shift and subtracted during deconvolution. I_i can then be determined by iteratively minimizing the residual spectrum, S_{Res}. A detailed description of the Raman data analysis for the identification of each individual component has been described elsewhere (Wang et al., 2017a) and is therefore no longer reiterated here.

$$S_{\mathrm{Res}} = S_{\mathrm{Raw}} - (B + \sum I_i S_{i,\mathrm{N}}) \tag{4.5}$$

4.2.2.4. Particle size measurement

A time-of-flight aerodynamic particle sizer (APS) was used in-line during the spray drying processes to measure the size distributions of the dried particles. The particle sizer was set to operate at a standard flow rate of 5 L/min, taking a 20s-measurement every 5 minutes. Volume equivalent diameter distributions of the spray-dried pure trehalose particles were also measured by SEM image analysis assuming perfectly spherical particles and fitting the particle edges using circles (ImageJ 1.52d, NIH, MD, USA). More than 300 particles for each of the spray-dried trehalose batches were counted and measured to generate their corresponding count based

cumulative particle diameter distributions, a method possible only when the geometric standard deviation (*GSD*) of the particle size distribution is small. Aerodynamic particle size distribution and volume equivalent diameter distributions were compared to confirm monodispersity and correct size measurement for dried particles.

4.2.2.5. Specific surface area measurement

To quantitatively compare the difference of surface roughness between the spray-dried powders, their specific surface areas were measured using a 7-point BET (Brunauer–Emmett–Teller) (Rouquerol et al., 2014) method (Model ASIQCU000-5, autosorb iQ, Quantachrome Instruments, FL, USA). According to the BET **Eqn.(4.6)**:

$$\frac{1}{m\left(\frac{P_0}{P}-1\right)}=\frac{C-1}{m_0 C}\left(\frac{P}{P_0}\right)+\frac{1}{m_0 C} \tag{4.6}$$

where m is the weight of adsorbed gas at a relative pressure P/P_0, m_0 is the weight of adsorbate constituting a monolayer of surface coverage for each unit mass of the sample, and C is the BET constant that is indicative of the adsorbate-adsorbent interaction energy, the krypton adsorption isotherm is plotted as $1\Big/m\left(\frac{P_0}{P}-1\right)$ against P/P_0, leading to a linearized BET plot. From **Eqn.(4.6)**, the slope, s, and intercept, i, of the plot can be obtained as:

$$s=\frac{C-1}{m_0 C} \tag{4.7}$$

and

$$i=\frac{1}{m_0 C} \tag{4.8}$$

The weight of adsorbate gas for a monolayer coverage can therefore be calculated by combining **Eqns. (4.7)** and **(4.8)** that:

$$m_0 = \frac{1}{s+i} \tag{4.9}$$

and the BET constant is:

$$C = 1 + \frac{s}{i} \tag{4.10}$$

The specific surface area of the tested sample, S, can therefore be determined as:

$$S = \frac{m_0 N_A A_{cr}}{M_{Kr}} \tag{4.11}$$

in which N_A is the Avogadro's constant, A_{cr} and M_{Kr} is the cross-sectional area of a single adsorbate gas molecule and the gas molecular weight respectively.

For each test, 0.2 - 0.4 g of monodisperse spray-dried powder was first loaded into a sample cell (O.D. = 6 mm) and degassed at 50 °C for 30 - 120 minutes. Since relatively small specific surface areas were expected for the tested powder samples due to the lack of internal void space, krypton (M.W. = 83.80 g/mol) was used as the adsorbate gaseous phase and was assumed to have a single-molecule cross-sectional area of 20.5 Å^2. The krypton physisorption analysis was then conducted for a relative pressure (P / P_0) range of 0.05 - 0.35 at the boiling temperature of liquid nitrogen at -196 °C.

In addition to the specific surface area, the adsorbent-dependent BET constant C was also determined. The BET constant is known to be directly related to the adsorption energy for the first adsorbed layer and its value is an indication of the magnitude of the adsorbent/adsorbate interactions (Rouquerol et al., 2014). Therefore, the BET constant in this study was used as a piece

of secondary evidence to support that the surface compositions of the formed particles were as predicted by the theory of particle formation during spray drying.

4.2.2.6. Pressurized suspensions

Pressurized suspensions of the monodisperse spray-dried particles were prepared by weighing 50 mg ± 2 mg of the dried powders into a glass vial, crimping an aluminum metering valve (DF30, Valois Pharma, NY, USA) onto the glass vial, and then using a benchtop pMDI production station (2005/21, Pamasol Willi Mäder AG, Switzerland) to pressure-fill 22.0 g ± 0.5 g of HFA-227ea propellant (UN3296, Mexichem Fluor Inc., UK) through the valve into the vial. The glass vials used for stability measurement are custom-designed round, flat-bottomed borosilicate glass vessels (Adams & Chittenden Scientific Glass, CA, USA) measuring 75.5 mm in height and 27.5 mm in outer diameter, and featuring a 900 kPa pressure rating, with good transmissivity.

4.2.2.7. Suspension stability measurement

Suspension stabilities of the particles in propellant HFA-227ea were measured using the shadowgraphic imaging method developed by Wang as introduced in CHAPTER 2. The technique acquires high-resolution sequential images of suspensions contained in transparent glass vials in a bright field and performs post image processing to extract the time (t) dependent change of transmission intensity (T) at different heights (h) along the suspension, $\Delta T_{t,h}$, according to **Eqn. (2.2)**. The normalized relative transmission profiles, $\Delta T_{t,h}^{\mathrm{N}}$, are then calculated as:

$$\Delta T_{t,h}^{\mathrm{N}} = \frac{\Delta T_{t,h}}{\Delta T_{t,h}^{\mathrm{Max}}} = \frac{T_{t,h}^{\mathrm{a}} - T_{t_0,h}^{\mathrm{a}}}{T_{\mathrm{Clear}}^{\mathrm{a}} - T_{t_0,h}^{\mathrm{a}}} \tag{4.12}$$

in which $\Delta T_{t,h}$ is the relative transmission profiles for the change of absolute transmission, $T^{\mathrm{a}}_{t,h}$, relative to the initial transmission profile, $T^{\mathrm{a}}_{t_0,h}$. $\Delta T_{t,h}$ is then normalized by its maximum value, $\Delta T^{\mathrm{Max}}_{t,h}$, which is the difference between the transmission for clear propellant, $T^{\mathrm{a}}_{\mathrm{Clear}}$, and the initial transmission profile of the sample being tested, $T^{\mathrm{a}}_{t_0,h}$. The normalized relative transmission profiles, $\Delta T^{\mathrm{N}}_{t,h}$, provide semi-quantitative information about the whole destabilization processes with abundant local details. In addition, by integrating each of the normalized relative transmission profiles, $\Delta T^{\mathrm{N}}_{t,h}$, according to **Eqn.(2.4)**:

$$\sigma(t) = \int_{h=0}^{h=1} \left| \Delta T^{\mathrm{N}}_{t,h} \right| \tag{2.4}$$

a single parameter, termed the instability index, $\sigma(t)$, is derived to account for the overall transmission changes during the suspension destabilization processes and can therefore be used to quantitatively compare and rank-order the stabilities of different samples. The instability index, $\sigma(t)$, is a dimensionless number ranging from 0 for extremely stable samples to 1.0 for suspensions that destabilize completely to clear liquid at a time t, and its derivative $d\sigma(t)/dt$ indicates the rate of destabilization.

In this study, stabilities of all the suspensions were measured within the same day of propellant filling to avoid the effects of moisture ingress on the suspended particles. Immediately before each stability measurement, the suspensions were agitated for 30 s in an external small-scale ultrasonic bath (M1800H, Fisher Scientific Comp., Ottawa, ON, Canada) to redisperse the suspended particles and break up any aggregated particles. The suspension tester was set to acquire shadowgraphic images at a frame rate of 0.5 Hz and an exposure time of 0.50 ms. The backlight LED was operated at a driving current of 1.0 A with a pulse width of 1.0 ms. The stabilities of all

suspensions were measured for 30 min immediately after the ultrasonic agitation. The settings and operating procedures were kept consistent for all the suspension stability measurements. Three suspension samples were prepared for each batch of spray-dried particles and each suspension was measured three times.

4.3. Results and Discussion

4.3.1. Morphological and spectroscopic analysis

SEM images of particles produced under different conditions are shown in **Figure 4.1**. This figure highlights that uniform and spherical trehalose particles were produced using the monodisperse spray drying technique. Because of the low Peclet number of trehalose and its high solubility in water, these particles were expected to be solid inside with little or no internal void space, and with a density close to the true density of trehalose (Zhang and Zografi, 2001). With the micro-jet orifice kept the same for all the spray-dried batches, and the feed solution concentration increased from 1 mg/mL to 30 mg/mL, the diameters of the resultant particles also increased as designed. Dimples on the surfaces are typical to the spray-dried trehalose particles and have been reported before (Vehring, 2008), which may be caused by inter-particle collision during the cyclone collection.

Due to the low Peclet number and low solubility of trileucine, the addition of trileucine changed the morphologies of the spray-dried particles significantly as expected, as shown in **Figure 4.2**. These results prove that trileucine caused early surface enrichment and shell formation during the drying process of the monodisperse solution droplets. Starting from the spherical particles formed from the pure trehalose solution at the top of the figure, the particles become more wrinkled the more trileucine is added, a result similar to those observed in the literature (Lechuga-Ballesteros et al., 2008).

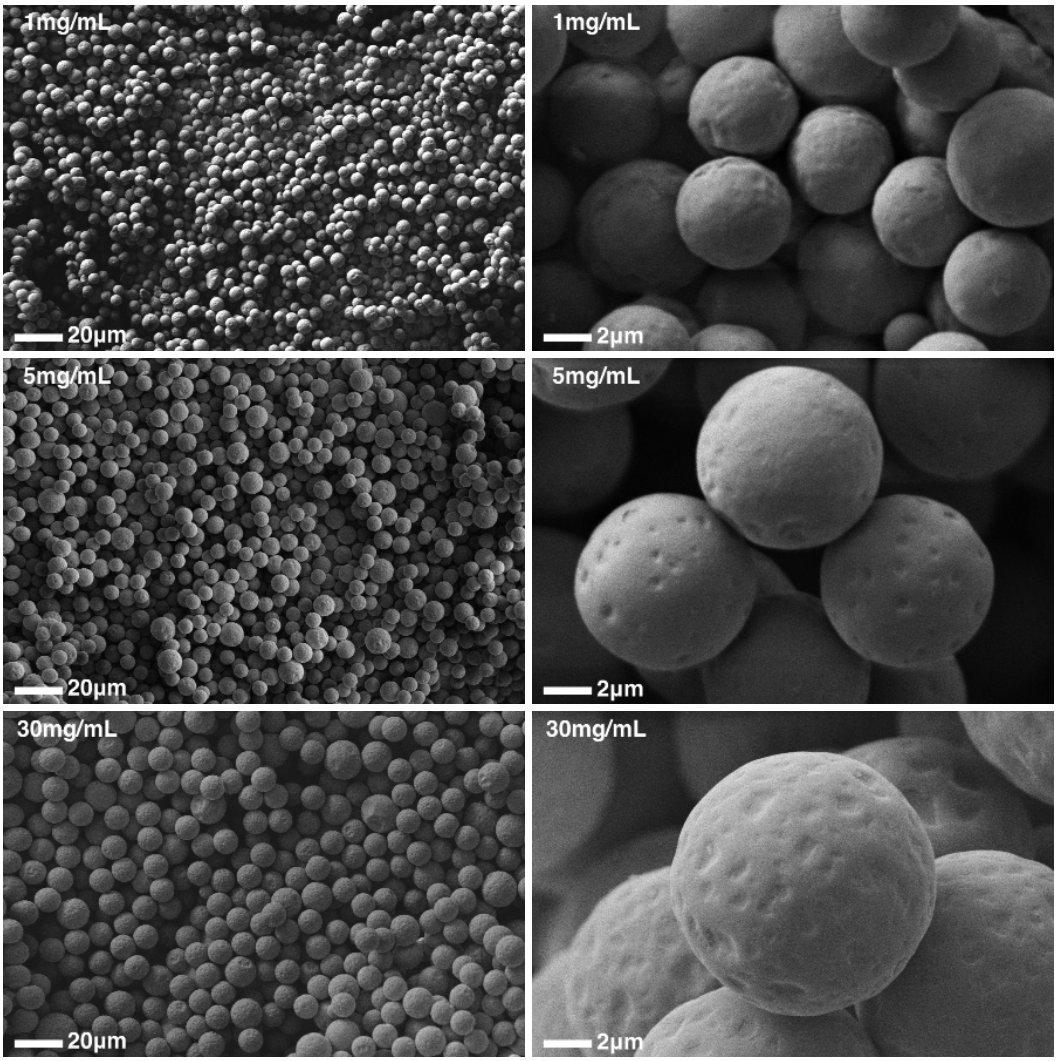

Figure 4.1. Morphology of the spray-dried pure trehalose particles shows a high level of sphericity and good monodispersity. Particle size increased with the feed solution concentration.

The special case of feed solution with 0.4% trileucine and 99.6% trehalose produced particles that were generally smooth with only a slightly increased rugosity, a result different from what has been reported and proving that the strategy to have trileucine and trehalose precipitate at roughly the same time to form a layered surface structure was successful. For the cases with 1.0% and 5.0% trileucine, trileucine shells were formed much earlier in the particle formation processes and collapsed later due to lack of mechanical strength, causing the particles to be more rugose, as planned. The theory according to Boraey and Vehring (Boraey and Vehring, 2014) allows a rough

estimate of shell thickness assuming that all the trileucine is on the surface. The thickness was estimated to be on the order of 10 nm, which Raman results later confirmed to be amorphous. Therefore, it is plausible that this thin shell had enough residual mobility to fold when formed initially and collapsed in the subsequent drying processes.

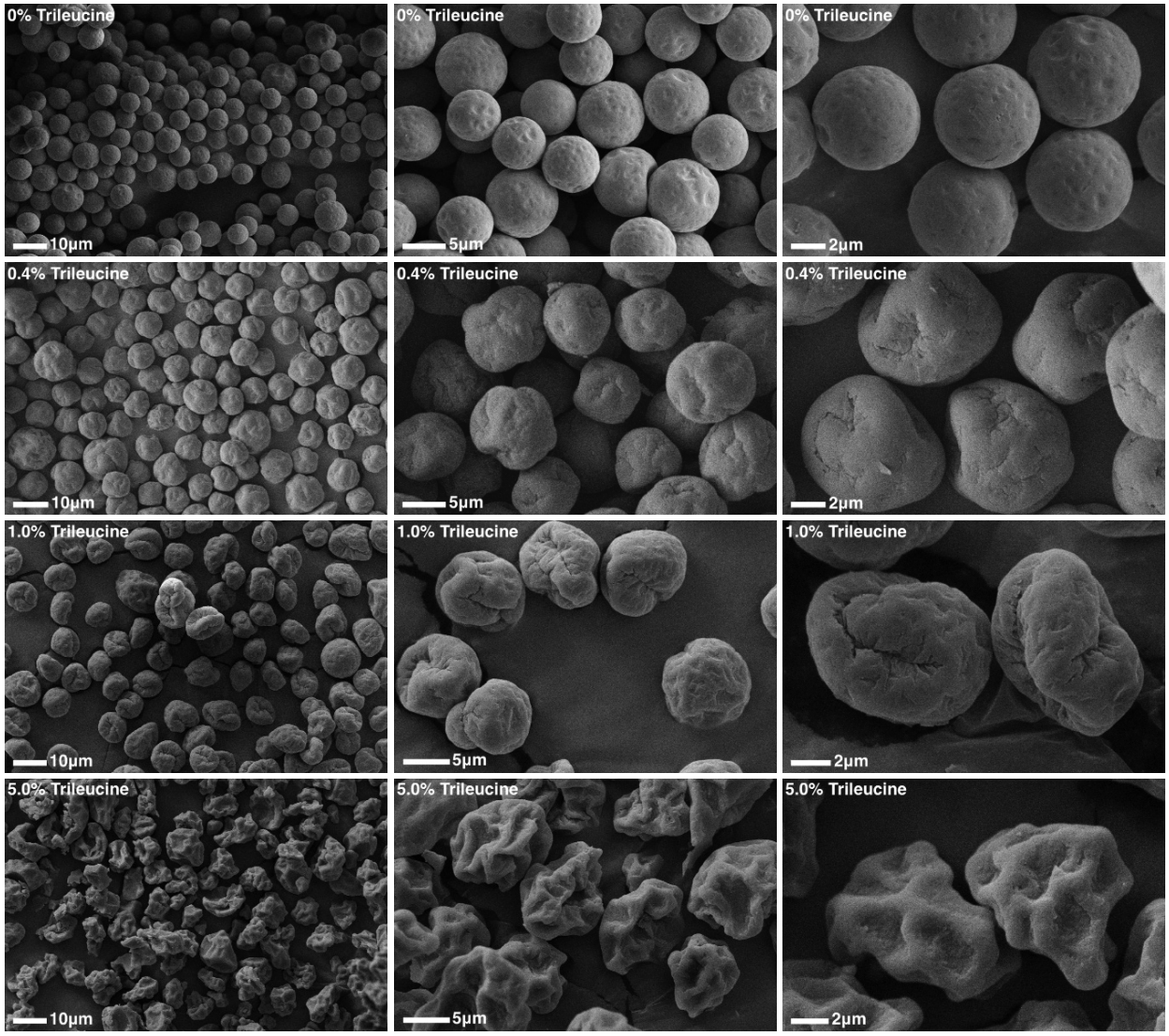

Figure 4.2. Morphology of the monodisperse spray-dried particles gradually changed from smooth to highly rugose when the concentration of trileucine was increased from 0% to 5.0%.

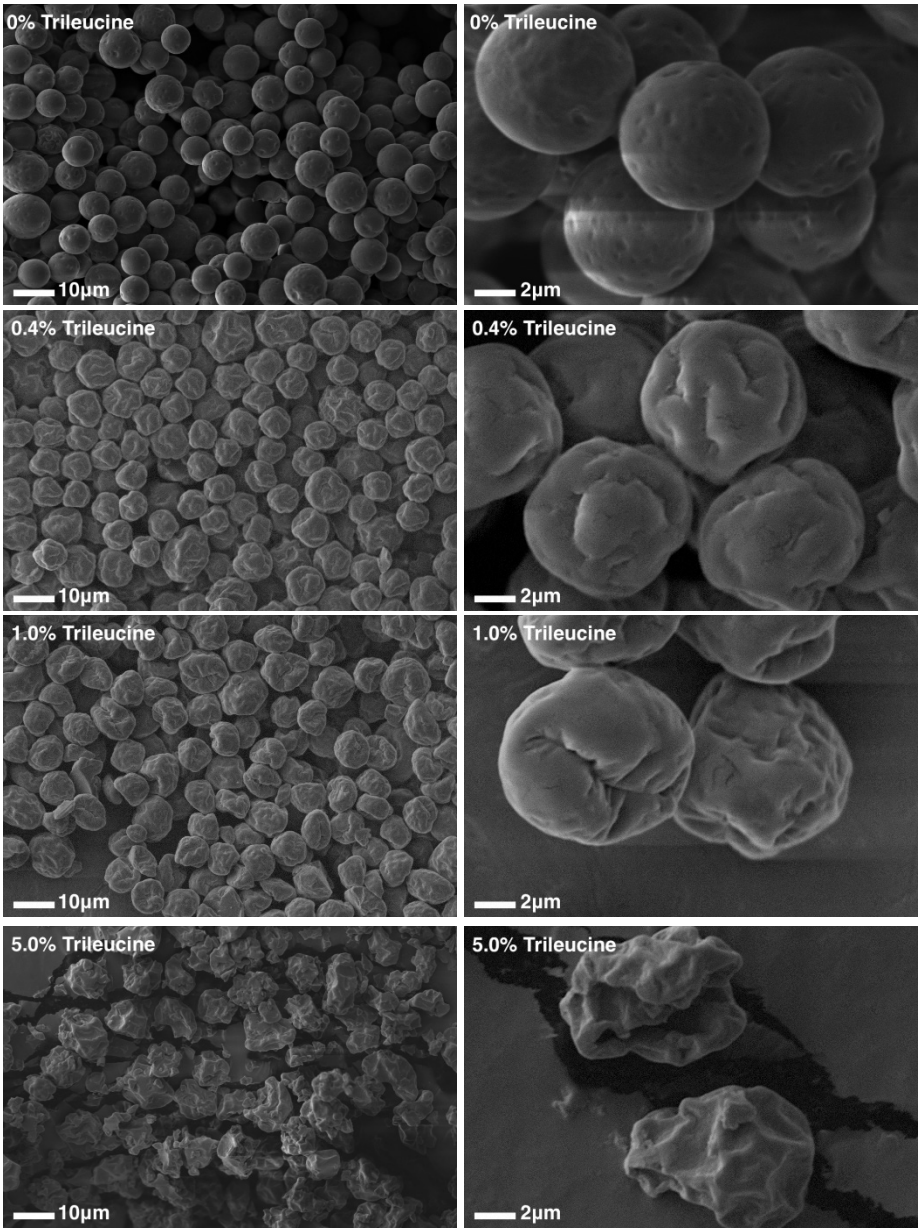

Figure 4.3. Images of particles extracted from the propellant after ultrasonic agitation showing no significant changes of morphology.

To prove that the surface structure of the particles was maintained in the propellant, the morphology of particles after suspension stability measurement is presented in **Figure 4.3**. In comparison with their original morphology shown in **Figure 4.2**, no significant morphology changes were found and the surface structures of the designed particles were retained, proving that

no dissolution or disruption of the particles occurred during the timeframe of the stability measurement. This is essential to the explanation that the increased surface roughness is directly transferred to the weaker inter-particle cohesive forces and eventually lead to improved colloidal stability rather than any changes of surface tension or surface energy of the suspensions caused by particle dissolution being responsible for the improved suspension stability.

The results of solid phase analysis by Raman spectroscopy are shown in **Figure 4.4**. Reference Raman spectra of amorphous (a-Tre) and crystalline (c-Tre) trehalose show different features in the displayed spectral region (70 – 1600 cm^{-1}, 2800 – 3200 cm^{-1}). For the first time, to our knowledge, the Raman spectra of amorphous (a-Leu_3) and crystalline (c-Leu_3) trileucine are also presented and compared. In general, crystalline materials have sharper and better-defined peaks because of the more isolated vibrational energy levels of their molecular bonds, while the Raman peaks are broadened due to the higher degree of disorder in amorphous materials (Hédoux, 2016; Wang et al., 2014). In comparison with the reference spectra of both amorphous and crystalline trehalose, a 100% amorphous state was confirmed for the three batches of spray-dried pure trehalose presented in **Figure 4.1**. Due to the low concentration of trileucine in the spray-dried trehalose-trileucine particles, a subtraction process was used for the solid-state identification. As a demonstration, the bottom trace in **Figure 4.4** is a residual spectrum after subtracting amorphous trehalose from the spectrum of the spray-dried sample with 95% trehalose and 5% trileucine. The residual spectrum is similar in shape to the reference spectrum of amorphous trileucine, and no trace of crystalline trehalose or trileucine can be found, proving the completely amorphous state of trehalose and trileucine in the dried particles. The solid state of trehalose and trileucine in the other cases was similarly determined to be 100% amorphous.

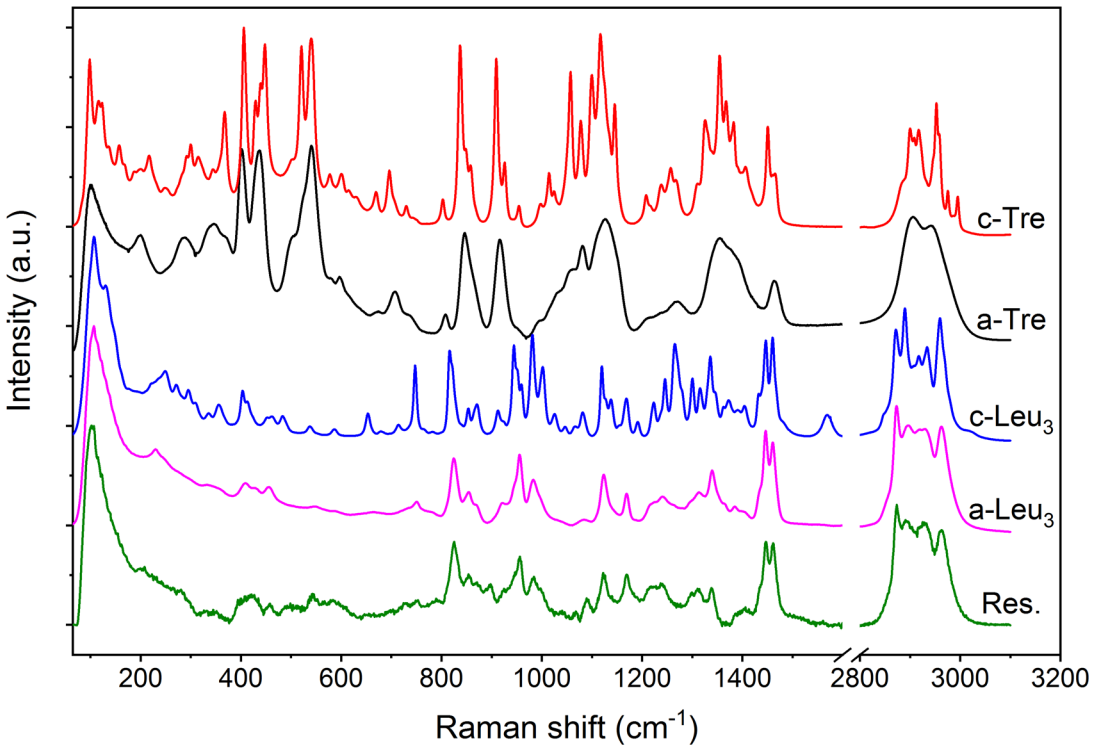

Figure 4.4. Reference spectra of crystalline trehalose (c-Tre), amorphous trehalose (a-Tre), crystalline trileucine (c-Leu$_3$), and amorphous trileucine (a-Leu$_3$). The bottom trace is a residual spectrum (Res.) arrived at by subtracting amorphous trehalose from the spectrum of trileucine-modified trehalose particles (95.0%Tre-5.0%Tri), proving the amorphous state for both trehalose and trileucine.

4.3.2. Size distributions of spray-dried particles

Three typical mass-based aerodynamic particle size distributions measured by the in-line aerodynamic particle sizer for the feed solutions with different initial concentrations are presented in **Figure 4.5**. These were in good agreement with the monomorphic particles observed from the SEM morphological analysis, all having narrow geometric standard deviations (GSD < 1.2), meaning that the dried trehalose particles were uniform and monodisperse. It is known that aerodynamic diameter, d_a, of spray-dried particles is related to the feed solution concentration, c_0, such that

$$d_a = \sqrt[6]{\frac{\rho_P}{\rho_0}} \cdot \sqrt[3]{\frac{c_0}{\rho_0}} \cdot d_0 \tag{4.13}$$

in which ρ_P, ρ_0, and d_0 are the particle density, unit density, and initial droplet diameter respectively. As designed, the three different batches of spray-dried trehalose showed very distinct mass median aerodynamic diameters (*MMAD*), and the final particle size increased with the trehalose solution concentration.

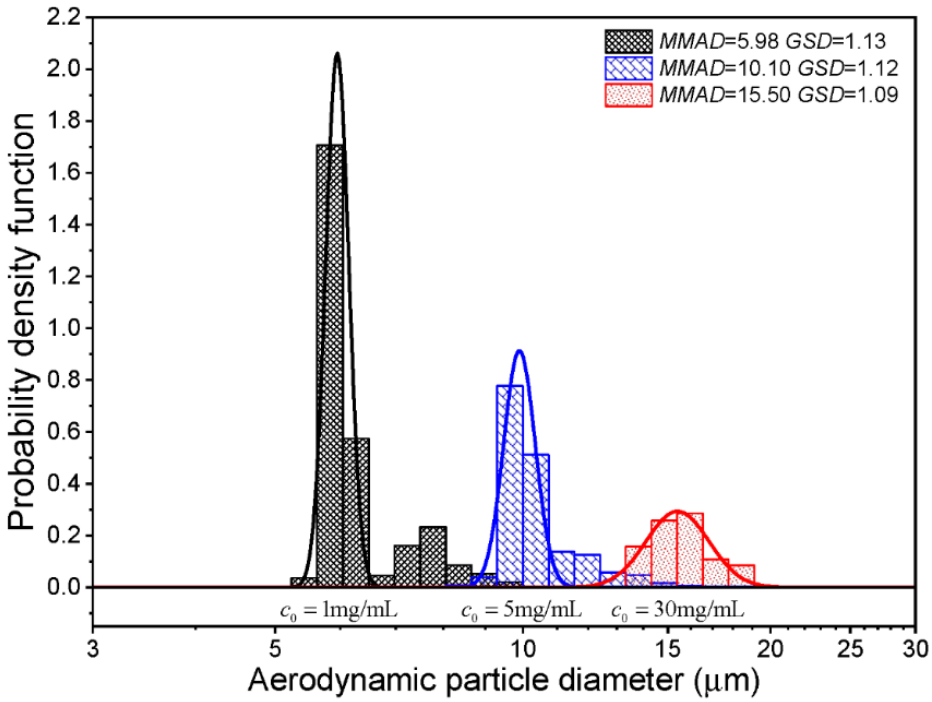

Figure 4.5. Aerodynamic size distributions of the spray-dried trehalose particles show high monodispersity with narrow distributions (*GSD* < 1.2). The corresponding *MMAD* increased from 6.0 μm to 15.5 μm with increasing feed solution concentrations.

Figure 4.6 shows the cumulative distributions of the measured trehalose volume equivalent diameters and fittings of the data with a least square regression method. All three cases also had good monodispersity with *GSD* < 1.2, which is in a good agreement with the results of direct aerodynamic size measurement. According to the central limit theorem, the obtained volume

equivalent diameters after measuring more than 300 particles for each sample were within small intervals (± 0.11, ± 0.15, ± 0.16) around the population median diameters with a high confidence level (99%), making this method of assessing the particle size distributions feasible. The count-based median volume equivalent diameters were compared to the APS-measured *MMAD* by first converting the volume equivalent diameter, d_{ve}, to aerodynamic diameter, d_a, according to **Eqn.(1.1)** assuming that the particle density was the same as the trehalose true density. The calculated aerodynamic diameter was thus equivalent to the count median aerodynamic diameter, *CMAD*. The *CMAD* was then used to calculate the *MMAD* using the Hatch-Choate **Eqn.(4.14)** (Hinds, 2012), which is practical only for monodisperse or near-monodisperse particles. Otherwise, a large bias error will be inevitable with this method for particles with a large *GSD* unless a very large number of particles are measured. Uncertainties (± δ) of the calculated *CMAD* and *MMAD* were estimated by assuming that the particle density is within ± 5% of its true density and the measured geometric standard deviation has a 10% uncertainty.

$$MMAD = CMAD \cdot \exp(3\ln^2 \sigma_g) \tag{4.14}$$

The comparison in **Table 4.3** shows that the calculated *MMAD* based on the volume equivalent diameter was close to the *MMAD* measured directly by the APS, indicating that the spray-dried particles were indeed monodisperse and their particle size distributions were correctly measured separately. These findings also mean that there was little or no void space, as expected. Using the particle size measured for the dried particles and a simple relation of solute mass conservation, the initial droplet diameters were also calculated to be within the predicted droplet size range of 50 μm – 65 μm. The asymmetrical and bimodal shape of the distributions indicating the existence of exceptional sized particles is observed in both **Figure 4.5** and **Figure 4.6**, and is a known phenomenon likely caused by doublets, triplets, etc., due to droplet coalescence in the

spray. However, these larger particles caused by the droplet coalescence are negligible in their count-based size distributions and are expected to settle much faster than the particles with primary sizes, hence their effects on the suspension stability measurements are expected to be minor.

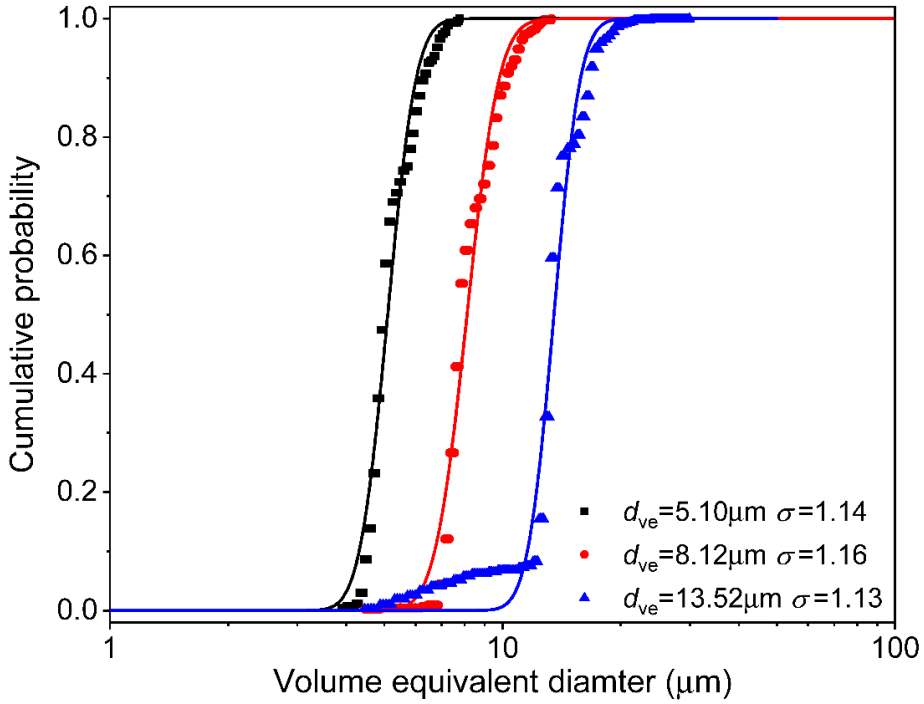

Figure 4.6. Cumulative volume equivalent diameter distributions of the spray-dried trehalose particles measured directly from the SEM images. The results agree well with the aerodynamic diameter distributions measured by the aerodynamic particle sizer.

Table 4.3. Comparison of particle size distributions measured using different methods.

d_{ve} (μm)	σ_g	d_{ve} confidence interval (99%)	d_a (*CMAD*) ± δ (μm)	*MMAD*-Calc. ± δ (μm)	*MMAD*-APS (μm)	d_0 (μm)
5.10	1.14	0.11	6.31 ± 0.21	6.65 ± 0.57	5.98	58.8
8.12	1.16	0.15	10.04 ± 0.33	10.74 ± 1.01	10.10	54.7
13.52	1.13	0.16	16.72 ± 0.48	17.49 ± 1.37	15.50	50.2

Aerodynamic particle size distributions for the spray-dried formulations with different trehalose-trileucine ratios are presented in **Figure 4.7**. All batches show good monodispersity with narrow geometric standard deviations (*GSD* < 1.2). The four batches of particles with the same solids concentration show similar mass median aerodynamic diameters. A slight shift of the *MMAD* towards the lower end from 10.1 µm to 8.7 µm is also observed. This is because particles with a higher level of rugosity lead to lower particle density, and therefore smaller aerodynamic diameters, according to **Eqn.(4.13)**. Overall, particles with different surface rugosity and similar size were successfully produced as designed.

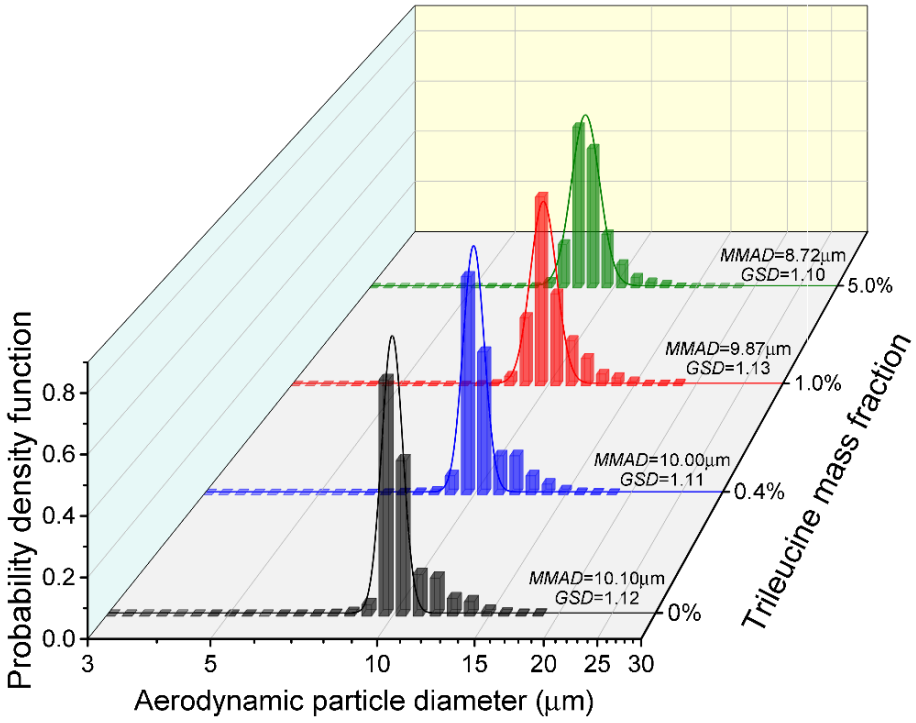

Figure 4.7. Particle size distributions of the spray-dried trehalose-trileucine particles show high monodispersity for formulations with different trileucine mass fractions. The mass median aerodynamic diameters decreased slightly due to the increased particle rugosity caused by the increase in trileucine mass fraction from 0% to 5.0%.

4.3.3. Specific surface area analysis

In addition to the qualitative particle roughness information provided by the SEM images, specific surface areas of the monodisperse spray-dried powders were measured to provide quantitative confirmation. The linearized BET isotherm plot described by **Eqn.(4.6)** is presented in **Figure 4.8**. Listed in **Table 4.4** include the slope (s), intercept (i), BET constant (C), and specific surface area (A_r) derived based on the krypton adsorption isotherm plot.

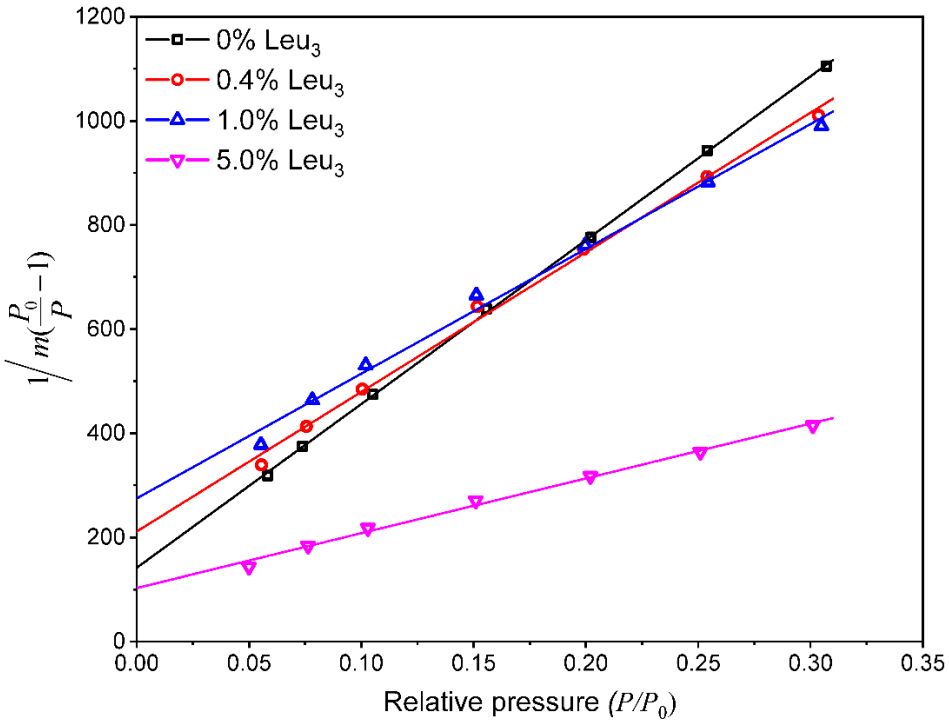

Figure 4.8. Linear region of the krypton adsorption isotherm used for the determination of specific surface area and BET constant.

Table 4.4. Data used for the determination of particle specific surface area and BET constant.

Sample	Slope, S	Intercept, i	R^2	Weight of monolayer, m_0 (mg)	BET constant, C	Specific surface area, A_r (m^2/g)
0% Tri	3148±20	141±4	> 0.999	0.30±0.01	23.3±0.6	0.45±0.02
0.4% Tri	2682±73	211±14	0.996	0.35±0.01	13.7±0.9	0.51±0.01
1.0% Tri	2397±89	275±16	0.992	0.37±0.01	9.7±0.6	0.55±0.01
5.0% Tri	1053±35	103±6	0.993	0.87±0.02	11.2±0.7	1.28±0.02

Shown in **Figure 4.9** is a comparison of the calculated surface rugosities for the spray-dried formulations with different trileucine concentrations. The real specific surface area (A_r) was directly measured from the BET method, and the geometric specific surface area (A_g) for each sample was calculated based on the particle size presented in **Figure 4.7** and assuming perfectly spherical and smooth particles for all the four cases. Uncertainties of the measured specific surface area were mainly originated from the gravimetric measurement of the used powder for characterization. The surface rugosity for the pure trehalose sample is slightly higher than 1.0, which is expected and is likely to be caused by the particles not being perfectly monodisperse and smooth spheres. On the other hand, the rugosity being close to the theoretical value of 1.0 in turn proves a good monodispersity of the dried particles.

The specific surface area slightly increased from 0.45 ± 0.02 m^2/g for the pure trehalose particles to 0.51 ± 0.01 m^2/g and 0.55 ± 0.01 m^2/g for the cases with 0.4% and 1.0% trileucine respectively, and further significantly increased to 1.28 ± 0.04 m^2/g with higher trileucine concentration at 5.0%, which corresponds to a surface rugosity that is almost three times higher than the pure trehalose particles, proving that highly-rugose particles were produced. These results also agree with our prediction by the particle formation theory as well as SEM images that the

particles gained higher level of rugosity slowly when a small fraction of trileucine was added just enough to form a thin film, while the increase of surface roughness became more significant when the shells formed much earlier in the particle drying process upon the addition of more trileucine, the shell former.

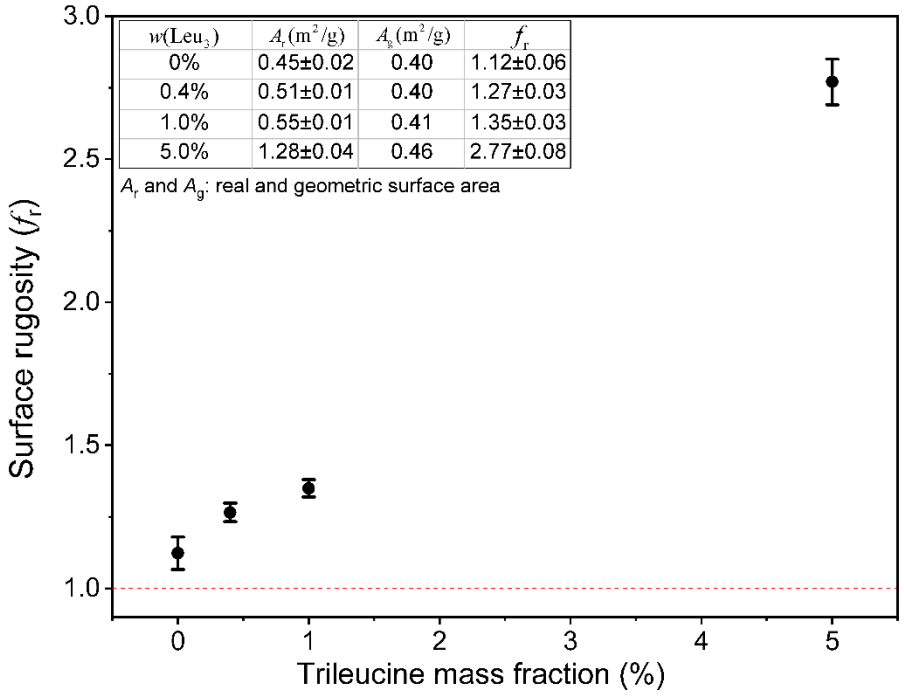

Figure 4.9. Surface rugosity ($f_r = A_r / A_g$) of the monodisperse spray-dried particles increased gradually as more trileucine was added to the feed solution. Insert table shows the real and geometric specific surface area used for the calculation of rugosity. Dotted base-line corresponds to a rugosity of 1.0 for perfectly smooth and spherical particles.

Along with the specific surface area, the BET constant that is directly related to adsorbent-adsorbate interaction energy for the first layer was also determined. Therefore, in the current study, the BET constants are indicators of the surface compositions of the formed particles. The BET constants for the samples with 0.4%, 1.0% and 5.0% trileucine were determined to be close at 13.7 ± 0.6, 9.7 ± 0.6, and 11.2 ± 0.7 respectively, indicating similar surface compositions. However, the BET constant for the pure trehalose sample was determined to be different from the

other three samples at 23.3 ± 0.6. This is an indication that trileucine indeed accumulated on the particle surfaces as designed.

4.3.4. Effects of particle size on the suspension stability

To study the effects of particle diameter, the stabilities of suspensions with monodisperse trehalose particles of different sizes but the same concentration at 0.23% (w/w) were first measured and compared. Three suspensions were prepared for each batch of spray-dried particles and each suspension sample was measured three times for 30 min immediately after ultrasonic agitation. As their normalized relative transmission profiles shown in **Figure 4.10**, the time-dependent transmission intensity changes over the entire height of the suspensions. Along the height axis, the profiles start at the bottom of the vial, at a normalized height of 0, and end at the top of the suspension, at a normalized height of 1. Intensity of the transmission change is also a normalized value in the range of 0 to 1. The suspensions with small, medium, and large trehalose particles destabilized very differently during the 30min observation time. In all cases, a thin layer of settled particles was detected at the bottom of the vial, indicated by the reduced transmission intensities close to the normalized height of 0. Different levels of clarification were observed for the three different suspensions, and the level of clarification after 30 min increased substantially from less than 10% for small particles (d_a = 6.0 μm) to about 60% for large particles (d_a = 15.5 μm). The clarification processes occurred uniformly across the whole suspension for all the cases indicated by the simultaneously increasing transmission intensities over the whole suspension sample.

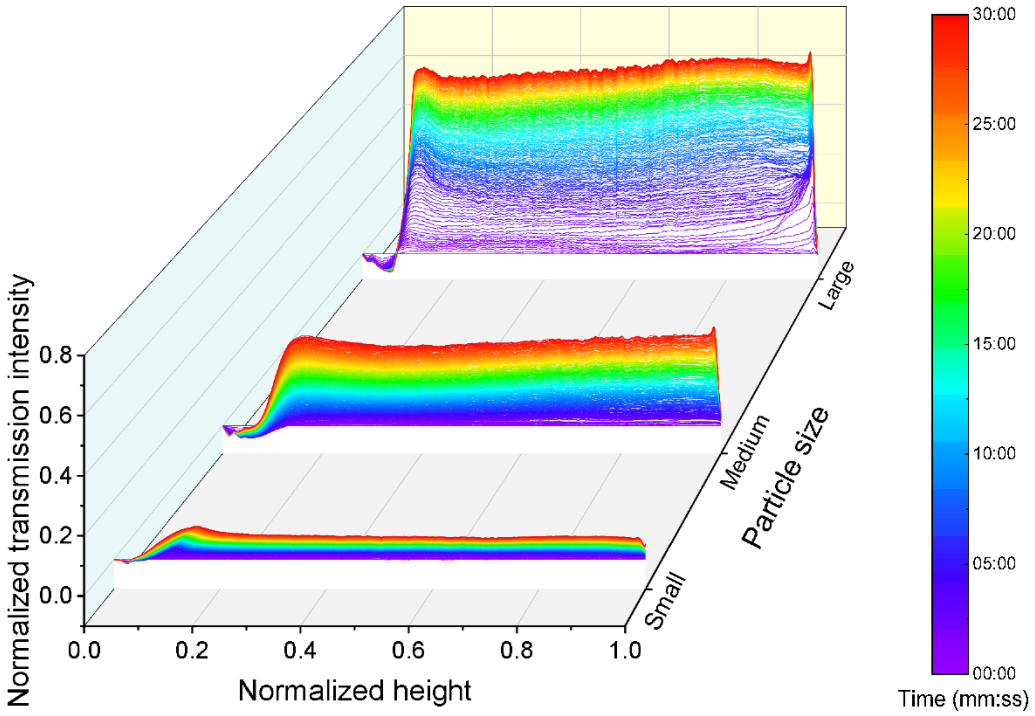

Figure 4.10. Normalized relative transmission profiles of the pressurized suspensions indicate that suspension stability strongly depends on the diameter of suspended particles. The suspension with large particles destabilized much more and much faster than those with smaller particles.

Plotted in **Figure 4.11** are the corresponding instability indices described in **Eqn.(2.4)** for the suspensions with monodisperse trehalose particles of different sizes. Each data point corresponds to a shadowgraphic image acquired at a specific time point, and the high temporal resolution (0.5 Hz) of the suspension tester enables monitoring and comparison of the suspension stability at any time point of the destabilization process. There is a clear trend of decreasing suspension stability when the suspended particles become larger. In combination with the transmission profiles shown in **Figure 4.10**, the lower level of clarification for the suspension with small particles corresponds to the lower instability index plot in **Figure 4.11**, and vice versa. Based on the slopes of the plots, the destabilization process for the sample with large particles started

rapidly from the beginning of the measurement, while the other two samples experienced slower transitions. After 30 minutes of observation, the rate of destabilization for large particles started to slow down and the instability index approached 0.7. However, the destabilization processes for the other two samples were still ongoing at the end of the observation period and showed little sign of slowing.

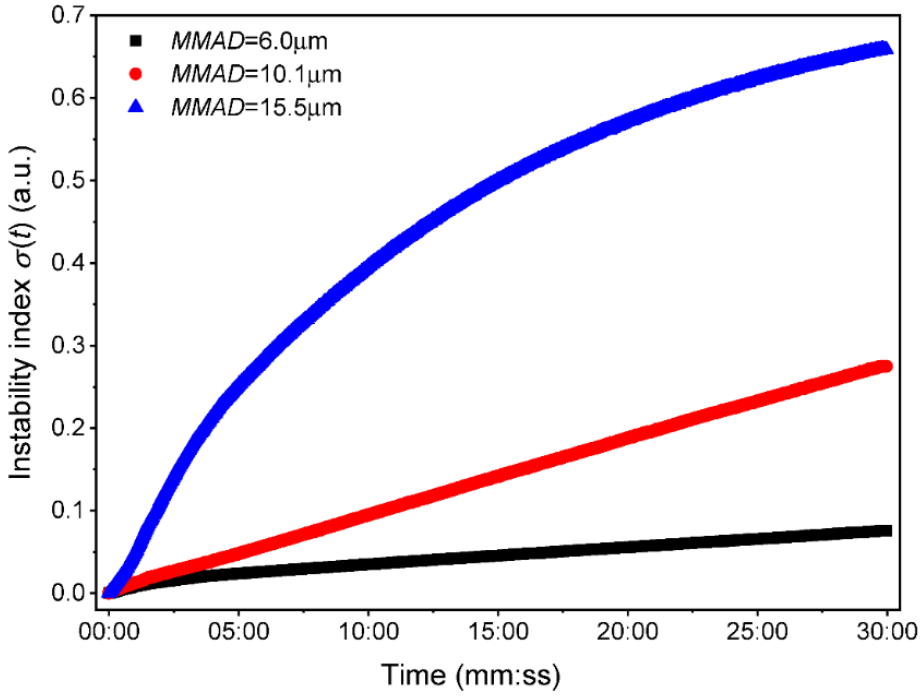

Figure 4.11. Instability index plots for suspensions of different trehalose particles show that larger particles lead to faster destabilization of the corresponding suspension.

To quantitatively illustrate the dependence of suspension stability on particle diameter, final instability indices at the end of the 30 min stability measurement, $\sigma(t = 30\,\text{min})$, are presented in **Figure 4.12**. The extra point at (0, 0) represents a virtual suspension sample with infinitely small particles, which will therefore be extremely stable and show no transmission changes at all; hence, the constant instability index at 0. The error bar for each data point stands for the variation between the three repeated measurements for each suspension sample. All are relatively small, proving

reproducible stability measurements. A certain level of cross-sample variation can be also observed between the suspensions containing particles of the same size, shown as the three data points for each particle diameter. Nevertheless, the instability index strongly depends on the diameter of suspended particles and demonstrated that the larger the particles the less stable the suspensions become.

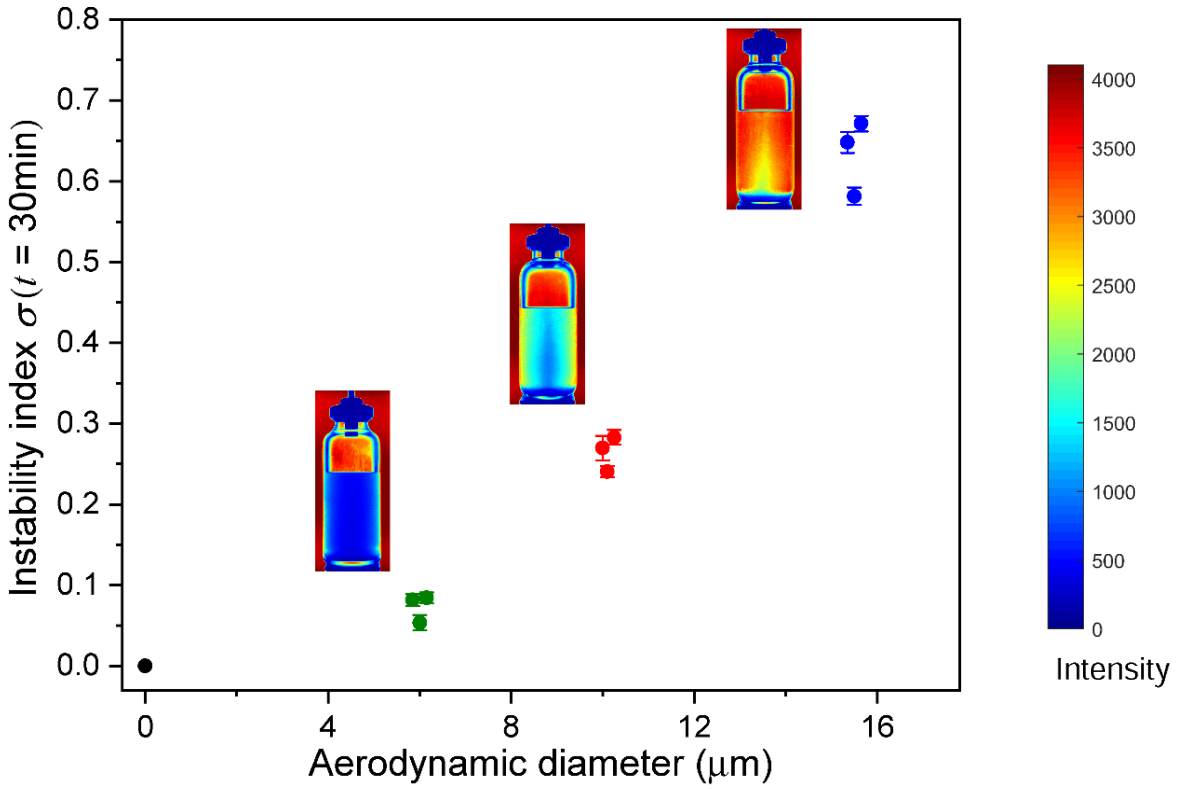

Figure 4.12. Comparison of the final instability indices at 30 min, σ (t = 30 min), for different suspensions shows a strong dependence of suspension stability on particle diameter. Three independent suspension samples were prepared for each group of particles, and each suspension was measured three times for its suspension stability. Inset shadowgraphic images represent end state of the suspension after 30 minutes measurement.

The suspensions with particles smaller than 5 μm remain relatively stable for at least 30min. However, increasing particle sizes beyond 5 μm will greatly impact the stability of the corresponding suspensions, and this can be explained by much faster settling velocities for the

larger particles according to **Eqn.(1.1)**, in which settling velocity is proportional to d_a^2. However, the question remains whether or not aggregation plays a role, which will be discussed in the next section.

4.3.5. Improved suspension stability with surface modification

The stability of the suspensions with particles exhibiting different levels of rugosity was also measured, and their normalized relative transmission profiles are presented in **Figure 4.13**. Similar to the suspensions of pure trehalose, a layer of settled particles was observed in all cases, as indicated by the reduced transmission intensity at the bottom, and the top portions of the suspensions all clarified to a certain extent after 30 minutes. The formulations with 0.4% trileucine destabilized similarly ($p > 0.1$) to the suspension with pure trehalose, and the difference started to become significant ($p < 0.01$) when the fraction of trileucine was increased to 1.0%. The formulation with 5.0% trileucine is the most distinctive case, showing little change over the 30 min measurements and thus manifesting a significantly improved ($p < 0.002$) suspension stability.

According to **Eqn.(1.1)**, particles with similar true densities and aerodynamic diameters should have close settling velocities and produce suspensions with similar colloidal stabilities. However, some of the suspensions tested here showed significantly different stabilities, proving that particle aggregation is making the difference in the destabilization process of the different suspensions. Considering that all the suspensions have the same concentration and the particles have a similar frequency of collision, it must be the changes in cohesive forces, either through surface energy or surface roughness, that is causing the different level of aggregation. Based on our earlier discussion of the theory of particle formation and also the work of Lechuga et al. (Lechuga-Ballesteros et al., 2008), trileucine is likely to be on the surface of the particles in all the formulations with 0.4%, 1.0%, and 5.0% trileucine. However, only an insignificant stability

improvement ($p > 0.1$) was observed for the suspensions with 0.4% trileucine when compared to the suspension of pure trehalose, indicating that surface composition of the particles is not the main factor here. This, leaves surface roughness as the only factor significantly affecting the suspension stability. It has been shown that surface roughness of microparticles is indeed the most important factor in determining the inter-particle cohesive forces (Baldelli and Vehring, 2016; Cheng et al., 2002), and the change in suspension stability become significant when short-range roughness increases, as in the cases with 1.0% and 5.0% trileucine.

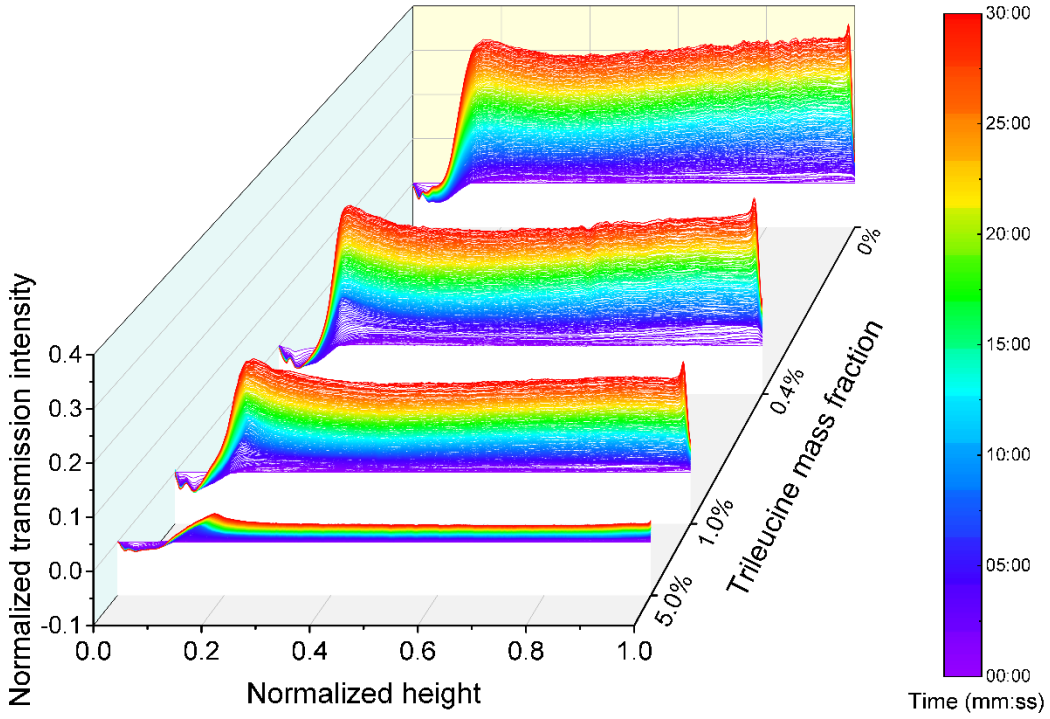

Figure 4.13. Normalized relative transmission profiles indicate a slower destabilization process as more trileucine is added to the formulation and the suspended particles become more wrinkled.

In accordance with the transmission profiles, typical instability index plots for the different formulations in **Figure 4.14** also show different rates of destabilization as indicated by their different slopes. By comparison, the suspension with pure trehalose particles exhibiting relatively spherical and smooth surfaces destabilized the fastest. The instability index goes beyond 0.25 after 30 minutes of observation. As more trileucine was added to the formulation and the dried particles became more rugose, the suspension stability improved gradually. The 5.0% trileucine – 95.0% trehalose case that showed the best suspension stability corresponded to the most highly corrugated particles and remained stable for the entire 30 minutes. The final instability index at 30 min stayed below 0.03, which is much lower than the other cases.

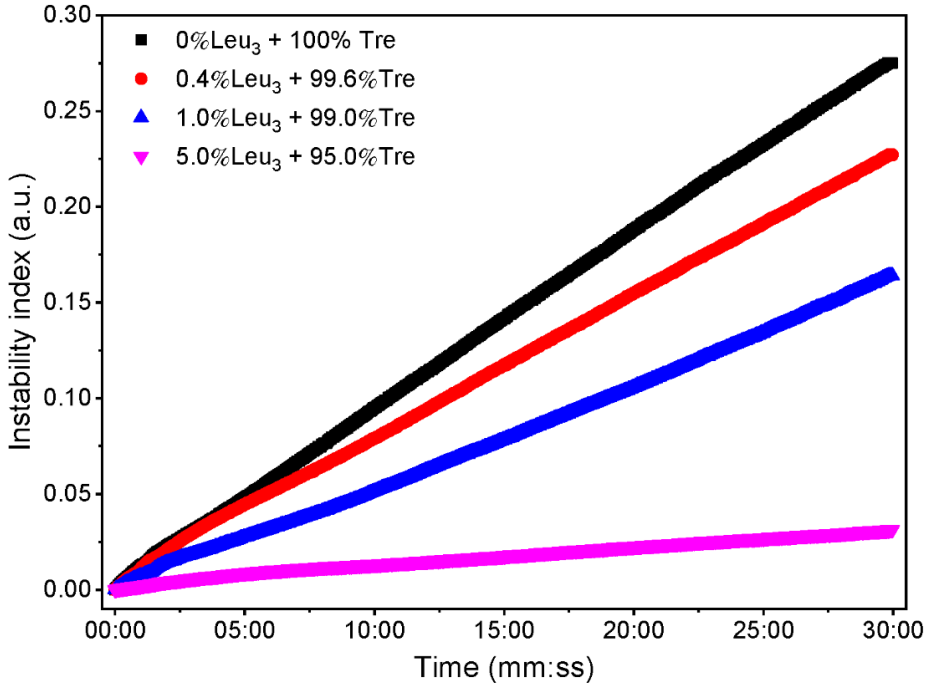

Figure 4.14. Instability index plot for suspensions of particles with different rugosity show that the increased surface roughness by trileucine improves suspension stability and reduces the rate of the destabilization process.

A quantitative stability comparison between the suspensions is shown in **Figure 4.15** with the corresponding final instability indices at 30 min, $\sigma(t = 30\,\text{min})$, plotted against trileucine mass fraction. The change in surface roughness caused by a small amount of trileucine in 0.4% already makes a difference in the stability of the corresponding suspensions. When the trileucine concentration was increased to 1.0% and 5.0%, the suspension stability was significantly improved by the increased surface rugosity and the instability index dropped substantially from 0.27 ± 0.02 to 0.18 ± 0.01 ($p < 0.01$) and 0.03 ± 0.01 ($p < 0.002$) respectively. This result further proves that aggregation plays a major role in the settling of pure trehalose particles and is not just a factor of density difference and particle size. It is likely that the particles aggregate and settle with a larger volume equivalent diameter of the aggregate.

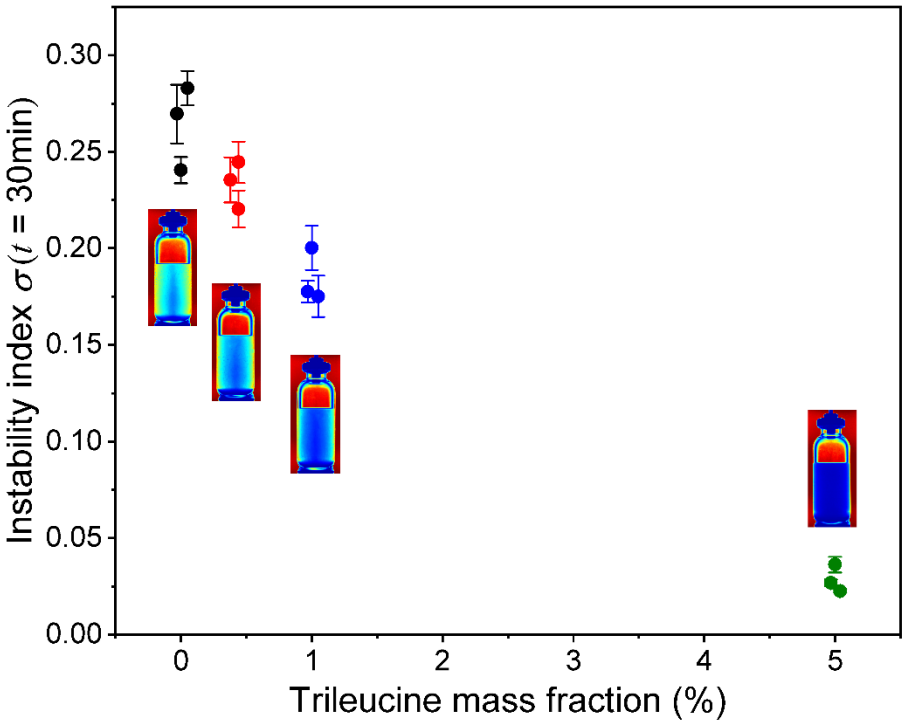

Figure 4.15. Instability indices σ ($t = 30$ min) for suspensions with particles of different rugosity. The suspension stability improves as the particles become more wrinkled. Inset shadowgraphic images represent end state of the suspension after 30 minutes measurement.

Taking into consideration the change of instability index that could be caused by their slightly different particle sizes as detected and shown in **Figure 4.7**, the instability indices for the relatively smaller particles with 0.4% and 1.0% trileucine were expected to be slightly lower—in the range of 0.27 ± 0.02—assuming that the dependence of suspension stability on particle size plotted in **Figure 4.12** is applicable in this case. However, the decrease in the instability index from the suspension with pure trehalose particles to the suspension with 0.4% and 1.0% trileucine is much more substantial than what might be caused by particle size difference. It is more obvious that the case with 5.0% trileucine, whose final instability index at 30 minutes was 0.03 ± 0.01, is even more stable than the suspension case with much smaller pure trehalose particles (*MMAD* = 5.98 μm), whose 30 min-instability index was 0.07 ± 0.01, as shown in **Figure 4.12**. In comparison with the specific surface area measurement presented in **Figure 4.9**, the trend of improved suspension stability agrees well with the trend of increased rugosity, which is directly related to particle surface roughness, demonstrating that the increased surface roughness is indeed playing an important role in stabilizing the suspensions.

The significant improvement to suspension stability caused by increased particle surface rugosity can be explained by the weaker van der Waals forces of rough-surfaced particles than of particles with smooth surfaces both in air (Adi et al., 2008; Baldelli and Vehring, 2016) and propellant (D'Sa et al., 2014) as outlined earlier. When the particles become more corrugated, the increased surface roughness leads to a substantially reduced contact area between particles as they collide during movement in the suspension. Consequently, the macroscopic inter-particle cohesion forces are also reduced. The reduced cohesion forces in turn lead to lower chances of particle aggregation upon collision. Because of the increased surface roughness, the particles settle individually at a much slower speed with less chance of particle aggregation, and the suspension

stability is much improved as a result. There may also be a tendency for the flocs to break up again if they are held together by weak forces, which may limit the maximum floc size.

4.4. Conclusions

The batch production of monodisperse particles using a custom-designed micro-jet atomizer offers a great opportunity to study the effects of each individual factor on suspension stability without the complications caused by polydisperse particles. For the first time, the effects of particle surface roughness on the stability of pressurized pharmaceutical suspensions are isolated and investigated in this study using monodisperse spray-dried trehalose-trileucine composite particles. The stability trend of the model suspensions of monodisperse trehalose particles with different median diameters demonstrates that the suspension stability can be significantly improved by reducing the sizes of suspended particles, which is expected based on the slower settling velocity of smaller particles. However, flocculation of particles is a key factor in suspension stability. Therefore, factors affecting flocculation, such as suspension concentration and particle cohesiveness in the propellant, need to be monitored carefully. Trileucine with low solubility and surface activity is an effective shell former, such that a small amount of trileucine (≤ 5.0% w/w) can change the trehalose particle morphology substantially, and the final particle surface rugosity can be significantly improved by spray drying feed solutions with higher trileucine-trehalose ratios. More importantly, the suspension stability of the particles whose surface has been modified by trileucine shows a clear dependence on the surface rugosity of the suspended particles: more corrugated particles lead to more stable suspensions, and all of them are more stable than suspensions containing pure trehalose particles with relatively smooth surfaces. Therefore, in respiratory drug delivery scenarios where the drug particle diameters are restricted within a certain range (1 – 5 μm) for the best delivery efficiency, increasing the surface roughness of the particles,

for example, by using shell formers like trileucine, is potentially a promising technique that can be used to stabilize their suspensions. This approach is likely not very dependent on the type of propellant and does not require the use of a surfactant. By avoiding solubility issues with surfactants in the novel propellants, this approach could prove highly useful in the transition to more environmentally friendly pMDIs.

CHAPTER 5 Conclusions

The importance of colloidal stability for pharmaceutical suspensions, especially pressurized suspensions used in pulmonary drug delivery, is highlighted and discussed in this thesis. A novel shadowgraphic imaging technique developed for the colloidal stability characterization of pharmaceutical suspensions is introduced together with its applications in the development of stable pMDI formulations. Main findings of this thesis are presented here with some thoughts on future study.

5.1. Main Conclusions

A new shadowgraphic imaging method and an associated instrument are introduced to fill the need for an effective technique for characterizing the colloidal stability of pressurized pharmaceutical suspensions. Pressurized suspensions with a wide range of colloidal stability can now be measured with both a wide range of temporal resolution (0.001 – 100 Hz) and a high spatial resolution (2560 × 2048 pixel). The developed normalized relative transmission profiles can be used as a unique fingerprint for each sample to qualitatively describe the destabilization processes. The instability index provides a single parameter based on the transmission changes, which is useful in quantitatively comparing and rank-ordering the stabilities of multiple samples.

For the purposed of making meaningful stability measurements, the effects of agitation on the colloidal stability of suspensions, an important aspect of suspension stability measurement that has rarely been discussed, are studied. The suspension stability shows a strong dependence on the applied agitation method inasmuch as the same suspension can behave differently when agitated using different methods. Therefore, cross-sample stability comparison must be based on the same

agitation method, and suspension stability analysis results must be accompanied with a detailed description of the applied agitation method for any measurement of suspension stability to be fully meaningful. Ultrasonic agitation is also proved to be the most effective method in dispersing the aggregated particles to their primary sizes and thus serves as a benchmark for all stability measurements.

The shadowgraphic imaging technique was further used in the development of stable pharmaceutical formulations, which is the end goal of this thesis. Surface roughness introduced to spray-dried model particles by a shell former was proved to be promising in reducing inter-particle cohesive forces and improving the resultant suspension stability. This approach provides a new perspective in the development of stable suspension formulations, especially in respiratory drug delivery scenarios where the optimum respirable widow for the drug particle diameter is narrow, within 1 – 5 μm. More importantly, this approach is likely not very dependent on the type of propellant and does not require the use of any surfactants, which could prove highly useful in the transition to the more environmentally friendly pMDIs by avoiding the solubility issues of the surfactants in the novel propellants.

5.2. Future Work

From the perspective of instrument design, there are still some improvements that can be made. For example, as discussed inCHAPTER 2 CHAPTER 3, the built-in ultrasonic agitation device is known to cause multiple reflections and refractions of the transmitted light, which can be minimized by using glass vessels and ultrasonic liquid with a similar refractive index as the propellant. Adding a temperature control unit for the ultrasonic bath can provide more capabilities to the technique to study temperature-dependent suspension stabilities. Despite the capability of

controlling the output power from the amplifier to the transducer, the actual energy coupled to the suspension remains unknown. Therefore, for controlled and quantified agitation, it will be a significant improvement if the actual energy delivered to the suspensions can be measured either directly or indirectly.

As briefly mentioned in CHAPTER 3, other than the agitation method, only the density and viscosity of the propellant were considered to affect the particle settling velocity and hence suspension stability. No evidence proving the effects of surface interaction was found because the tested model saccharide particles have very similar surface properties and morphology. The surface properties of the propellants, such as surface tension, can be important in determining the suspension stability as well as the corresponding aerosolization performance. A further study on this topic can contribute to the ongoing transition to novel pMDIs with more environment-friendly propellants.

Only the first-order factors affecting suspension stability, including particle size and surface roughness, were addressed in CHAPTER 4, but many of the other factors, such as API type, long-term storage, propellant type, excipient, and surfactant, are worthy of some attention and deserve to be studied further in the future. For example, for the proposed approach to be applied in pharmaceutical products, long-term storage stability of the shell-former must be tested for each propellant. It will also be useful to expand the candidates for shell formers that can be used to introduce controlled surface rugosity to the particles.

BIBLIOGRAPHY

Adi, S., Adi, H., Tang, P., Traini, D., Chan, H.-k., Young, P.M., 2008. Micro-particle corrugation, adhesion and inhalation aerosol efficiency. *European Journal of Pharmaceutical Sciences, 35*(1-2), 12-18. DOI: http://dx.doi.org/10.1016/j.ejps.2008.05.009

Arora, P., Kumar, L., Vohra, V., Sarin, R., Jaiswal, A., Puri, M., Rathee, D., Chakraborty, P., 2014. Evaluating the technique of using inhalation device in COPD and bronchial asthma patients. *Respiratory Medicine, 108*(7), 992-998. DOI: http://dx.doi.org/10.1016/j.rmed.2014.04.021

Ashayer, R., Luckham, P.F., Manimaaran, S., Rogueda, P., 2004. Investigation of the molecular interactions in a pMDI formulation by atomic force microscopy. *European Journal of Pharmaceutical Sciences, 21*(4), 533-543. DOI: http://dx.doi.org/10.1016/j.ejps.2003.12.003

Azhdarzadeh, M., Shemirani, F.M., Ruzycki, C.A., Baldelli, A., Ivey, J., Barona, D., Church, T., Lewis, D., Olfert, J.S., Finlay, W.H., Vehring, R., 2016. An atomizer to generate monodisperse droplets from high vapor pressure liquids. *Atomization and Sprays, 26*(2), 121-134. DOI: http://dx.doi.org/10.1615/AtomizSpr.2015011631

Babick, F., 2016. *Suspensions of colloidal particles and aggregates* (Vol. 20): Springer. DOI: http://dx.doi.org/10.1007/978-3-319-30663-6_4

Baldelli, A., Vehring, R., 2016. Analysis of cohesion forces between monodisperse microparticles with rough surfaces. *Colloids and Surfaces a-Physicochemical and Engineering Aspects, 506*, 179-189. DOI: http://dx.doi.org/10.1016/j.colsurfa.2016.06.009

Boraey, M.A., Vehring, R., 2014. Diffusion controlled formation of microparticles. *Journal of Aerosol Science, 67*, 131-143. DOI: http://dx.doi.org/10.1016/j.jaerosci.2013.10.002

Brindley, A., 1999. The chlorofluorocarbon to hydrofluoroalkane transition: the effect on pressurized metered dose inhaler suspension stability. *Journal of Allergy and Clinical Immunology, 104*(6), s221-s226. DOI: http://dx.doi.org/10.1016/S0091-6749(99)70034-5

Cheng, W., Dunn, P., Brach, R., 2002. Surface roughness effects on microparticle adhesion. *The Journal of Adhesion, 78*(11), 929-965. DOI: http://dx.doi.org/10.1080/00218460214510

Cosgrove, T., 2010. *Colloid science: principles, methods and applications*: John Wiley & Sons. DOI: http://dx.doi.org/10.1002/9781444305395

D'Sa, D., Chan, H.-K., Chrzanowski, W., 2014. Predicting physical stability in pressurized metered dose inhalers via dwell and instantaneous force colloidal probe microscopy. *European Journal of Pharmaceutics and Biopharmaceutics, 88*(1), 129-135. DOI: http://dx.doi.org/10.1016/j.ejpb.2014.07.006

DeCarlo, P.F., Slowik, J.G., Worsnop, D.R., Davidovits, P., Jimenez, J.L., 2004. Particle morphology and density characterization by combined mobility and aerodynamic diameter measurements. Part 1: Theory. *Aerosol Science and Technology, 38*(12), 1185-1205. DOI: http://dx.doi.org/10.1080/027868290903907

Dellamary, L.A., Tarara, T.E., Smith, D.J., Woelk, C.H., Adractas, A., Costello, M.L., Gill, H., Weers, J.G., 2000. Hollow porous particles in metered dose inhalers. *Pharmaceutical Research, 17*(2), 168-174. DOI: http://dx.doi.org/10.1023/A:1007513213292

Detloff, T., Sobisch, T., Lerche, D., 2013. Instability index. *Dispersion Letters Technical, 4*, 1-4.

Elversson, J., Millqvist-Fureby, A., 2005. Particle size and density in spray drying - effects of carbohydrate properties. *Journal of Pharmaceutical Sciences, 94*(9), 2049-2060. DOI: http://dx.doi.org/10.1002/jps.20418

Engstrom, J.D., Tam, J.M., Miller, M.A., Williams, R.O., Johnston, K.P., 2009. Templated open flocs of nanorods for enhanced pulmonary delivery with pressurized metered dose inhalers. *Pharmaceutical Research, 26*(1), 101-117. DOI: http://dx.doi.org/10.1007/s11095-008-9707-z

Ensminger, D., Bond, L.J., 2011. *Ultrasonics Fundamentals Technologies and Applications* (3rd ed.): CRC Press.

Finlay, W.H., 2001. *The mechanics of inhaled pharmaceutical aerosols: an introduction*: Academic Press. DOI: http://dx.doi.org/10.1016/B978-012256971-5/50008-0

Goodrich, R.P., Crowe, J.H., Crowe, L.M., Baldeschwieler, J.D., 1991. Alterations in membrane surfaces induced by attachment of carbohydrates. *Biochemistry, 30*(21), 5313-5318. DOI: http://dx.doi.org/doi.org/10.1021/bi00235a026

Hédoux, A., 2016. Recent developments in the Raman and infrared investigations of amorphous pharmaceuticals and protein formulations: A review. *Advanced Drug Delivery Reviews, 100*, 133-146. DOI: http://dx.doi.org/10.1016/j.addr.2015.11.021

Heyder, J., 2004. Deposition of inhaled particles in the human respiratory tract and consequences for regional targeting in respiratory drug delivery. *Proceedings of the American Thoracic Society, 1*(4), 315-320. DOI: http://dx.doi.org/10.1513/pats.200409-046TA

Hinds, W.C., 2012. *Aerosol technology: properties, behavior, and measurement of airborne particles* (2nd ed.). New York: John Wiley & Sons. DOI: http://dx.doi.org/10.1016/S0021-8502(99)00571-6

Hirst, P.H., Pitcairn, G.R., Weers, J.G., Tarara, T.E., Clark, A.R., Dellamary, L.A., Hall, G., Shorr, J., Newman, S.P., 2002. In vivo lung deposition of hollow porous particles from a pressurized metered dose inhaler. *Pharmaceutical Research, 19*(3), 258-264. DOI: http://dx.doi.org/10.1023/A:1014482615914

Huang, J., Wigent, R.J., Bentzley, C.M., Schwartz, J.B., 2006. Nifedipine solid dispersion in microparticles of ammonio methacrylate copolymer and ethylcellulose binary blend for controlled drug delivery: Effect of drug loading on release kinetics. *International Journal of Pharmaceutics, 319*(1-2), 44-54. DOI: http://dx.doi.org/10.1016/j.ijpharm.2006.03.035

Huang, Y., Dai, W.-G., 2014. Fundamental aspects of solid dispersion technology for poorly soluble drugs. *Acta pharmaceutica sinica B, 4*(1), 18-25. DOI: http://dx.doi.org/10.1016/j.apsb.2013.11.001

Hunter, R.J., 2001. *Foundations of colloid science*: Oxford University Press.

Israelachvili, J.N., 2011. *Intermolecular and surface forces: revised third edition* (3rd ed.): Academic Press. DOI: http://dx.doi.org/10.1016/B978-0-12-391927-4.10014-3

Ivey, J.W., Bhambri, P., Church, T.K., Lewis, D.A., Vehring, R., 2018. Experimental investigations of particle formation from propellant and solvent droplets using a monodisperse spray dryer. *Aerosol Science and Technology*, 1-15. DOI: http://dx.doi.org/10.1080/02786826.2018.1451818

Ivey, J.W., Vehring, R., Finlay, W.H., 2015. Understanding pressurized metered dose inhaler performance. *Expert Opinion on Drug Delivery, 12*(6), 901-916. DOI: http://dx.doi.org/10.1517/17425247.2015.984683

Janes, K., Calvo, P., Alonso, M., 2001. Polysaccharide colloidal particles as delivery systems for macromolecules. *Advanced Drug Delivery Reviews, 47*(1), 83-97. DOI: http://dx.doi.org/10.1016/S0169-409X(00)00123-X

Johnson, K.A., 1996. Interfacial phenomena and phase behavior in metered dose inhaler formulations. In *Lung Biology in Health and Disease* (Vol. 94, pp. 385-415).

Jones, S.A., Martin, G.P., Brown, M., 2005. High-pressure aerosol suspensions-a novel laser diffraction particle sizing system for hydrofluoroalkane pressurised metered dose inhalers. *International Journal of Pharmaceutics, 302*(1), 154-165. DOI: http://dx.doi.org/10.1016/j.ijpharm.2005.07.001

Jones, S.A., Martin, G.P., Brown, M.B., 2006. Manipulation of beclomethasone–hydrofluoroalkane interactions using biocompatible macromolecules. *Journal of Pharmaceutical Sciences, 95*(5), 1060-1074. DOI: http://dx.doi.org/10.1002/jps.20608

Kaialy, W., Martin, G.P., Ticehurst, M.D., Royall, P., Mohammad, M.A., Murphy, J., Nokhodchi, A., 2011. Characterisation and deposition studies of recrystallised lactose from binary mixtures of ethanol/butanol for improved drug delivery from dry powder inhalers. *The AAPS journal, 13*(1), 30-43. DOI: http://dx.doi.org/10.1208/s12248-010-9241-x

Kayes, J., 1977. Pharmaceutical suspensions: relation between zeta potential, sedimentation volume and suspension stability. *Journal of Pharmacy and Pharmacology, 29*(1), 199-204. DOI: http://dx.doi.org/10.1111/j.2042-7158.1977.tb11288.x

Kipp, J., 2004. The role of solid nanoparticle technology in the parenteral delivery of poorly water-soluble drugs. *International Journal of Pharmaceutics, 284*(1-2), 109-122. DOI: http://dx.doi.org/10.1016/j.ijpharm.2004.07.019

Kleinstreuer, C., Zhang, Z., Donohue, J., 2008. Targeted drug-aerosol delivery in the human respiratory system. *Annual Review of Biomedical Engineering, 10*, 195-220. DOI: http://dx.doi.org/10.1146/annurev.bioeng.10.061807.160544

Kulshreshtha, A.K., Singh, O.N., Wall, G.M., 2010. *Pharmaceutical suspensions*. DOI: http://dx.doi.org/10.1007/978-1-4419-1087-5

Kundu, P.K., Cohen, I.M., Dowling, D.R., 2012. *Fluid mechanics* (5th ed.). New York: Academic.

Lamminen, M.O., Walker, H.W., Weavers, L.K., 2004. Mechanisms and factors influencing the ultrasonic cleaning of particle-fouled ceramic membranes. *Journal of Membrane Science, 237*(1-2), 213-223. DOI: http://dx.doi.org/10.1016/j.memsci.2004.02.031

Leal-Calderon, F., Schmitt, V., Bibette, J., 2007. *Emulsion science: basic principles*: Springer Science & Business Media. DOI: http://dx.doi.org/10.1007/978-0-387-39683-5

Lechuga-Ballesteros, D., Charan, C., Stults, C.L.M., Stevenson, C.L., Miller, D.P., Vehring, R., Tep, V., Kuo, M.C., 2008. Trileucine improves aerosol performance and stability of spray-dried powders for inhalation. *Journal of Pharmaceutical Sciences, 97*(1), 287-302. DOI: http://dx.doi.org/10.1002/jps.21078

Lerche, D., Sobisch, T., 2007. Consolidation of concentrated dispersions of nano- and microparticles determined by analytical centrifugation. *Powder Technology, 174*(1-2), 46-49. DOI: http://dx.doi.org/10.1016/j.powtec.2006.10.020

Lerche, D., Sobisch, T., 2014. Evaluation of particle interactions by in situ visualization of separation behaviour. *Colloids and Surfaces A: Physicochemical and Engineering Aspects, 440*, 122-130. DOI: http://dx.doi.org/10.1016/j.colsurfa.2012.10.015

Lesaint, C., Glomm, W.R., Lundgaard, L.E., Sjöblom, J., 2009. Dehydration efficiency of AC electrical fields on water-in-model-oil emulsions. *Colloids and Surfaces A: Physicochemical and Engineering Aspects, 352*(1-3), 63-69. DOI: http://dx.doi.org/10.1016/j.colsurfa.2009.09.051

Li, H.-Y., Seville, P.C., 2010. Novel pMDI formulations for pulmonary delivery of proteins. *International Journal of Pharmaceutics, 385*(1), 73-78. DOI: http://dx.doi.org/10.1016/j.ijpharm.2009.10.032

Lieberman, H.A., Rieger, M.M., Banker, G.S., 1996. *Pharmaceutical dosage forms: Disperse systems* (2nd ed. Vol. 2): Marcel Dekker, New York. DOI: http://dx.doi.org/10.1002/jps.2600790927

Liu, W.R., Sun, D.J., Li, C.F., Liu, Q., Xu, H., 2006. Formation and stability of paraffin oil-in-water nano-emulsions prepared by the emulsion inversion point method. *Journal of Colloid and Interface Science, 303*(2), 557-563. DOI: http://dx.doi.org/10.1016/j.jcis.2006.07.055

Marsh, D., 2013. *Handbook of lipid bilayers, 2nd Edition*: Boca Raton: CRC press. DOI: http://dx.doi.org/10.1201/b11712

Mayer, H., Mentler, A., Papakyriacou, M., Rampazzo, N., Marxer, Y., Blum, W., 2002. Influence of vibration amplitude on the ultrasonic dispersion of soils. *International Agrophysics, 16*(1), 53-60.

Mengual, O., Meunier, G., Cayre, I., Puech, K., Snabre, P., 1999a. Characterisation of instability of concentrated dispersions by a new optical analyser: the TURBISCAN MA 1000. *Colloids and Surfaces A: Physicochemical and Engineering Aspects, 152*(1), 111-123. DOI: http://dx.doi.org/10.1016/S0927-7757(98)00680-3

Mengual, O., Meunier, G., Cayré, I., Puech, K., Snabre, P., 1999b. TURBISCAN MA 2000: multiple light scattering measurement for concentrated emulsion and suspension instability analysis. *Talanta, 50*(2), 445-456. DOI: http://dx.doi.org/10.1016/S0039-9140(99)00129-0

Müller, R.H., MaÈder, K., Gohla, S., 2000. Solid lipid nanoparticles (SLN) for controlled drug delivery–a review of the state of the art. *European Journal of Pharmaceutics and Biopharmaceutics, 50*(1), 161-177. DOI: http://dx.doi.org/10.1016/S0939-6411(00)00087-4

Myrdal, P.B., Sheth, P., Stein, S.W., 2014. Advances in metered dose inhaler technology: formulation development. *AAPS PharmSciTech, 15*(2), 434-455. DOI: http://dx.doi.org/10.1208/s12249-013-0063-x

Nielloud, F., 2000. *Pharmaceutical emulsions and suspensions: revised and expanded*: CRC Press.

Ooi, J., Traini, D., Boyd, B.J., Gaisford, S., Young, P.M., 2015. Determination of physical and chemical stability in pressurised metered dose inhalers: potential new techniques. *Expert Opinion on Drug Delivery, 12*(10), 1661-1675. DOI: http://dx.doi.org/10.1517/17425247.2015.1046834

Pasquali, R.C., Taurozzi, M.P., Bregni, C., 2008. Some considerations about the hydrophilic-lipophilic balance system. *International Journal of Pharmaceutics, 356*(1-2), 44-51. DOI: http://dx.doi.org/10.1016/j.ijpharm.2007.12.034

Passerini, N., Albertini, B., Perissutti, B., Rodriguez, L., 2006. Evaluation of melt granulation and ultrasonic spray congealing as techniques to enhance the dissolution of praziquantel. *International Journal of Pharmaceutics, 318*(1-2), 92-102. DOI: http://dx.doi.org/10.1016/j.ijpharm.2006.03.028

Patravale, V., Kulkarni, R., 2004. Nanosuspensions: a promising drug delivery strategy. *Journal of Pharmacy and Pharmacology, 56*(7), 827-840. DOI: http://dx.doi.org/10.1211/0022357023691

Rabinow, B.E., 2004. Nanosuspensions in drug delivery. *Nature reviews. Drug discovery, 3*(9), 785. DOI: http://dx.doi.org/10.1038/nrd1494

Raghavan, S., Schuessel, K., Davis, A., Hadgraft, J., 2003. Formation and stabilisation of triclosan colloidal suspensions using supersaturated systems. *International Journal of Pharmaceutics, 261*(1-2), 153-158. DOI: http://dx.doi.org/10.1016/S0378-5173(03)00299-0

Rahate, A.R., Nagarkar, J.M., 2007. Emulsification of vegetable oils using a blend of nonionic surfactants for cosmetic applications. *Journal of Dispersion Science and Technology, 28*(7), 1077-1080. DOI: http://dx.doi.org/10.1080/01932690701524802

Ramachandran, K., Suganya, T., Gandhi, N.N., Renganathan, S., 2013. Recent developments for biodiesel production by ultrasonic assist transesterification using different heterogeneous catalyst: a review. *Renewable and sustainable energy reviews, 22*, 410-418. DOI: http://dx.doi.org/10.1016/j.rser.2013.01.057

Rogueda, P., 2005. Novel hydrofluoroalkane suspension formulations for respiratory drug delivery. *Expert Opinion on Drug Delivery, 2*(4), 625-638. DOI: http://dx.doi.org/10.1517/17425247.2.4.625

Rogueda, P.G., Price, R., Smith, T., Young, P.M., Traini, D., 2011. Particle synergy and aerosol performance in non-aqueous liquid of two combinations metered dose inhalation formulations: An AFM and Raman investigation. *Journal of Colloid and Interface Science, 361(2)*(2), 649-655. DOI: http://dx.doi.org/10.1016/j.jcis.2011.05.073

Rouquerol, F., Rouquerol, J., Sing, K.S., Llewellyn, P., Maurin, G., 2014. *Adsorption by powders and porous solids: principles, methodology and applications* (2nd ed.): Academic press. DOI: http://dx.doi.org/10.1016/B978-0-08-097035-6.00007-3

Sato, K., Li, J.G., Kamiya, H., Ishigaki, T., 2008. Ultrasonic dispersion of TiO2 nanoparticles in aqueous suspension. *Journal of the American Ceramic Society, 91*(8), 2481-2487. DOI: http://dx.doi.org/10.1111/j.1551-2916.2008.02493.x

Schramm, L.L., 2014. *Emulsions, Foams, Suspensions, and Aerosols: microscience and applications*: John Wiley & Sons. DOI: http://dx.doi.org/10.1002/9783527679478

Selvam, P., Peguin, R.P., Chokshi, U., da Rocha, S.R., 2006. Surfactant design for the 1, 1, 1, 2-tetrafluoroethane−water interface: ab initio calculations and in situ high-pressure tensiometry. *Langmuir, 22*(21), 8675-8683. DOI: http://dx.doi.org/10.1021/la061015z

Sesis, A., Hodnett, M., Memoli, G., Wain, A.J., Jurewicz, I., Dalton, A.B., Carey, J.D., Hinds, G., 2013. Influence of acoustic cavitation on the controlled ultrasonic dispersion of carbon nanotubes. *Journal of Physical Chemistry B, 117*(48), 15141-15150. DOI: http://dx.doi.org/10.1021/jp410041y

Sidhu, B., Washington, C., Davis, S., Purewal, T., 1993. Electrophoretic properties of lactose and salbutamol sulfate suspensions in halogenated solvents. *Langmuir, 9*(3), 839-843. DOI: http://dx.doi.org/10.1021/la00027a038

Sirignano, W., Mehring, C., 2000. Review of theory of distortion and disintegration of liquid streams. *Progress in Energy and Combustion Science, 26*(4-6), 609-655. DOI: http://dx.doi.org/10.1016/S0360-1285(00)00014-9

Smyth, H.D., 2003. The influence of formulation variables on the performance of alternative propellant-driven metered dose inhalers. *Advanced Drug Delivery Reviews, 55*(7), 807-828. DOI: http://dx.doi.org/10.1016/S0169-409X(03)00079-6

Stein, S.W., Sheth, P., Hodson, P.D., Myrdal, P.B., 2014. Advances in metered dose inhaler technology: hardware development. *AAPS PharmSciTech, 15*(2), 326-338. DOI: http://dx.doi.org/10.1208/s12249-013-0062-y

Stevenson, P., 2012. *Foam engineering: fundamentals and applications*: John Wiley & Sons. DOI: http://dx.doi.org/10.1002/9781119954620

Taurozzi, J.S., Hackley, V.A., Wiesner, M.R., 2011. Ultrasonic dispersion of nanoparticles for environmental, health and safety assessment - issues and recommendations. *Nanotoxicology, 5*(4), 711-729. DOI: http://dx.doi.org/10.3109/17435390.2010.528846

Traini, D., Rogueda, P., Young, P., Price, R., 2005. Surface energy and interparticle force correlation in model pMDI formulations. *Pharmaceutical Research, 22*(5), 816-825. DOI: http://dx.doi.org/10.1007/s11095-005-2599-2

Traini, D., Young, P.M., Rogueda, P., Price, R., 2007. In vitro investigation of drug particulates interactions and aerosol performance of pressurised metered dose inhalers. *Pharmaceutical Research, 24*(1), 125-135. DOI: http://dx.doi.org/10.1007/s11095-006-9130-2

Vasconcelos, T., Sarmento, B., Costa, P., 2007. Solid dispersions as strategy to improve oral bioavailability of poor water soluble drugs. *Drug Discovery Today, 12*(23), 1068-1075. DOI: http://dx.doi.org/10.1016/j.drudis.2007.09.005

Vehring, R., 2008. Pharmaceutical particle engineering via spray drying. *Pharmaceutical Research, 25*(5), 999-1022. DOI: http://dx.doi.org/10.1007/s11095-007-9475-1

Vehring, R., Foss, W.R., Lechuga-Ballesteros, D., 2007. Particle formation in spray drying. *Journal of Aerosol Science, 38*(7), 728-746. DOI: http://dx.doi.org/10.1016/j.jaerosci.2007.04.005

Vehring, R., Lechuga-Ballesteros, D., Joshi, V., Noga, B., Dwivedi, S.K., 2012. Cosuspensions of microcrystals and engineered microparticles for uniform and efficient delivery of respiratory therapeutics from pressurized metered dose inhalers. *Langmuir, 28*(42), 15015-15023. DOI: http://dx.doi.org/10.1021/la302281n

Verma, S., Kumar, S., Gokhale, R., Burgess, D.J., 2011. Physical stability of nanosuspensions: investigation of the role of stabilizers on Ostwald ripening. *International Journal of Pharmaceutics, 406*(1-2), 145-152. DOI: http://dx.doi.org/10.1016/j.ijpharm.2010.12.027

Voss, A., Finlay, W.H., 2002. Deagglomeration of dry powder pharmaceutical aerosols. *International Journal of Pharmaceutics, 248*(1-2), 39-50. DOI: http://dx.doi.org/10.1016/S0378-5173(02)00319-8

Wang, H., Barona, D., Oladepo, S., Williams, L., Hoe, S., Lechuga-Ballesteros, D., Vehring, R., 2017a. Macro-Raman spectroscopy for bulk composition and homogeneity analysis of multi-component pharmaceutical powders. *Journal of Pharmaceutical and Biomedical Analysis, 141*, 180-191. DOI: http://dx.doi.org/10.1016/j.jpba.2017.04.003

Wang, H., Bhambri, P., Ivey, J., Vehring, R., 2017b. Design and pharmaceutical applications of a low-flow-rate single-nozzle impactor. *International Journal of Pharmaceutics, 533*(1), 14-25. DOI: http://dx.doi.org/10.1016/j.ijpharm.2017.09.047

Wang, H., Boraey, M.A., Williams, L., Lechuga-Ballesteros, D., Vehring, R., 2014. Low-frequency shift dispersive Raman spectroscopy for the analysis of respirable dosage forms. *International Journal of Pharmaceutics, 469*(1), 197-205. DOI: http://dx.doi.org/10.1016/j.ijpharm.2014.04.058

Wang, H., Nobes, D.S., Finlay, W.H., Vehring, R., 2019a. Agitation method affects colloidal stability of pharmaceutical suspensions, *Respiratory Drug Delivery*, Lisbon, Portugal.

Wang, H., Nobes, D.S., Finlay, W.H., Vehring, R., 2019b. Increasing particle surface roughness as a promising strategy to improve colloidal stability of pharmaceutical suspensions, *Respiratory Drug Delivery*, Lisbon, Portugal.

Wang, H., Nobes, D.S., Vehring, R., 2019c. Particle surface roughness improves colloidal stability of pressurized pharmaceutical suspensions. *Pharmaceutical Research, 36*(3), 43. DOI: http://dx.doi.org/10.1007/s11095-019-2572-0

Wang, H., Tan, P., Barona, D., Li, G., Hoe, S., Lechuga-Ballesteros, D., Nobes, D.S., Vehring, R., 2018a. Characterization of the suspension stability of pharmaceuticals using a shadowgraphic imaging method. *International Journal of Pharmaceutics, 548*(1), 128-138. DOI: http://dx.doi.org/10.1016/j.ijpharm.2018.06.053

Wang, H., Tan, P., Barona, D., Li, G., Hoe, S., Lechuga-Ballesteros, D., Nobes, D.S., Vehring, R., 2018b. A new shadowgraphic imaging method for the suspension stability analysis of pressurized metered dose inhalers, *Respiratory Drug Delivery*, Tucson, Arizona, US, 573-578.

Wang, Y., Zheng, Y., Zhang, L., Wang, Q., Zhang, D., 2013. Stability of nanosuspensions in drug delivery. *Journal of Controlled Release, 172*(3), 1126-1141. DOI: http://dx.doi.org/10.1016/j.jconrel.2013.08.006

Waterman, K.C., Adami, R.C., 2005. Accelerated aging: prediction of chemical stability of pharmaceuticals. *International Journal of Pharmaceutics, 293*(1-2), 101-125. DOI: http://dx.doi.org/10.1016/j.ijpharm.2004.12.013

Weers, J., Tarara, T., 2014. The PulmoSphere™ platform for pulmonary drug delivery. *Therapeutic Delivery, 5*(3), 277-295. DOI: http://dx.doi.org/10.4155/tde.14.3

Weyna, D.R., Shattock, T., Vishweshwar, P., Zaworotko, M.J., 2009. Synthesis and structural characterization of cocrystals and pharmaceutical cocrystals: mechanochemistry vs slow evaporation from solution. *Crystal Growth and Design, 9*(2), 1106-1123. DOI: http://dx.doi.org//10.1021/cg800936d

Williams, R.O., Repka, M., Liu, J., 1998. Influence of propellant composition on drug delivery from a pressurized metered-dose inhaler. *Drug Development and Industrial Pharmacy, 24*(8), 763-770. DOI: http://dx.doi.org/10.3109/03639049809082724

Wu, L., da Rocha, S.R., 2007. Biocompatible and biodegradable copolymer stabilizers for hydrofluoroalkane dispersions: a colloidal probe microscopy investigation. *Langmuir, 23*(24), 12104-12110. DOI: http://dx.doi.org/10.1021/la702108x

Wu, L., da Rocha, S.R., 2011. Nanoparticle-stabilized colloids in compressible hydrofluoroalkanes. *Langmuir, 27*(17), 10501-10506. DOI: http://dx.doi.org/10.1021/la201906f

Wu, L., Zhang, J., Watanabe, W., 2011. Physical and chemical stability of drug nanoparticles. *Advanced Drug Delivery Reviews, 63*(6), 456-469. DOI: http://dx.doi.org/10.1016/j.addr.2011.02.001

Young, P.M., Price, R., Lewis, D., Edge, S., Traini, D., 2003. Under pressure: predicting pressurized metered dose inhaler interactions using the atomic force microscope. *Journal of Colloid and Interface Science, 262*(1), 298-302. DOI: http://dx.doi.org/10.1016/S0021-9797(03)00032-8

Zhang, J., Zografi, G., 2001. Water vapor absorption into amorphous sucrose-poly (vinyl pyrrolidone) and trehalose–poly (vinyl pyrrolidone) mixtures. *Journal of Pharmaceutical Sciences, 90*(9), 1375-1385. DOI: http://dx.doi.org/10.1002/jps.1090

APPENDICES

Appendix I Suspension Tester Design

I.1. Hardware

A detailed list of the components used to build the new suspension tester is provided in the following **Table I.1** with each of the individual components highlighted in **Figure I.1**. Most of the components were directly purchased from the corresponding vendors. The outer housing for the suspension samples and the LED screen is machined from impact-resistant ABS sheets with a water jet cutter according to the drawings provided below. The interior of the housing is covered with anti-reflective paper to prevent scattered light from interfering with the image acquisition. An external transformer is needed to provide the correct power to the Pulsar LED controller.

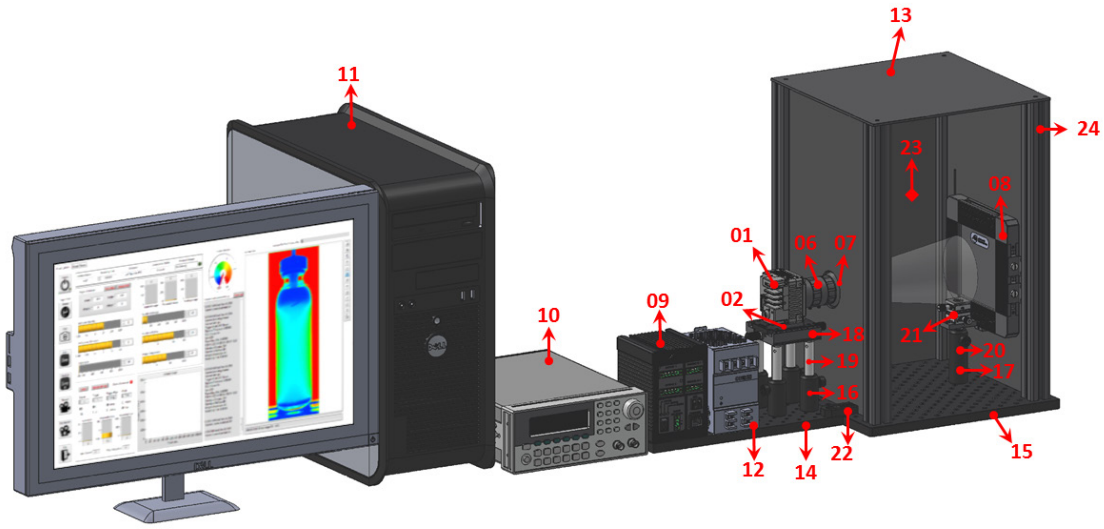

Figure I.1. CAD model of the suspension tester with indexed component numbers.

Table I.1. Components used for the suspension tester.

#	Vendor/Manufacturer	Item	Model	Q
01	Graftek Imaging	JAI	High-res mono camera	SP-5000M-PMCL	1
02		JAI	Camera mounting plate	MP-42	1
03		NI	Camera link frame grabber	PCIe-1433 781169-01	1
04		NI	Camera data cables	199744-02	2
05		NI	Camera trigger cable	763389-01	1
06		Edmund	Camera lens	86571	1
07		Midwest	Polarizing Filter	PR120-46	1
08	Advanced Illumination		Backlighting LED	CX0404-0530C5	1
09			LED controller	Pulsar 320	1
10	Newark	Tektronix	Function generator	43Y2834	1
11	Dell		Computer tower & Monitor	U2417Ht&DCG6RD2	1
12	McMaster-Carr		Power supply for LED controller	7009K81	1
13			1/4" ABS sheets for housing	8586K371	2
14	Thorlabs		Aluminum Breadboard	MB1530/M	1
15			Aluminum Breadboard	MB3030D/M	1
16			Post Holder (for camera)	PH50/M	4
17			Post Holder (for sample)	PH75/M	1
18			Dovetail Translation Stage	DTS25/M	1
19			Optical Post (for camera)	TR75/M	4
20			Optical Post (for sample)	TR50/M	1
21			XY Translation Stage with Baseplate	DT12XY/M	1

22	Mounting Base 25mmx58mmx10mm	BA1S/M	2
23	Black Flocked Paper Sheet 30"x30"	BFP1	1
24	Optical Construction Rails	XE25L300/M	4

I.2. Custom-made components

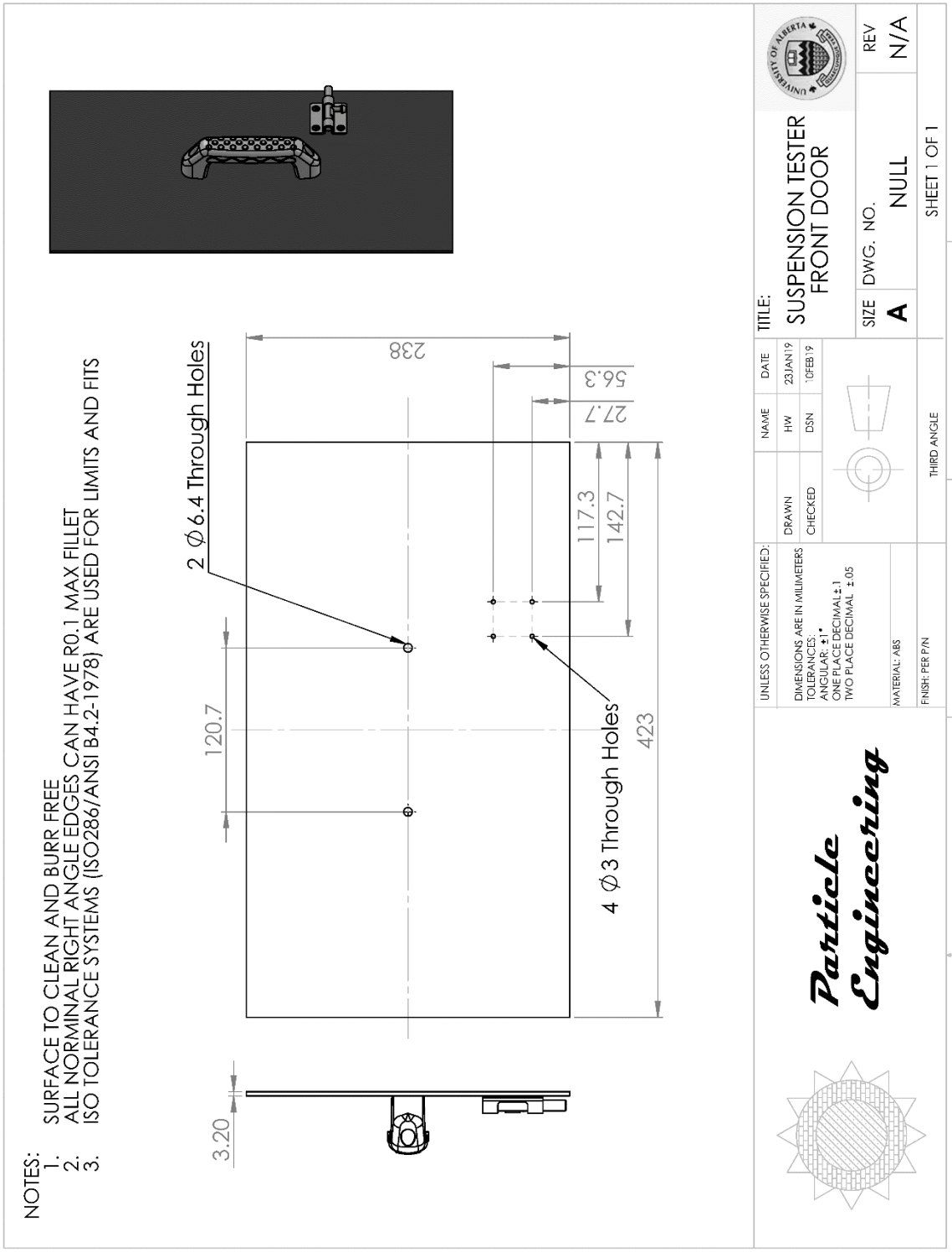

Figure I.2. CAD drawing for the front door of the light-proof sample chamber.

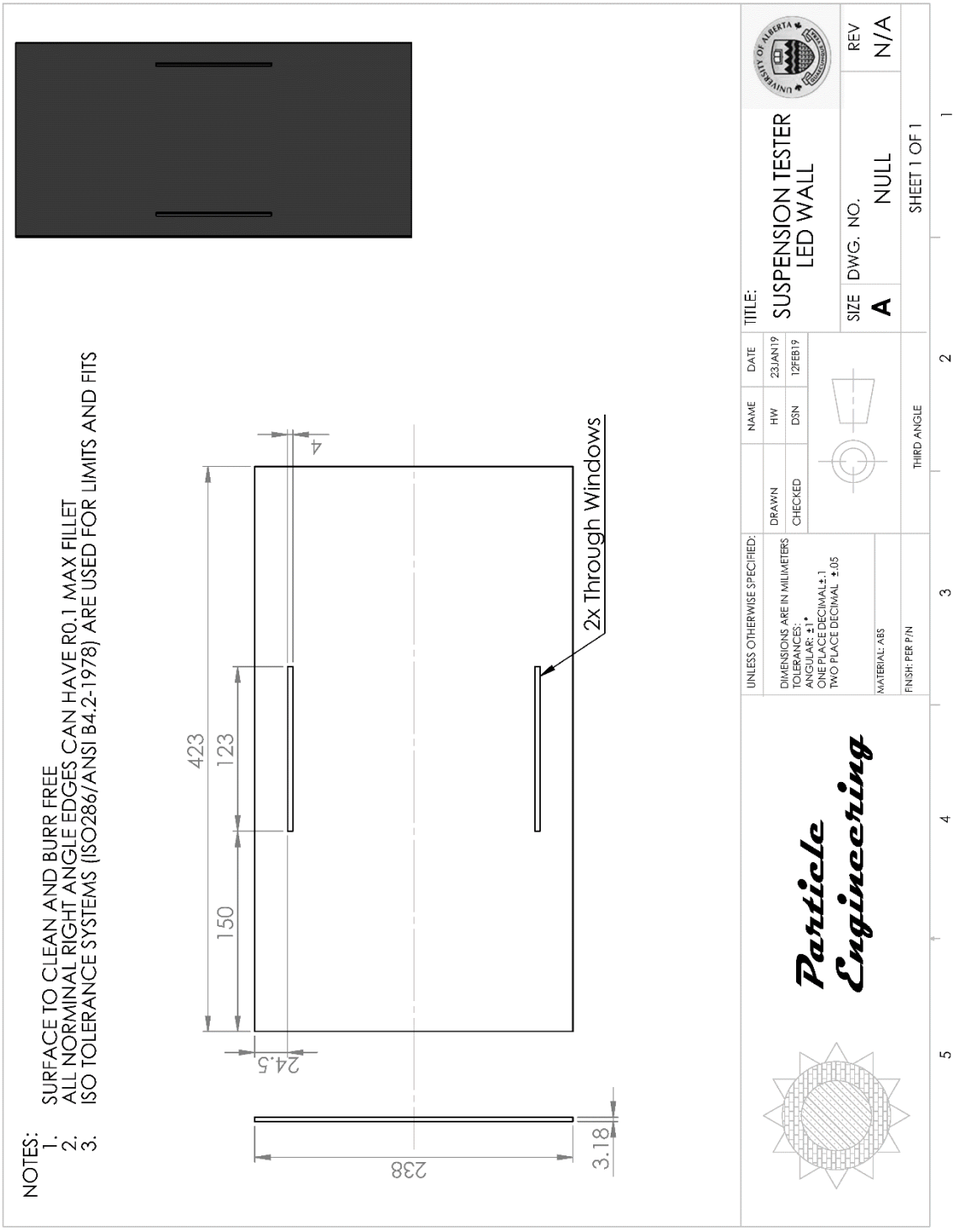

Figure I.3. CAD drawing for the side wall of the light-proof sample chamber for the LED panel installation.

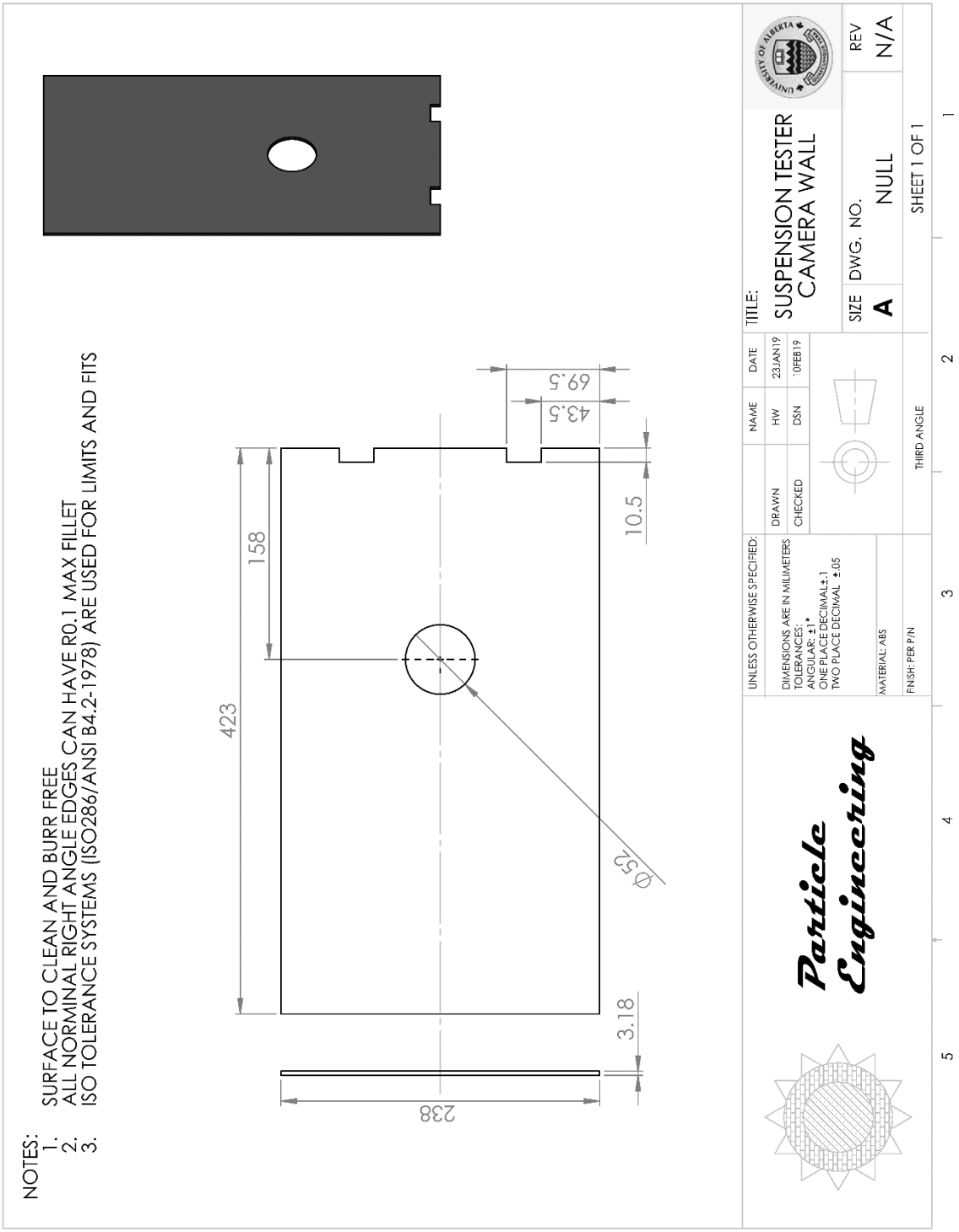

Figure I.4. CAD drawing for the side wall of the light-proof sample chamber with an optical window for the camera lens.

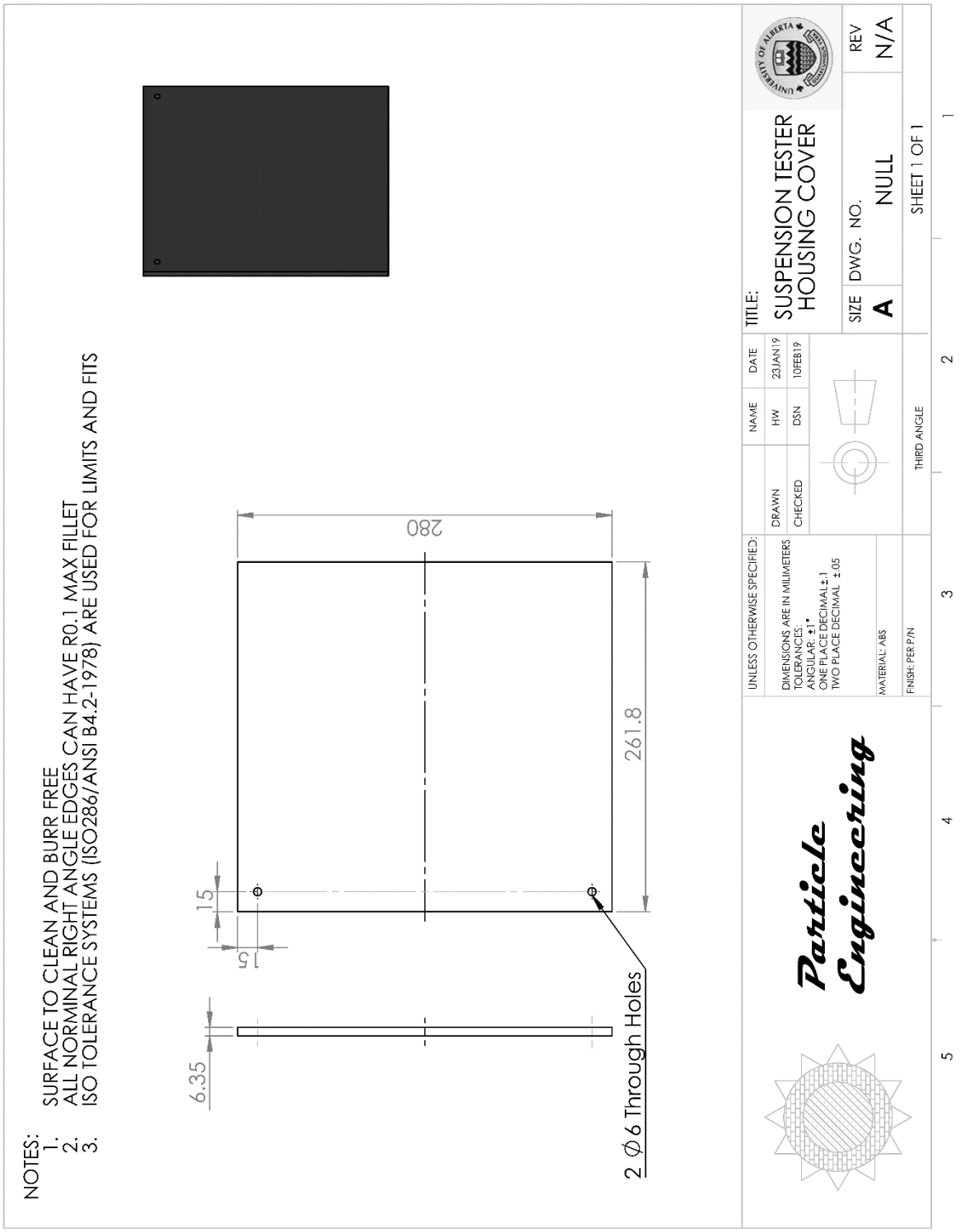

Figure I.5. CAD drawing for the top cover of the light-proof sample chamber.

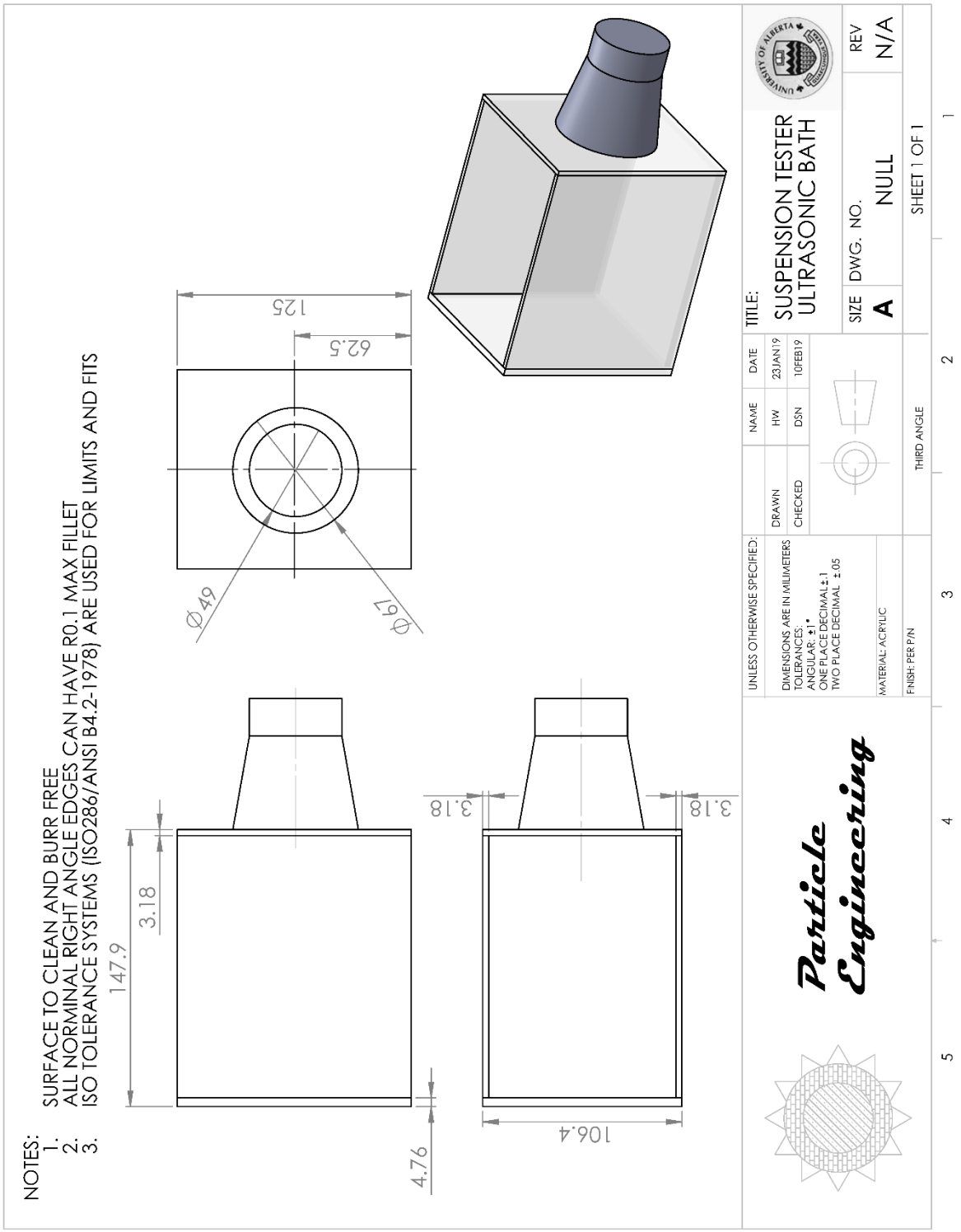

Figure I.6. CAD drawing for the custom-made transparent ultrasonic bath for the controlled initial sample agitation.

I.3. Cable connection

The connection of data and power cables for the suspension tester is shown in **Figure I.7**. A Camera Link frame grabber card (PCIe-1433, National Instruments Corp., Austin, TX, USA) first needs to be installed in the computer for communication with the camera. The camera is then connected to the frame grabber using two 26-pin MDR Camera Link cables, enabling high frequency up to 137 frames/second continuous acquisition of images with full resolution. The two cables also supply power directly to the camera. A standard USB cable is used to connect the Pulsar controller and the computer for direct control of the LED with the developed software shown below.

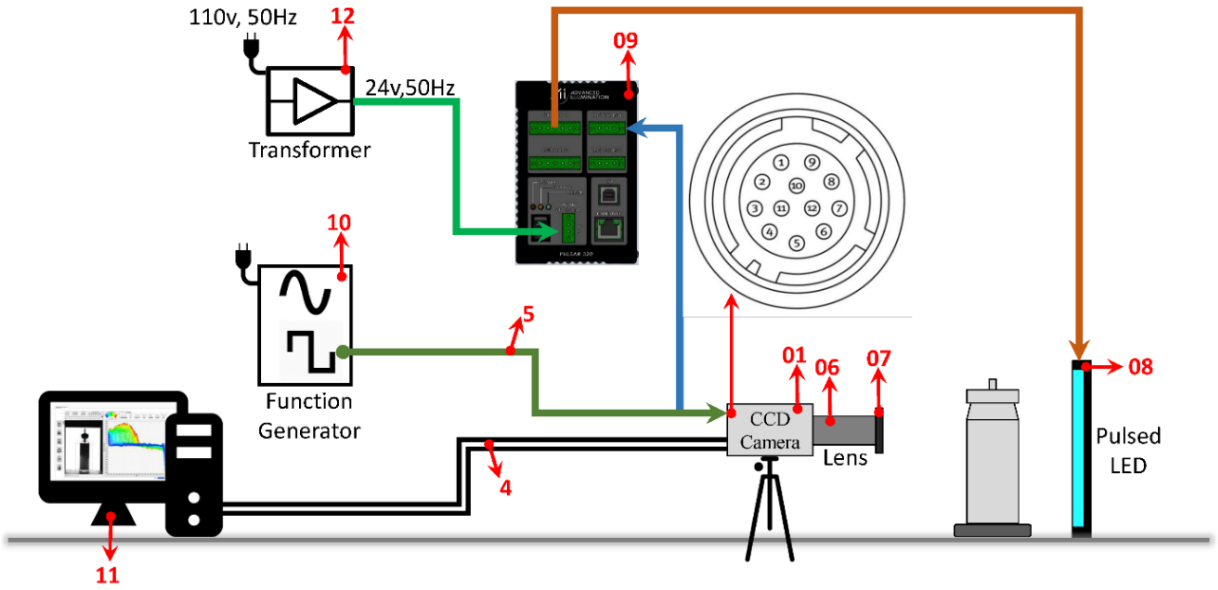

Figure I.7. Schematic diagram of the suspension tester showing the connection of the power and data cables. The inset shows the configuration of the connector for triggering signal input.

Square waves produced by an external function generator are used to synchronize the camera and the backlighting LED. According to the configuration of the 12-pin connector shown as the inset in **Figure I.7**, pin 10 of the camera connector is used for triggering signal input, and pin 1 is

used as a ground line. Corresponding lines of the triggering cable 5 are connected to the function generator using a BNC connector. The same signal is sent to the Pulsar controller and modulated before it is sent to trigger the LED panel. The illumination time of the LED panel during each triggering cycle is controlled by the pulse width of the modulated signal. Synchronization of the camera and the LED screen using the same signal allows the high-intensity output of the light source and significantly reduces the exposure time required for high-contrast images, especially for concentrated suspension samples, therefore, giving simultaneous illumination and high temporal resolution features of the shadowgraphic imaging technique.

Despite the fact that the camera and LED panel are synchronized using the same triggering signal, extra caution must be paid when setting the exposure time of the camera and the illumination time of the LED panel, or the pulse width of the modulated signal. It is necessary to set the camera exposure time shorter than the illumination time of the light source. Triggering delays may be needed in applications where images are acquired at high frame rates ~100 Hz but are not much of a concern for most suspension stability testing applications.

Appendix II Calibration of Transmission Intensity

Based the transmission intensity map shown in **Figure 2.5**, the 10 plots were fitted using a linear equation to get the dependence of their slopes and intercepts on the LED input power. As the results shown in **Figure II.1** and **Figure II.2**, both showed a good linear dependence on the power of the light source. Using the fitting parameters, transmission intensities through clear propellant, T^{a}_{Clear}, measured at an arbitrary combination of exposure time and LED power can now be calculated using a single **Eqn.(II.1)** with good accuracy. This is especially important for measuring highly concentrated suspensions when a long exposure time or a high LED power is needed for better image contrast but the corresponding transmission intensities through clear propellant, T^{a}_{Clear}, cannot be directly measured due to the limited full well capacity of the camera pixels.

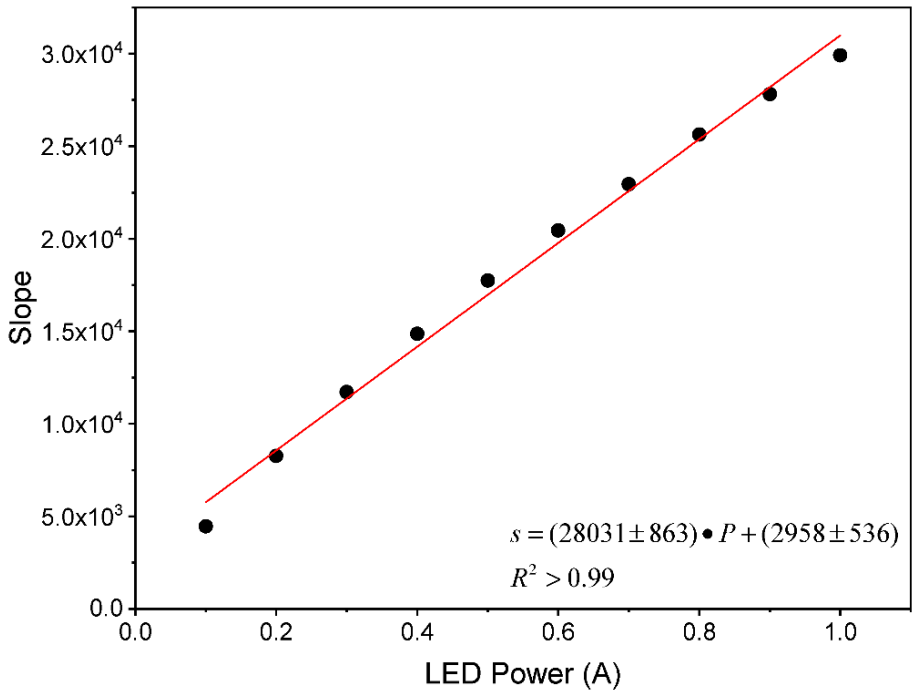

Figure II.1. Slopes of the transmission intensity vs. exposure time curves in **Figure 2.5** shows a linear dependence on the applied LED power.

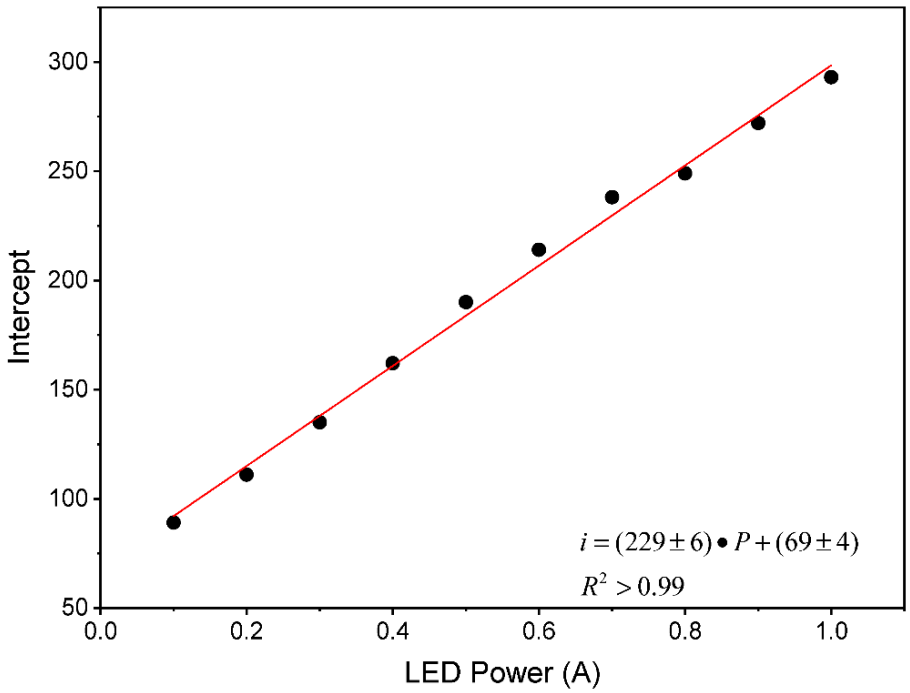

Figure II.2. Intercepts of the transmission intensity vs. exposure time curves in **Figure 2.5** shows a linear dependence on the applied LED power.

$$\begin{aligned} & I(P,t) \\ & = s(P) \cdot t + i(P) \\ & = [(28031 \pm 863) \cdot P + (2958 \pm 536)] \cdot t + [(229 \pm 6) \cdot P + (69 \pm 4)] \end{aligned} \tag{II.1}$$

Since the equation is used for calculating light signal that can be detected by the sensor, any changes that would affect the amount of detectable signal should be avoided such as changing the aperture, rotating the polarizing filter, adjusting the focus of the lens, and switching the LED panel. Otherwise, the calibration equation needs to be updated every time after the changes are made.

Appendix III Single-Nozzle Impactor Used for pMDI Particle Extraction

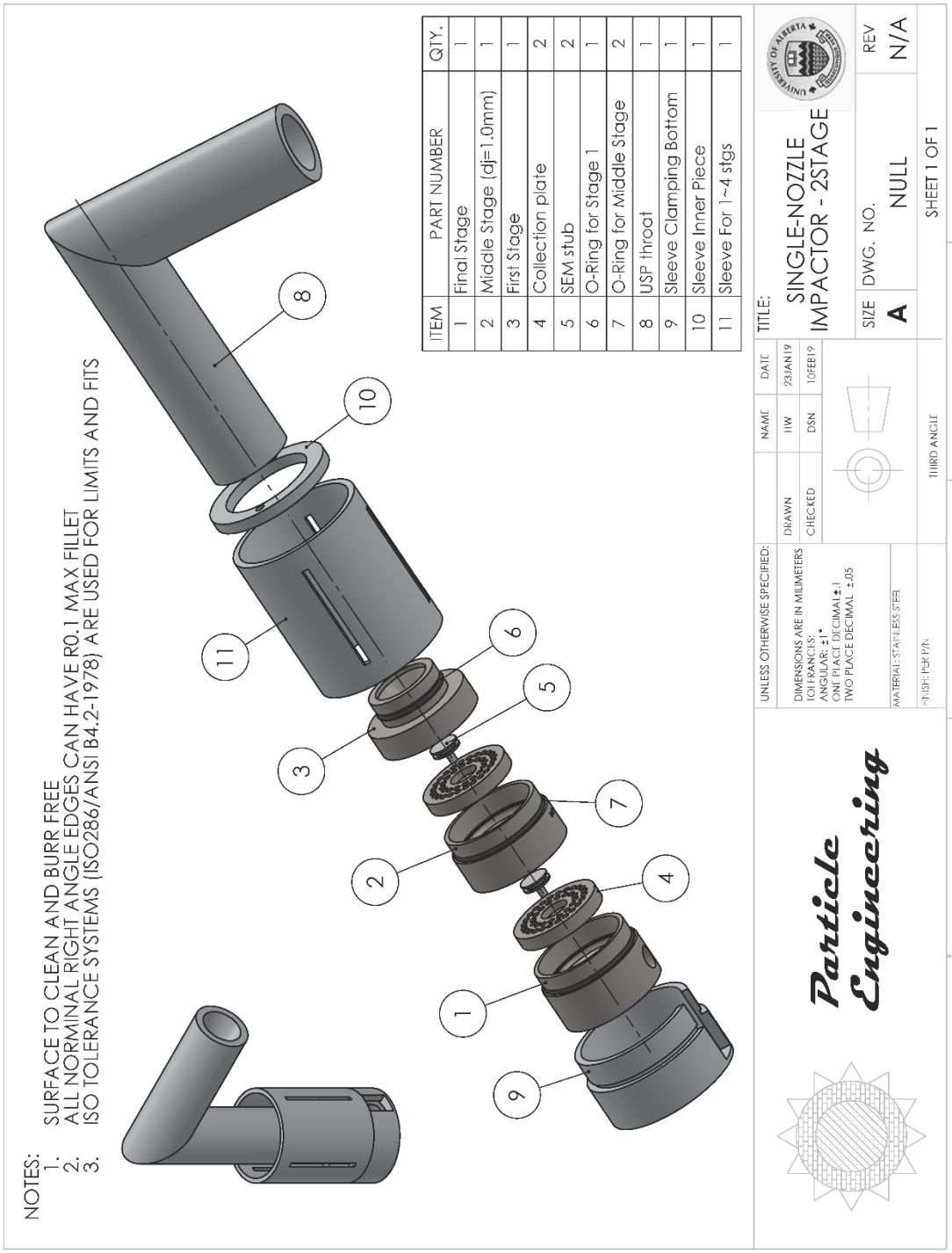

Figure III.1. A single-stage configuration of the single-nozzle impactor for extracting particles from pMDIs for spectroscopic and morphological analysis.

Appendix IV Macro-Raman Spectroscopy System

Figure IV.1. CAD model for the custom-built macro-Raman spectroscopy system.

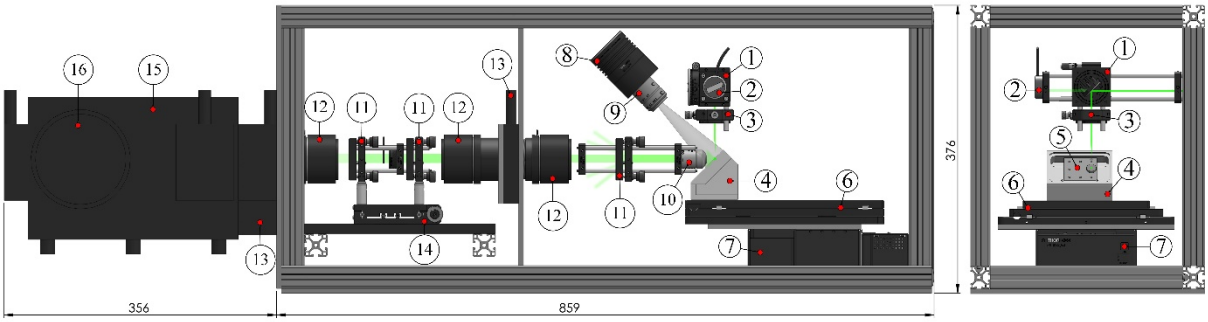

Figure IV.2. Front and side view of the dispersive macro-Raman system signal collection chamber (dimension in millimeter).

Table IV.1. Key components in the excitation chamber of the macro-Raman spectroscopy.

#	Vendor/Manufacturer	Item	Model
01	Thorlabs Inc.	90:10 (R:T) Beam Splitter	BSX10
02		Laser Power Meter	S121C & PM100D
03		Plano-convex Lens	LA1255
04	Custom	Block Sample Holder	-
05	Ted Pella Inc.	Pin Stub Holder	15334-33
06	Thorlabs Inc.	X-Y Scanning Stage	MLS 203-1
07		Motorized Stage	MLJ050-M
08		Tungsten-Halogen Lamp	QTH10-M
09		Camera & Lens	DCC1645C, MVL25TM23
10		Plan Achromat Objective	RMS10X
11	Ondax Inc.	Narrow-band Notch Filters	114-ER317-001 LLN-532.2-OD4
12	Thorlabs Inc.	Focusing Lens	AF Nikkor 50 mm f/1.8D
13	Princeton Instruments Inc.	Manual Slit	-
14	Thorlabs Inc.	Single Axis Stage	LT1-M

15	Princeton Instruments Inc.	Spectrograph	SP2500
16		CCD Sensor	PIXIS: 400BR eXcelon

Appendix V Suspension Imaging Software

V.1. LabVIEW Front panel – Suspension Imaging

The software used for both data acquisition and preliminary data processing was developed in LabVIEW 2016 (64-bit, National Instruments Corp., Austin, TX, USA) with NI Vision Acquisition and Vision Development modules and requires a computer running 64-bit Microsoft Windows 7. The software uses an event-driving programming method to control cameras with Camera Link interfaces and therefore can be used for many other imaging applications. Briefly, the software allows full control of the camera including the bit depth (8, 10, 12), digital gain (100 - 1600), exposure time, frame rate (< 137 Hz), triggering mode (manual, timed, external signal), acquisition time, acquisition mode (live, snap, record) and so on. Control unit for the Pulsar LED and controller has also been incorporated into the software for simultaneous control of the whole imaging system. Interfaces of the software are shown below in **Figure V.1** and **Figure V.2**. The Image Process tab of the software allows preliminary data processing and produces absolute transmission profiles, $T_{t,h}^{\mathrm{a}}$.

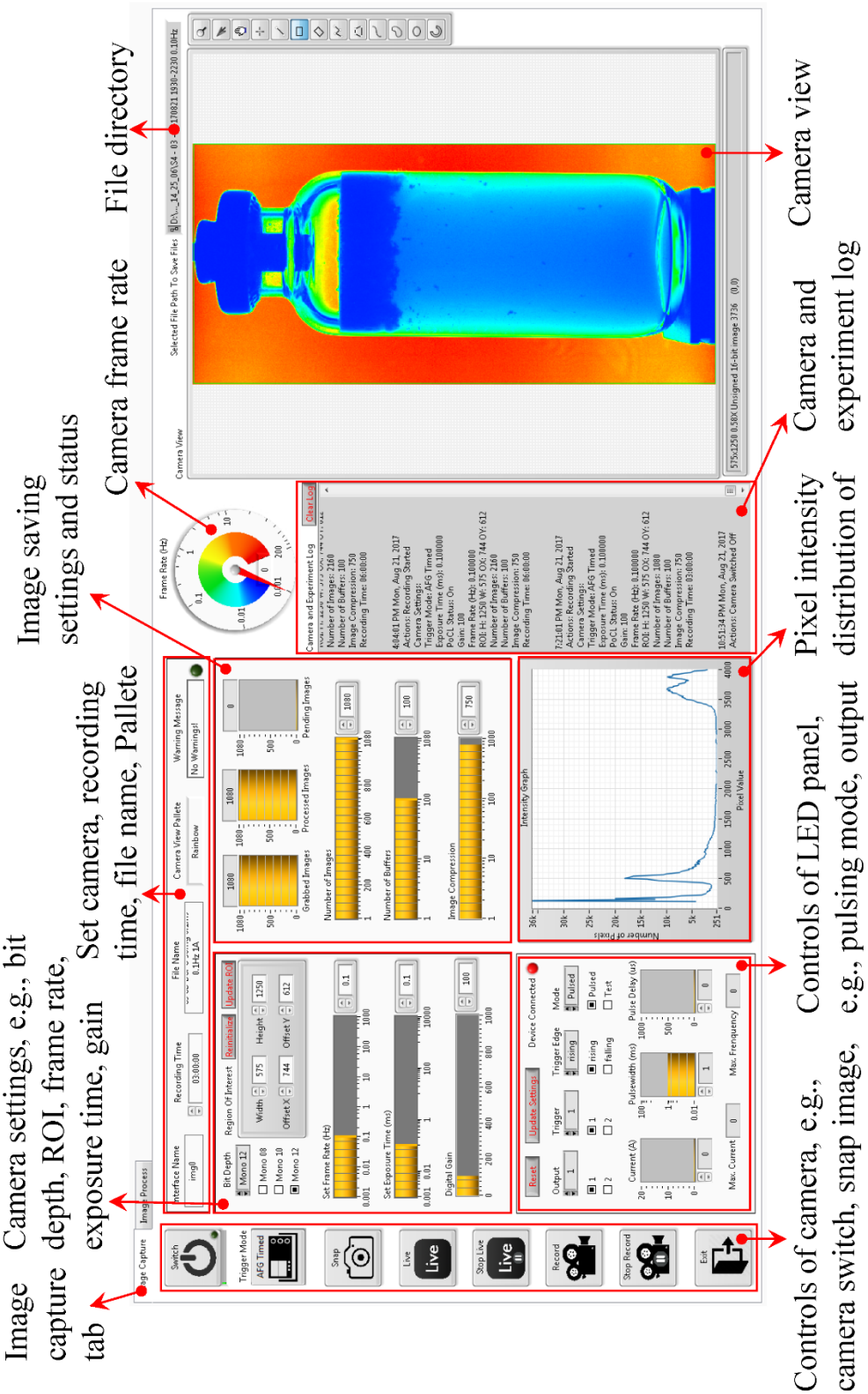

Figure V.1. The Suspension Imaging software interface for data acquisition.

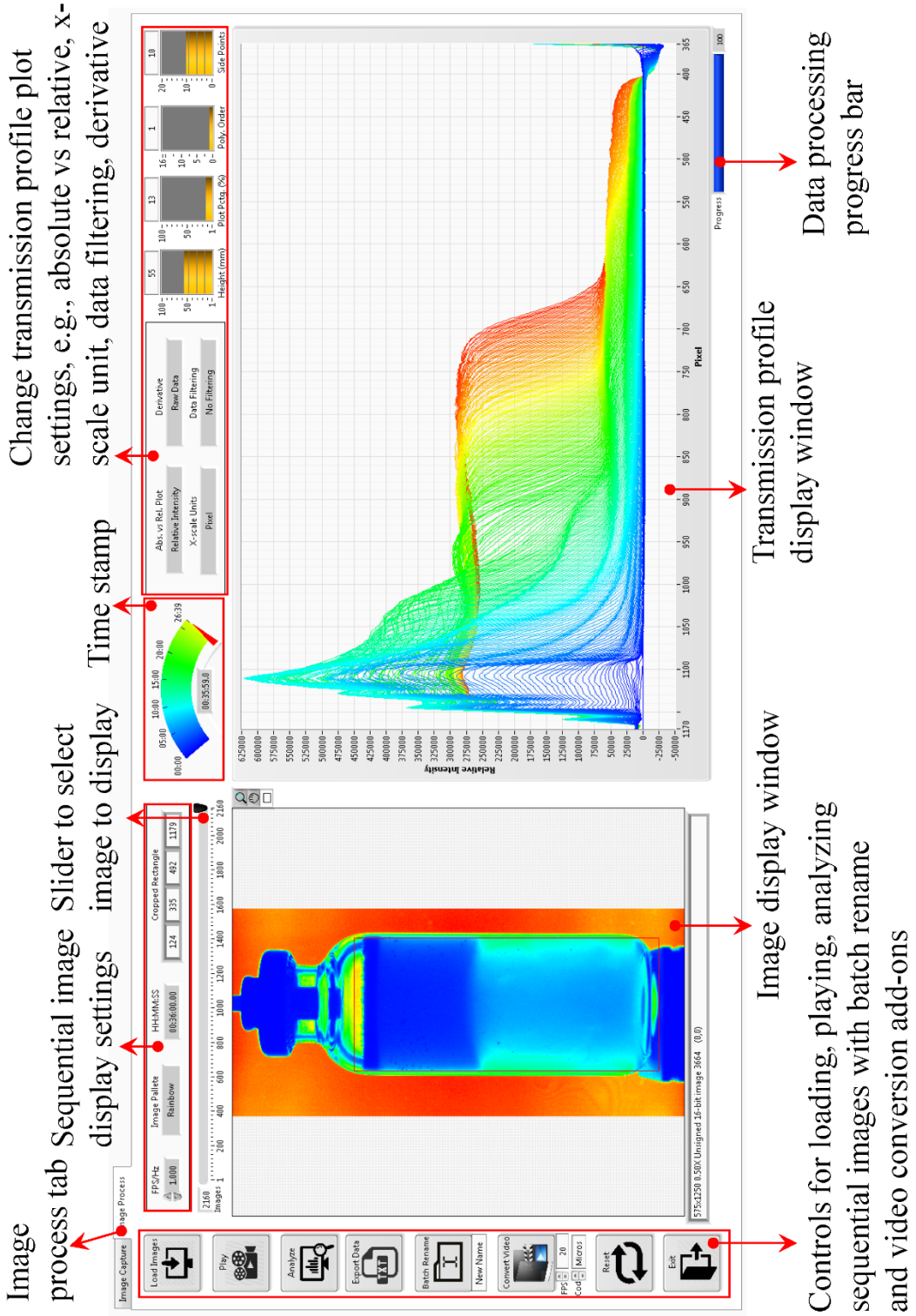

Figure V.2. The Suspension Imaging software interface for data processing.

V.2. LabVIEW Block diagram – Suspension Imaging

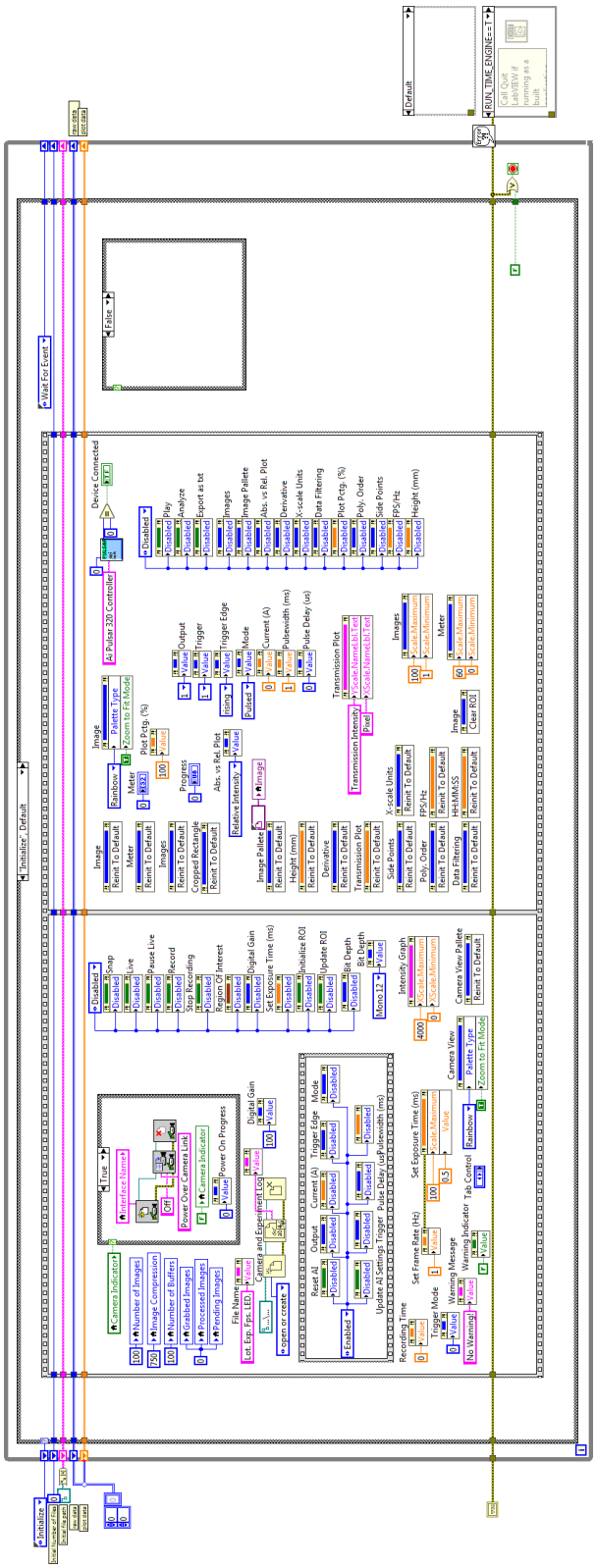

Initialization of all settings before each run.

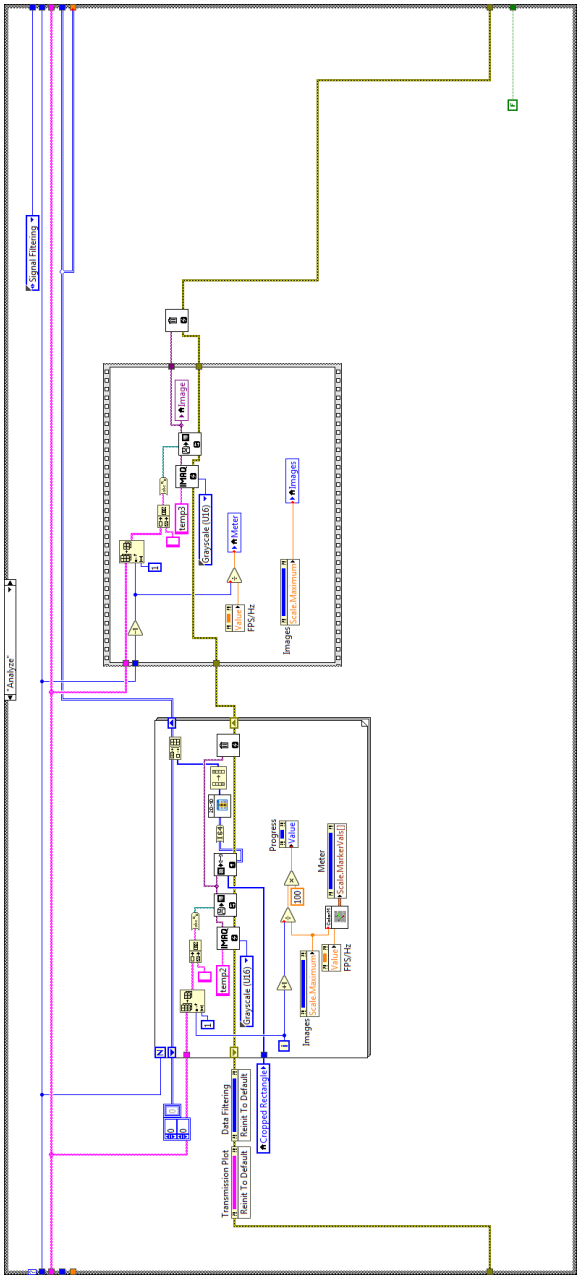

Transmission profiles extraction from images.

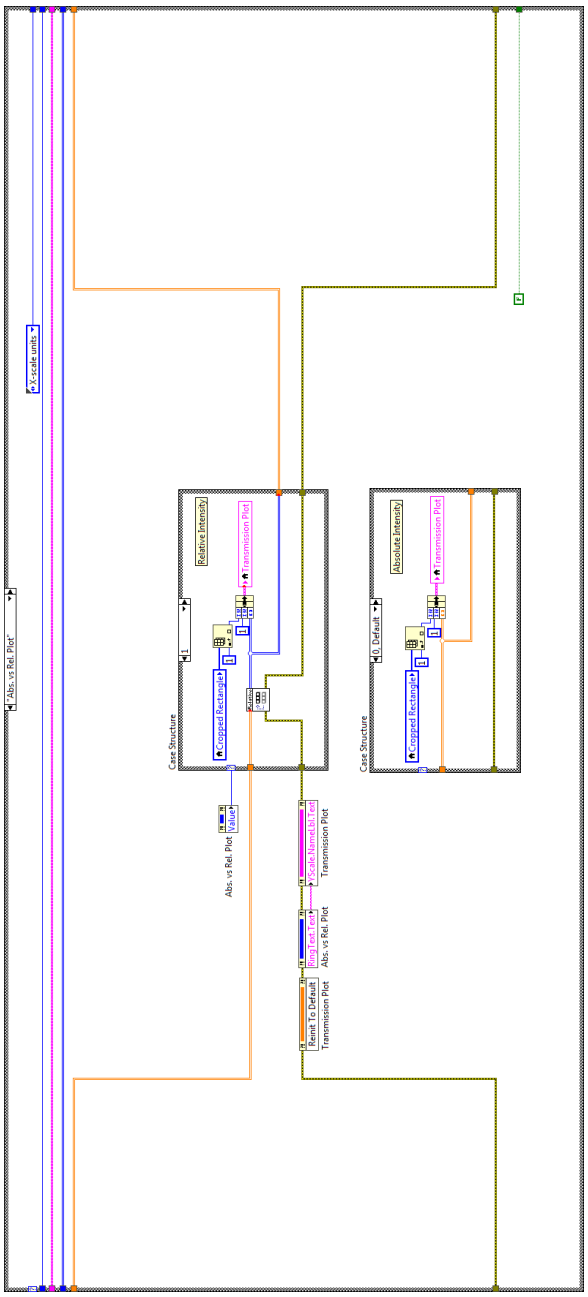

Switch between absolute and relative transmission profiles.

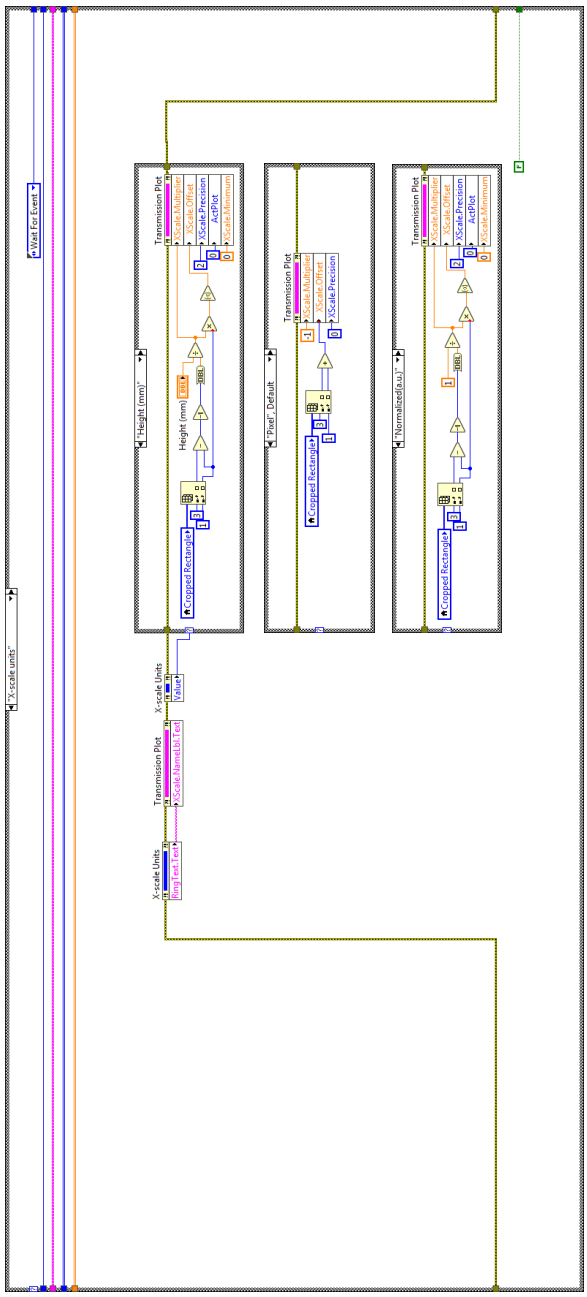

Change x-scale units of transmission profiles between normlized, mm, and pixel.

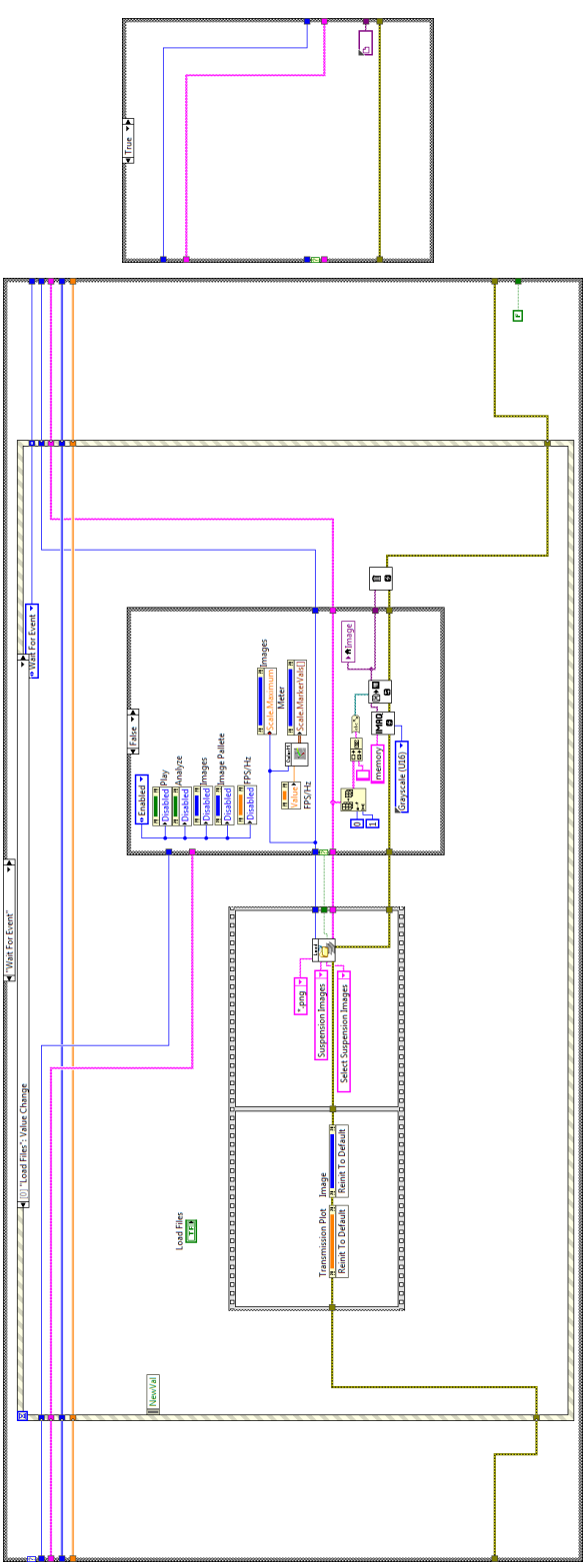

State machine infrastructure. Load image files when corresponding button is clicked.

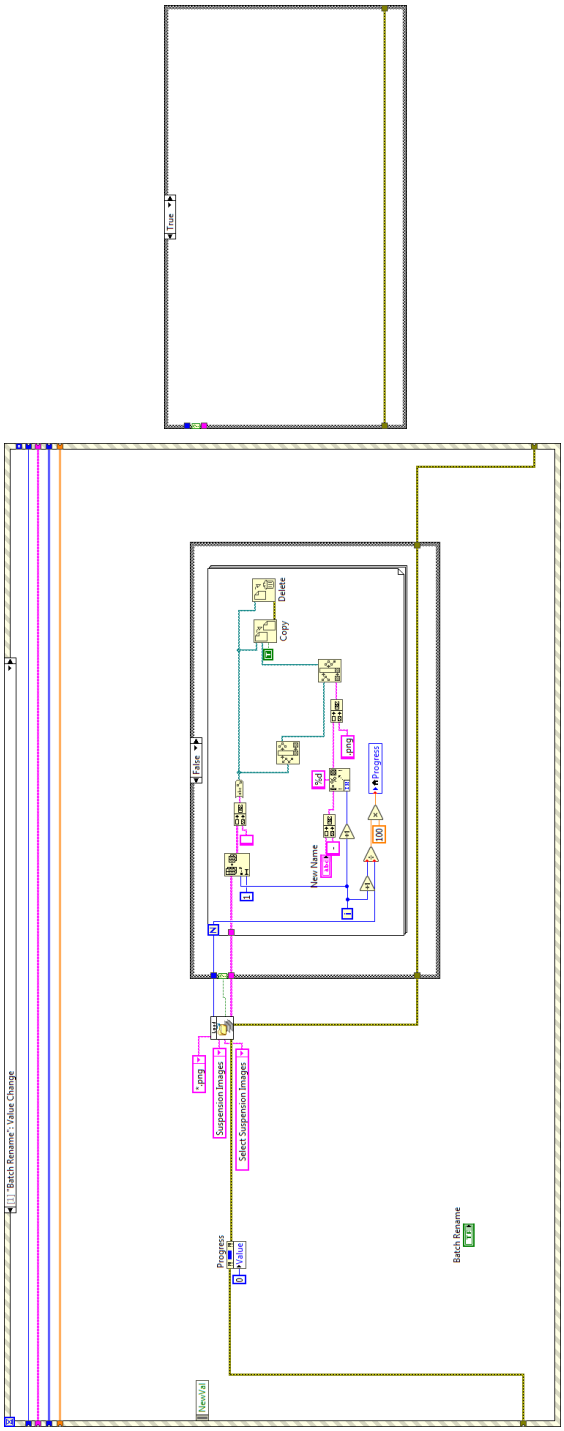

Batch rename selected image files to preset names for subsequent analysis.

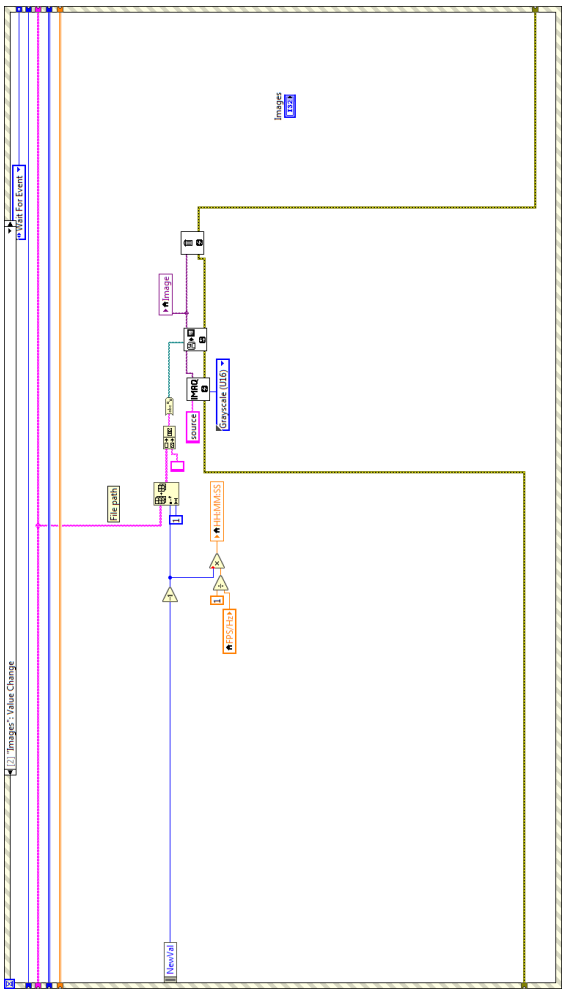

Select which of the loaded images to show in the display window.

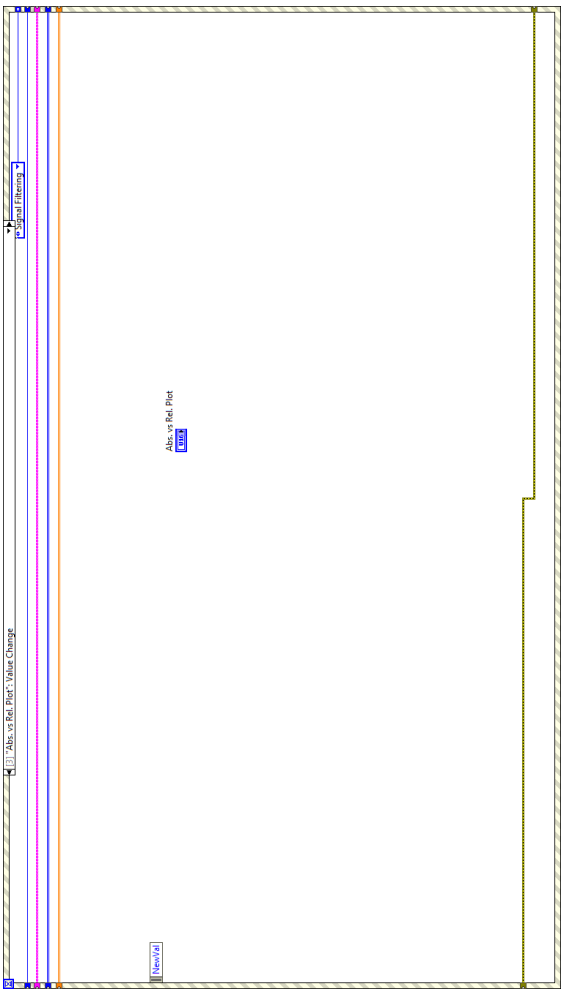

Capture an event when a different y-unit is requested for the transmission profiles.

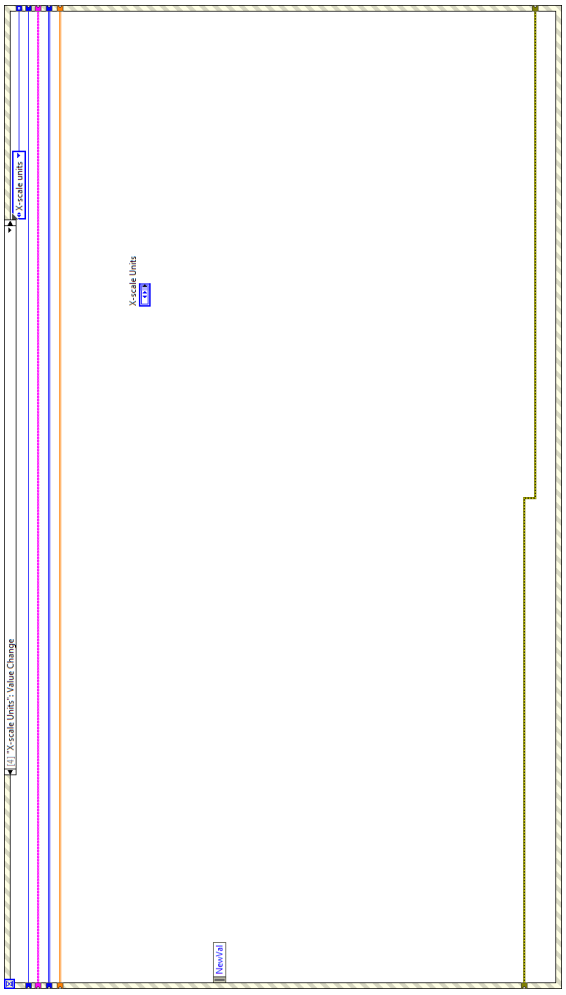

Capture an event when a different x-unit is requested for the transmission profiles.

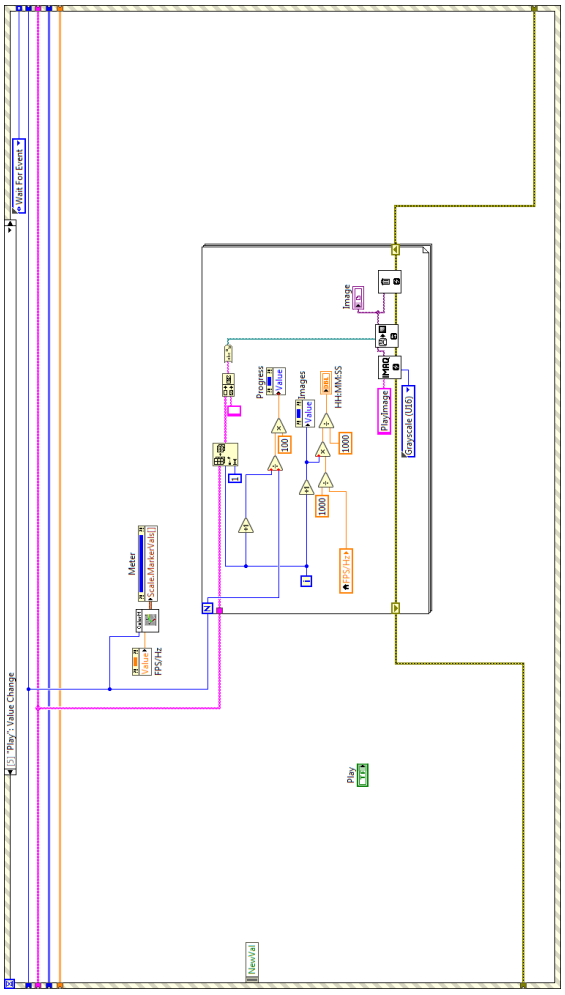

Play through the loaded shadowgraphic images.

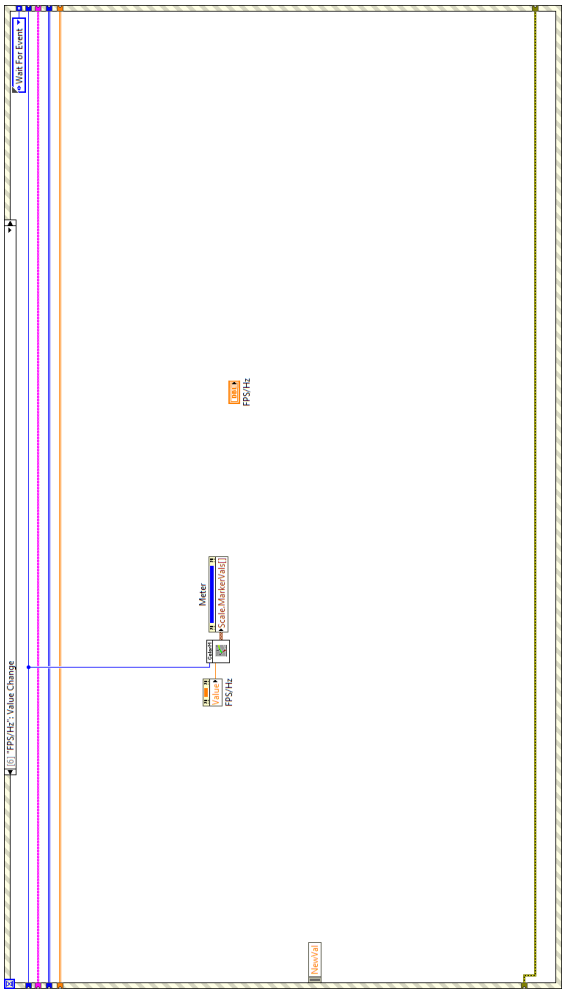

Change the displayed frame rate on Image Process tab to match the acquision setting.

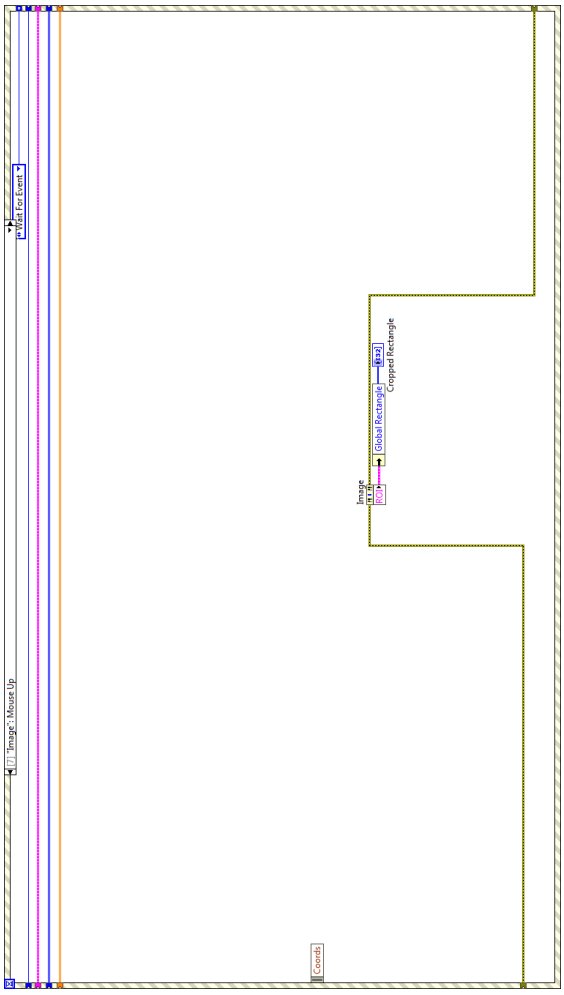

Draw a rectangular region of interest on the dislayed image.

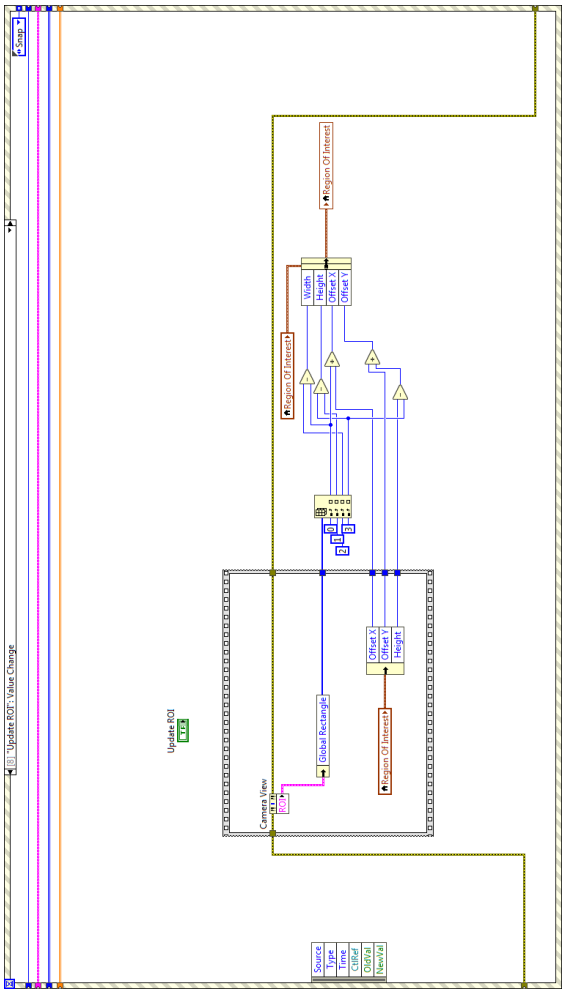

Update the camera view to match the drawn regtangular region of interest.

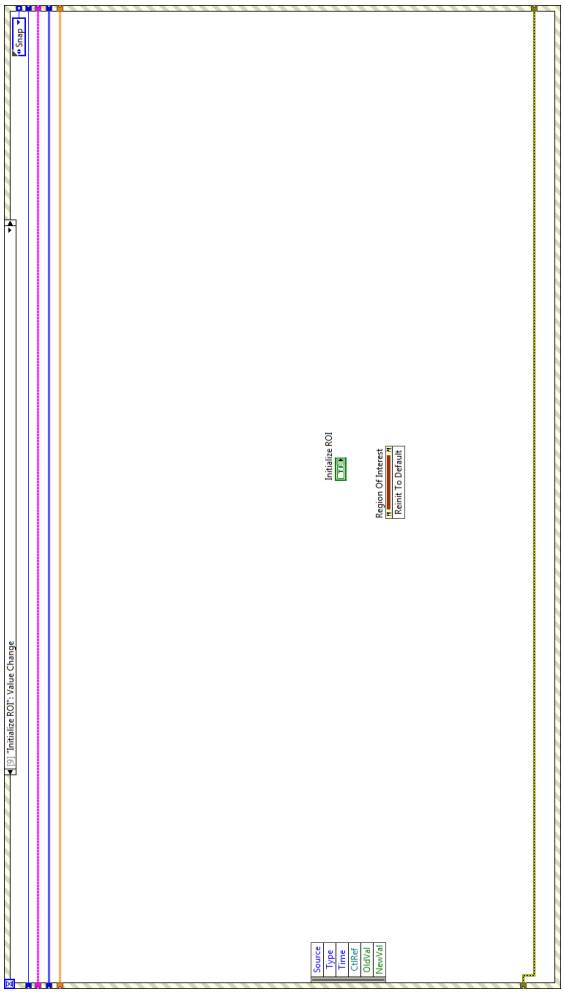

Reset the camera view to its full sensing area.

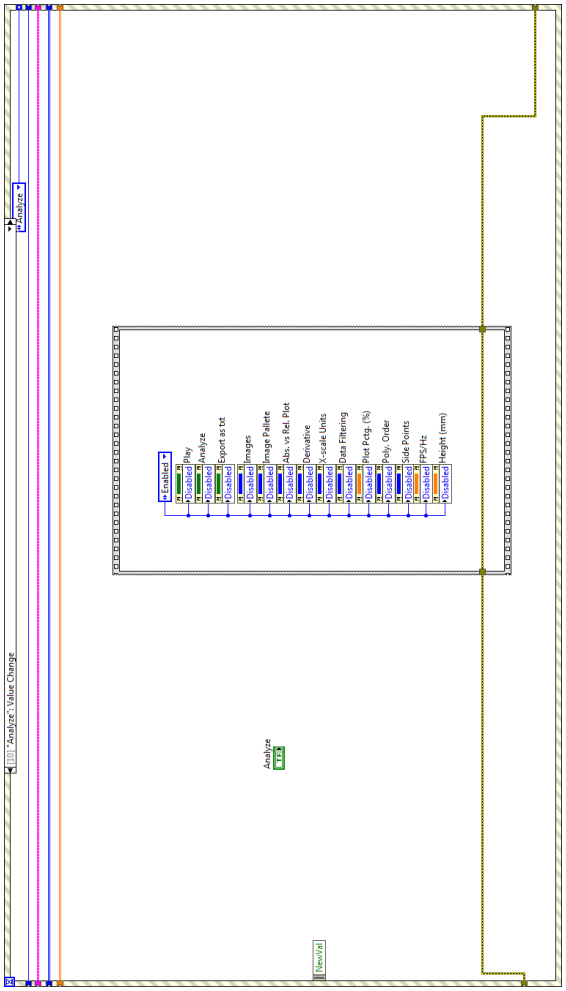

Capture an event when data analysis is requested for the loaded images.

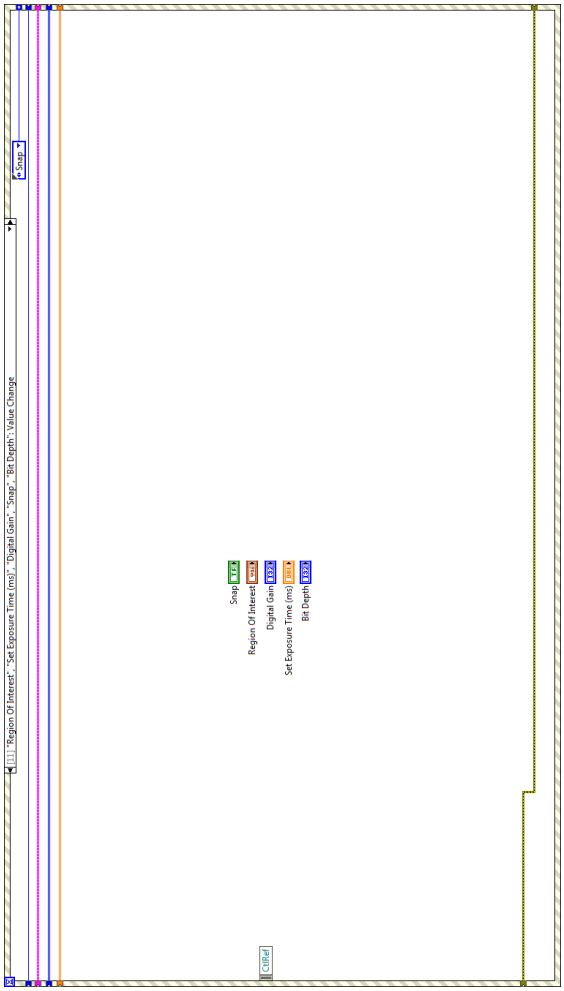

Snap a image when Snap is clicked or any settings of the camera including ROI, gain, exposure tike, and bit depth, are changed.

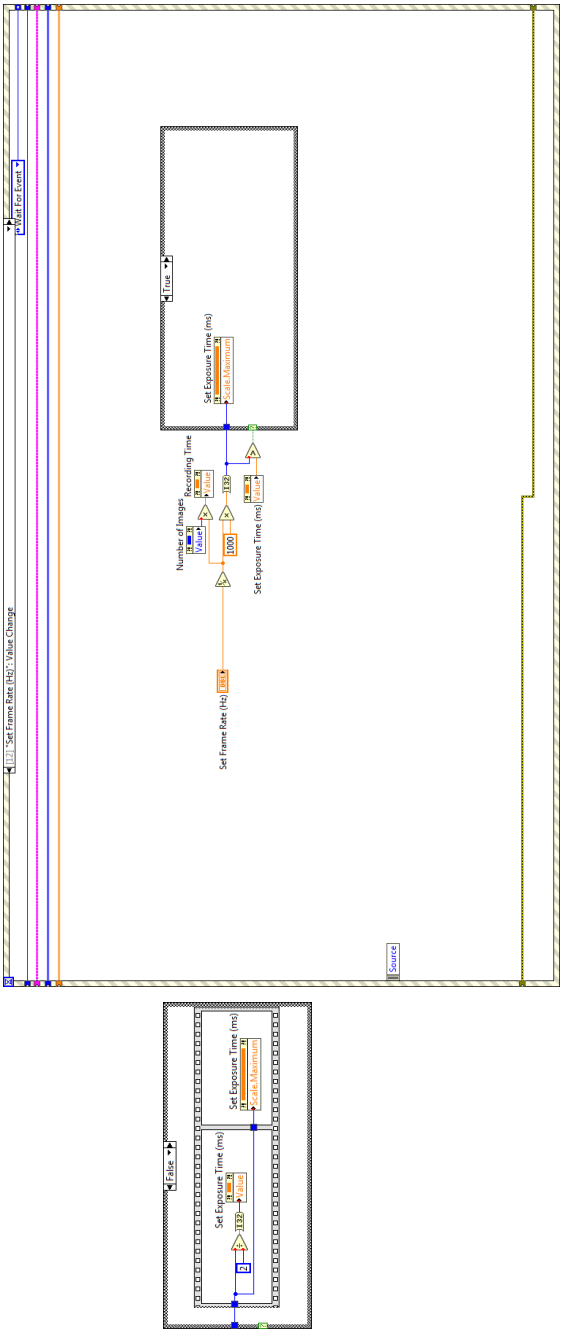

Set the frame rate to acquire shadowgraphic images.

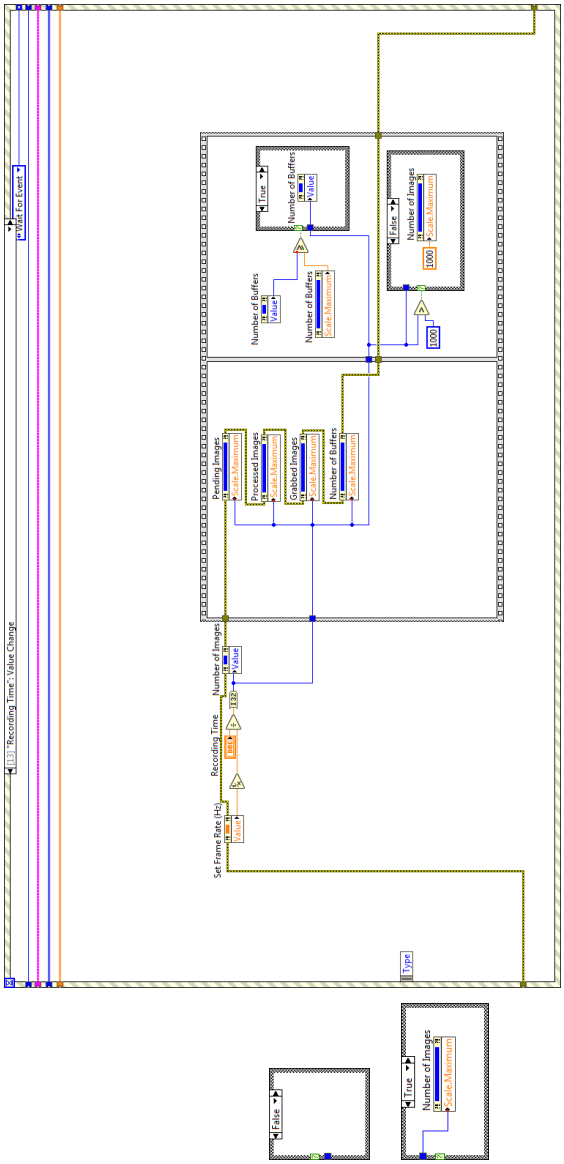

Set the recording time and calculate the corresponding number of images and frame rate.

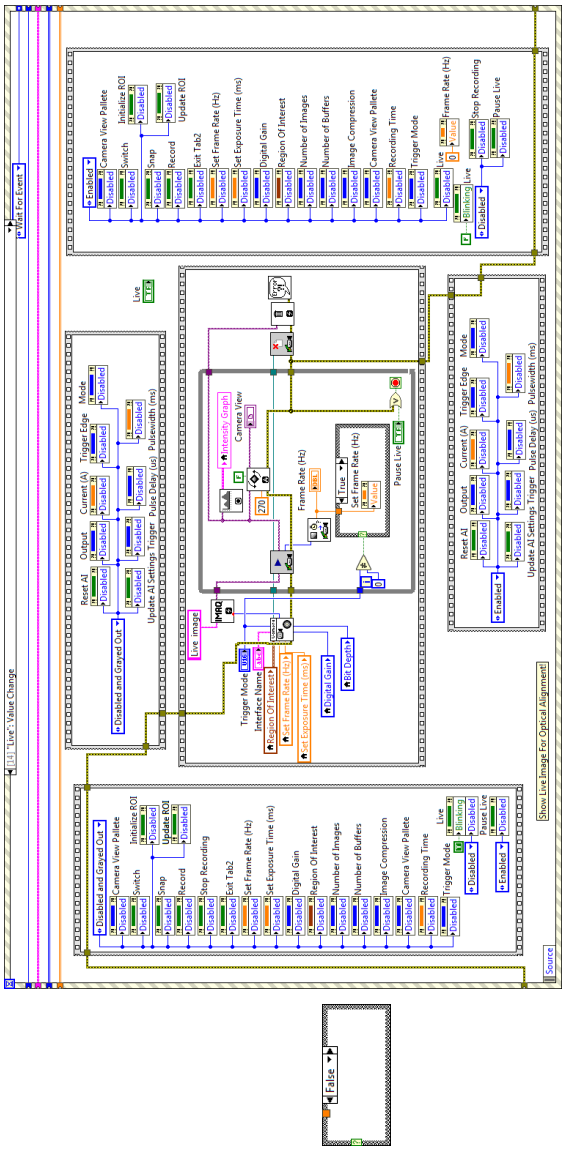

Acquie live view of the camera using current settings.

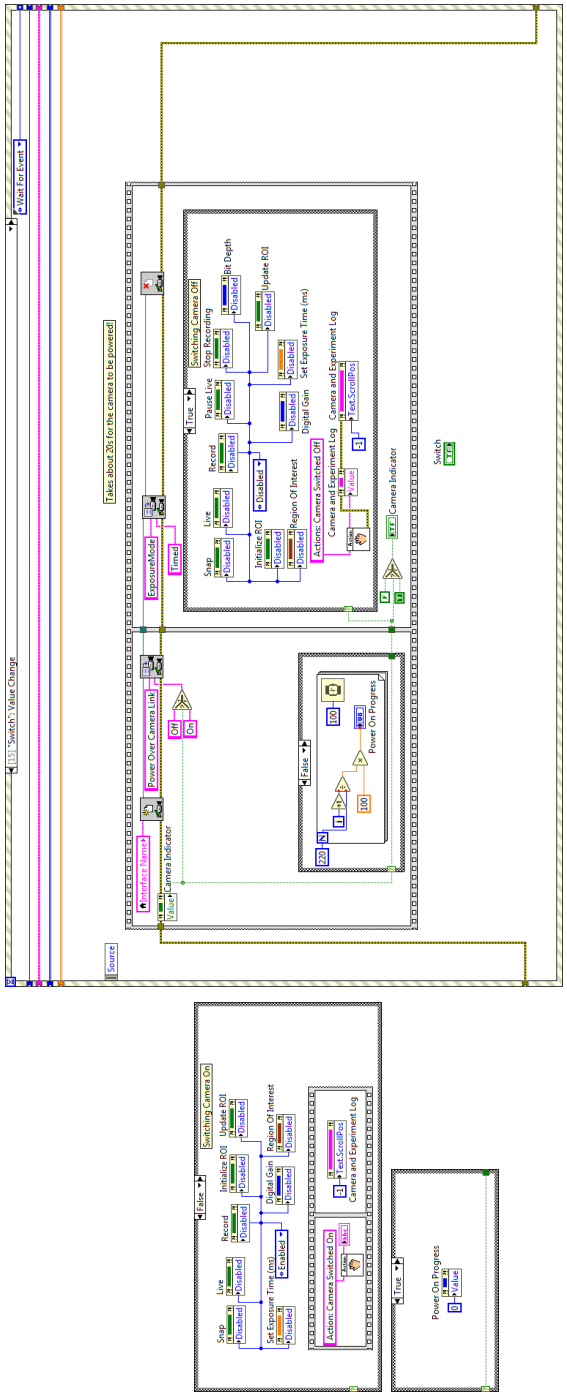

Switch on and off the camera.

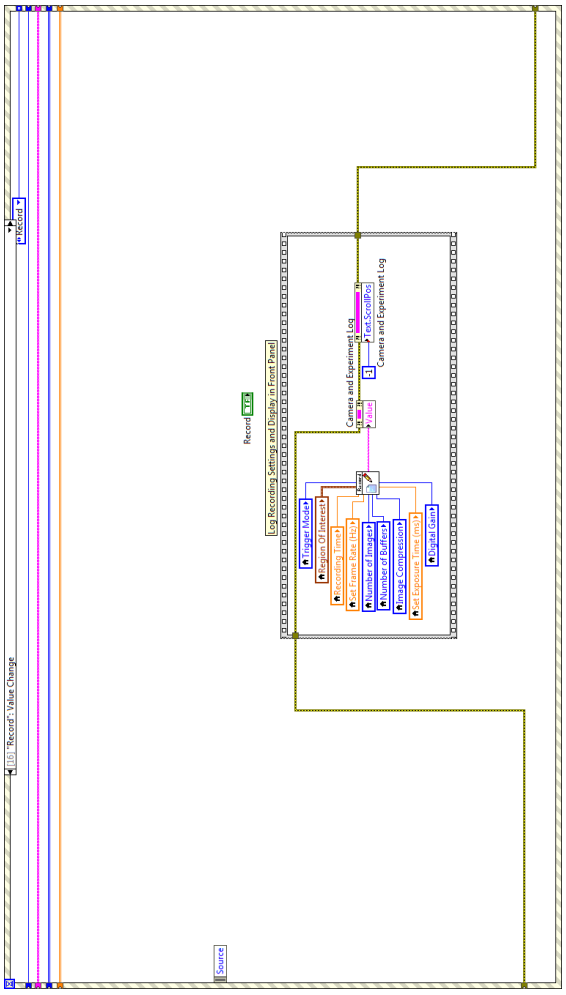

Start recording shadowgraphic images using the current camera settings.

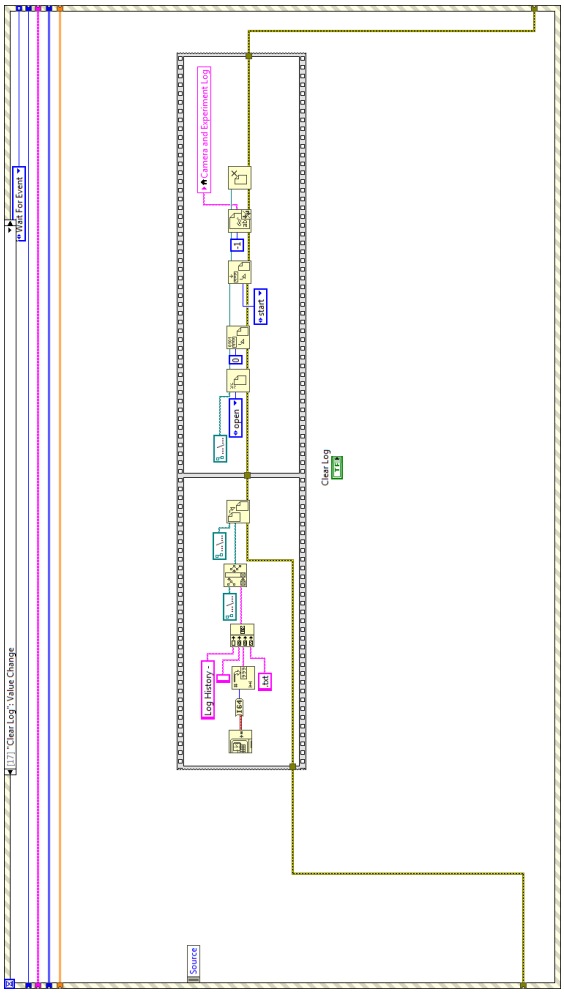

Reset event log window.

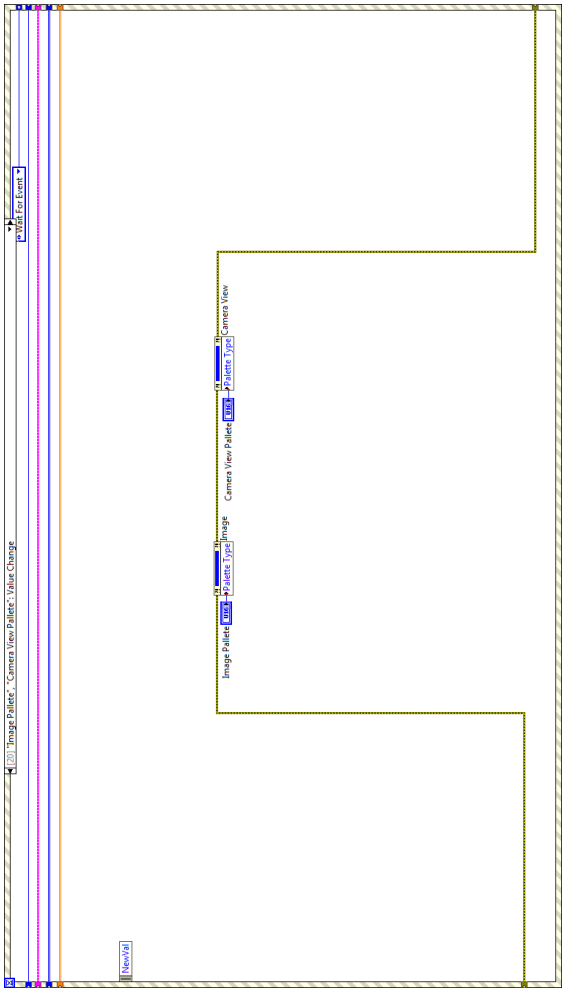

Change the Pallete used to display the acquired images.

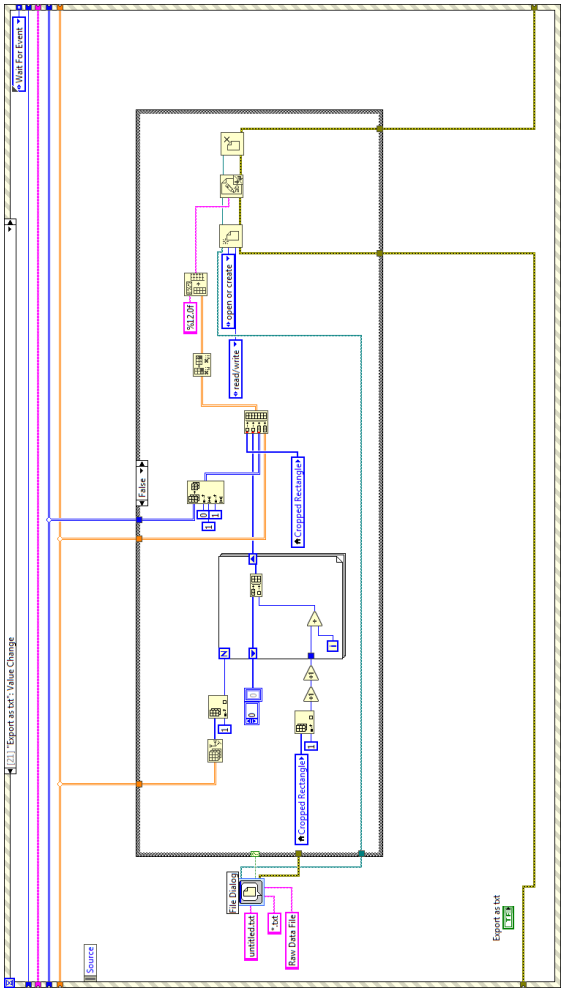

* Empty "True"

Export raw data of transmission profiles to a text file for post analysis.

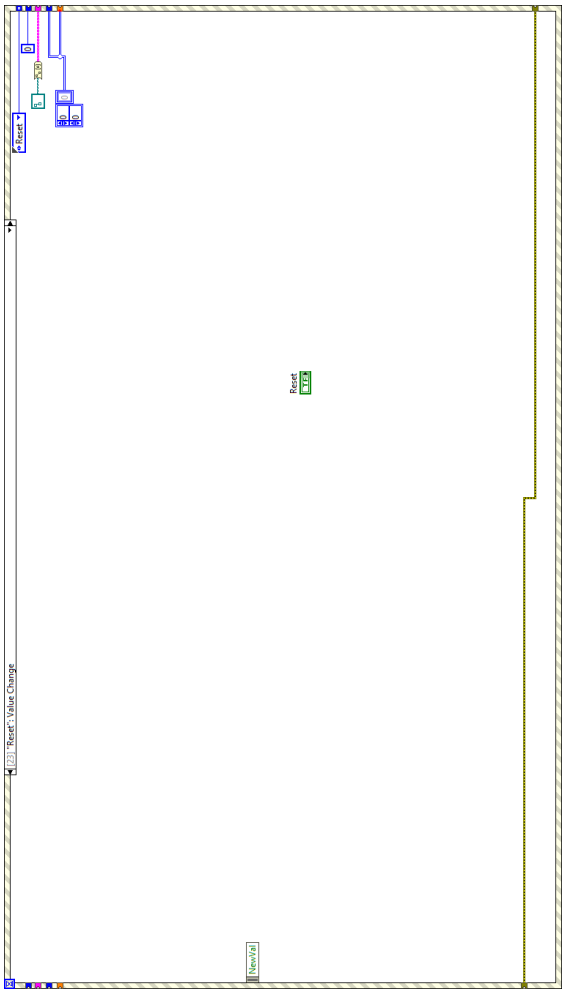

Capture reset event and initialize the software settings.

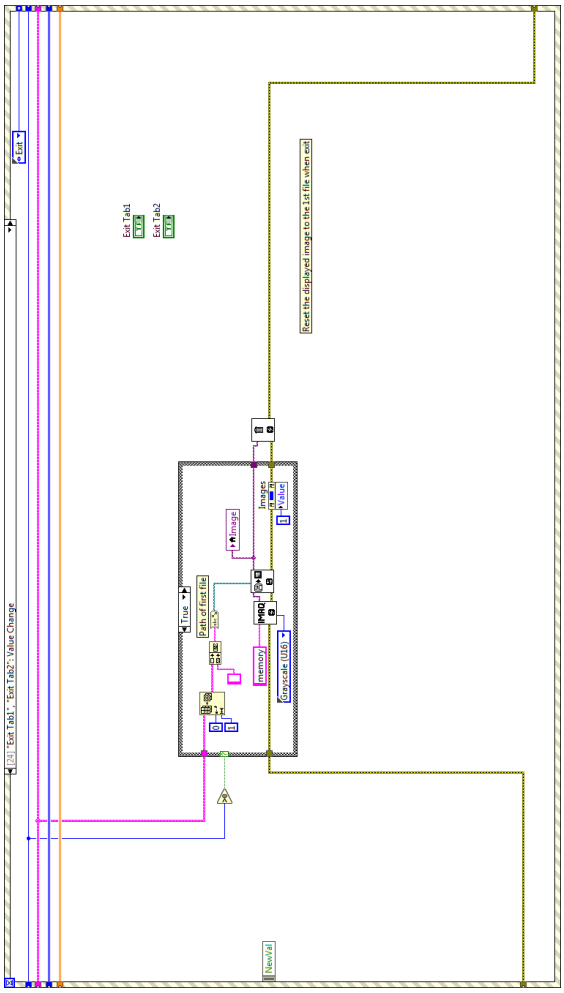

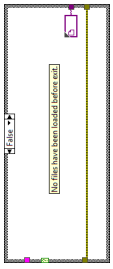

Exit the software.

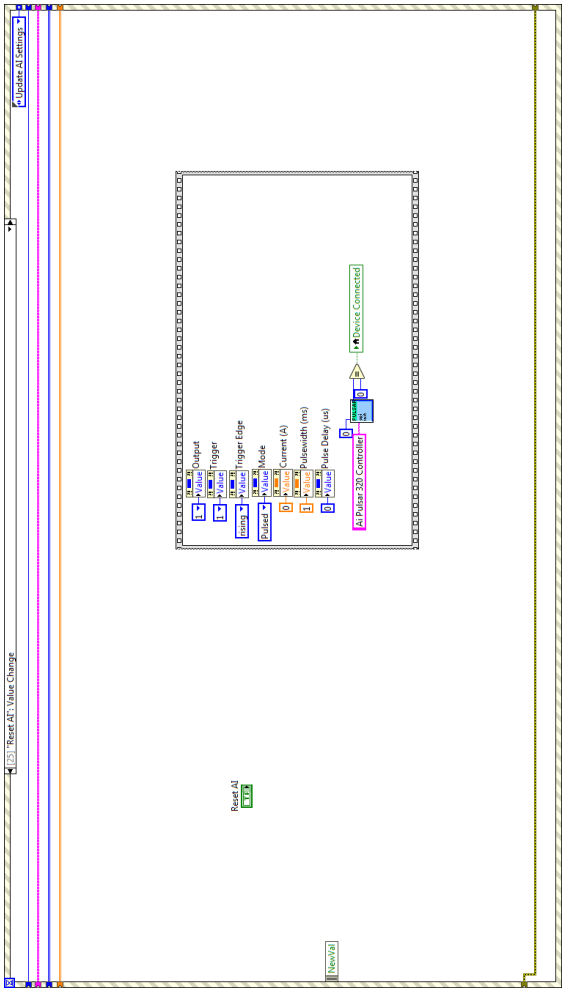

Reset the settings of the LED panel to their default values.

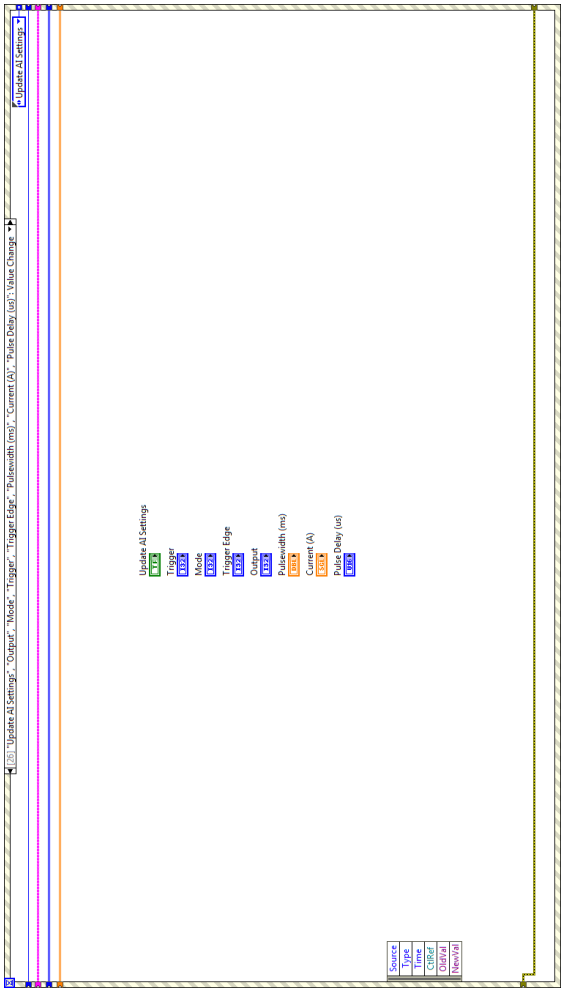

Update the settings of the LED panel when changes are detected.

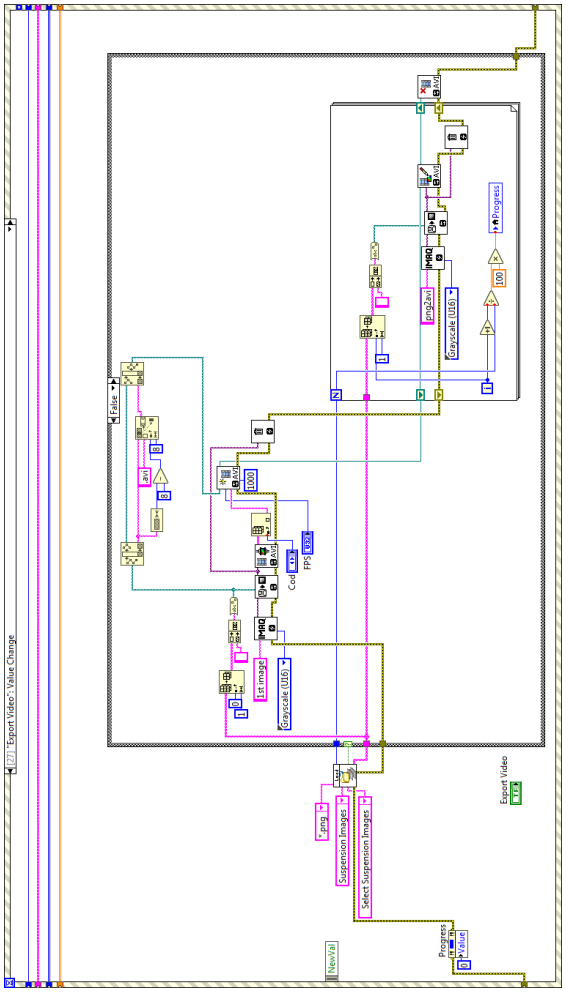

* Empty “True”

Convert sequential images to videos for subsequent presentation.

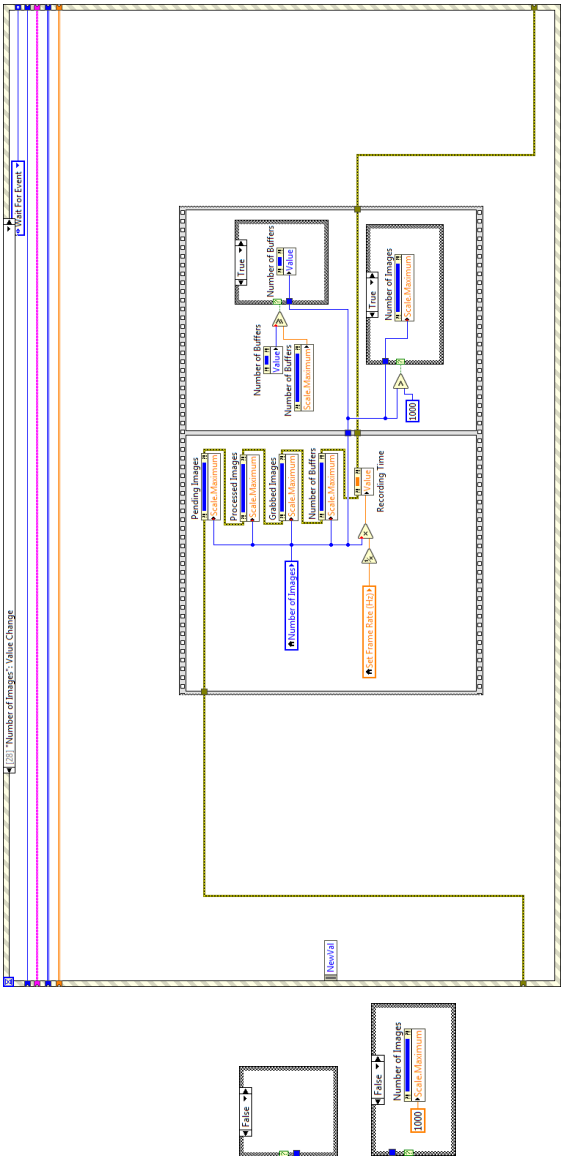

Set the number of images to acquire for a measurement.

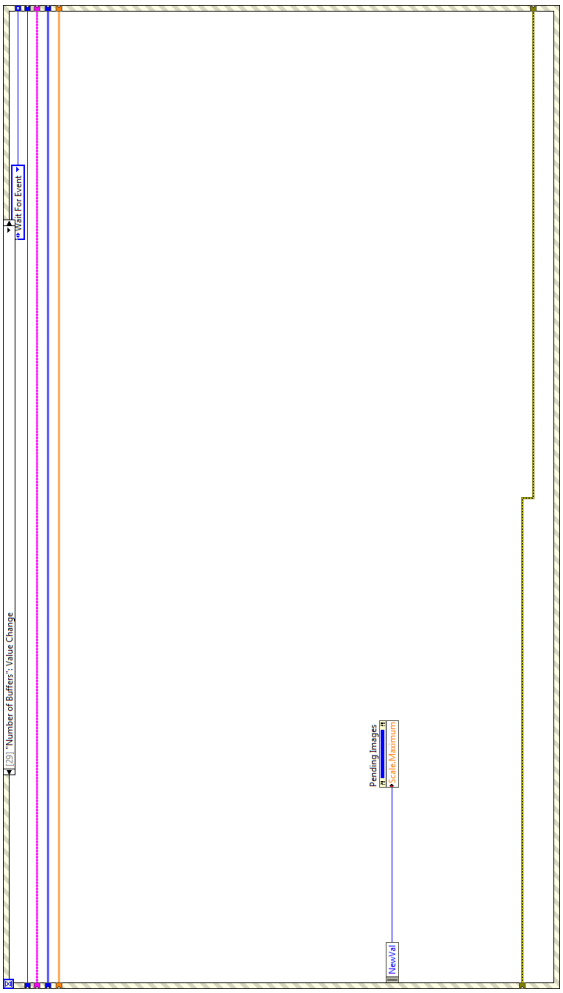

Set the number of buffers to store temporary files generated.

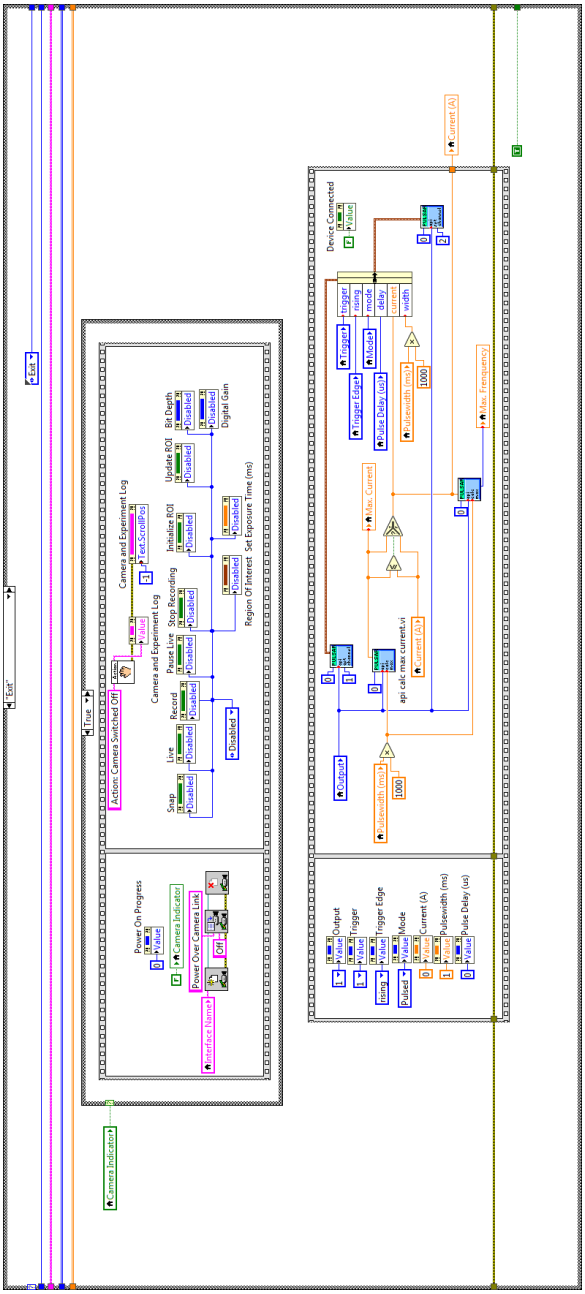

* Empty “False”

Reset LED and camera settings to their default values before exiting the software.

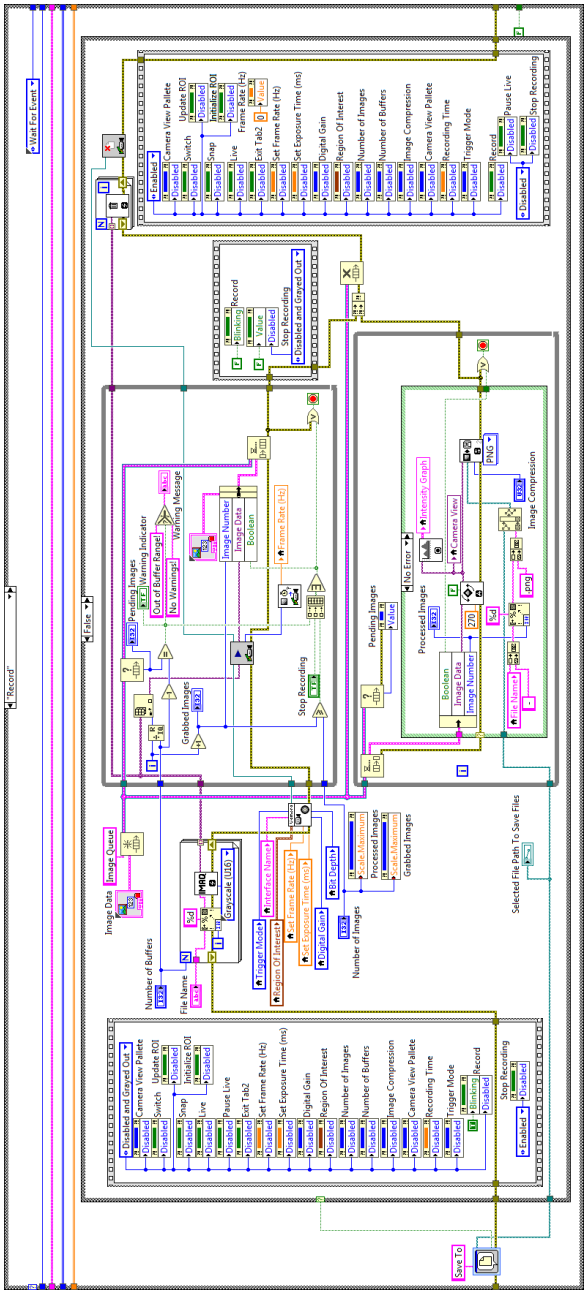

* Empty “Error” and “True”

Record shadowgraphic images using current LED and camera settings.

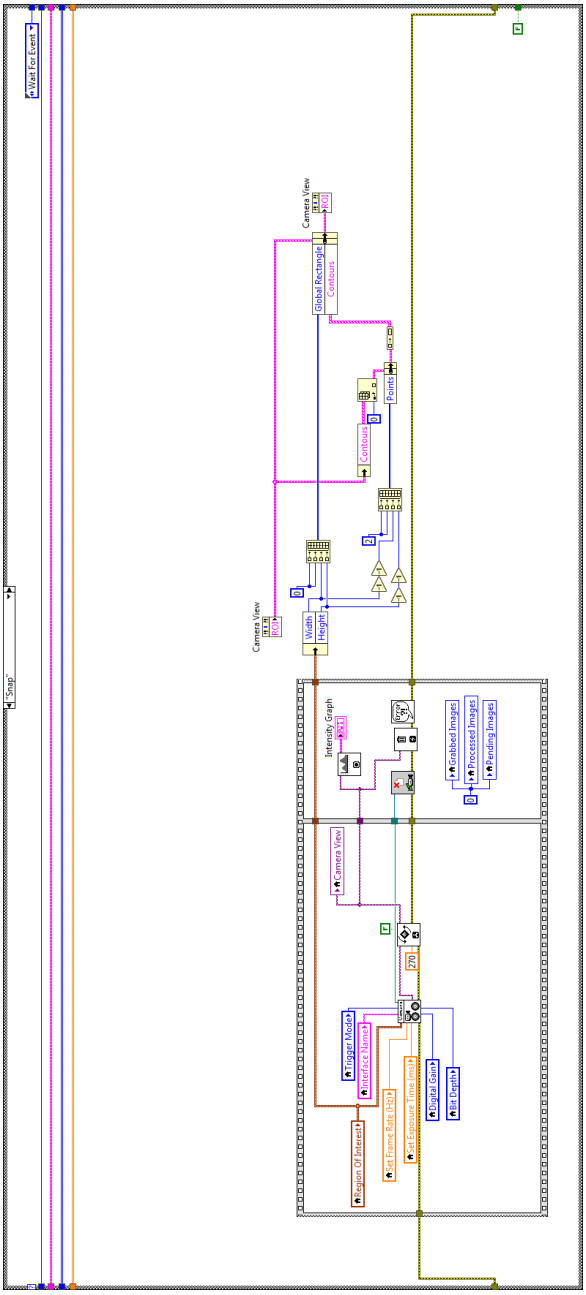

Snap a image of the current camera view using current settings.

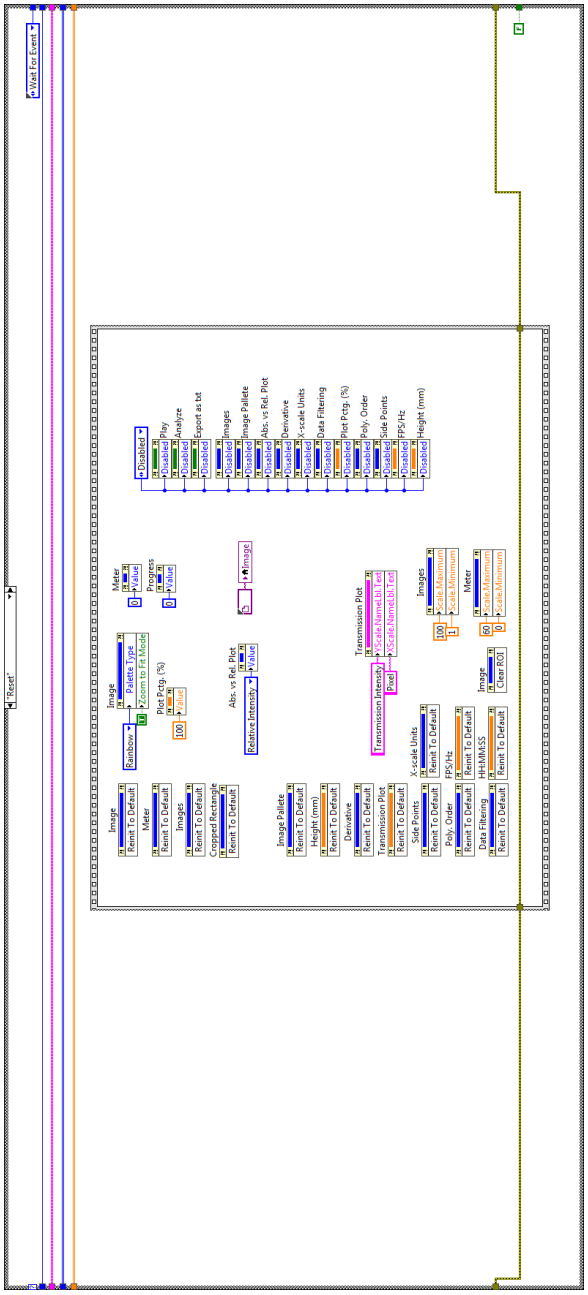

Reset all settings and initialize.

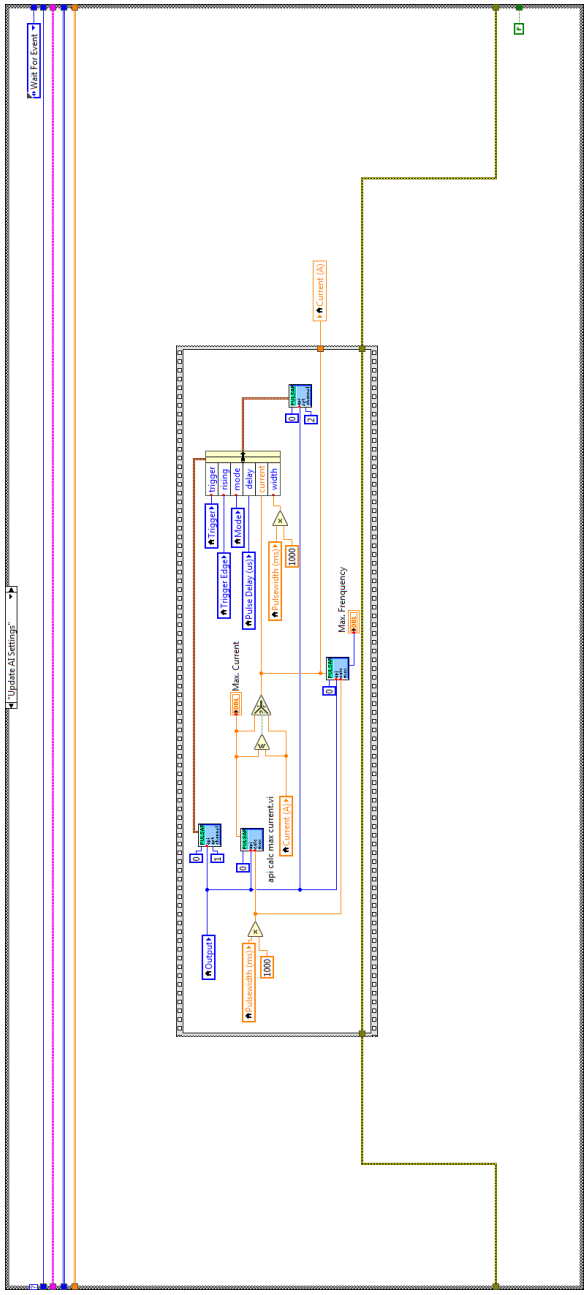

Update the settings for the LED panel.

V.3. Post-data processing

A SI_Data_Analysis software written in MATLAB (MathWorks, Inc., MA, US) was used for further refined post-data processing to produce the transmission profiles and instability indices introduced in CHAPTER 2, as its front panel shown in **Figure V.5**. The three instability index plots in **Figure V.3** stand for the samples used in CHAPTER 3 with monodisperse lactose suspended in HFA134a after three different agitation methods, wrist action shaking, vortex mixing, and ultrasonic agitation. Most of the produced instability index plots can be well-fitted using a hill function as introduced in **Eqn. (3.1)**. Three parameters, σ_{Max}, n, and k, are obtained after a successful fitting.

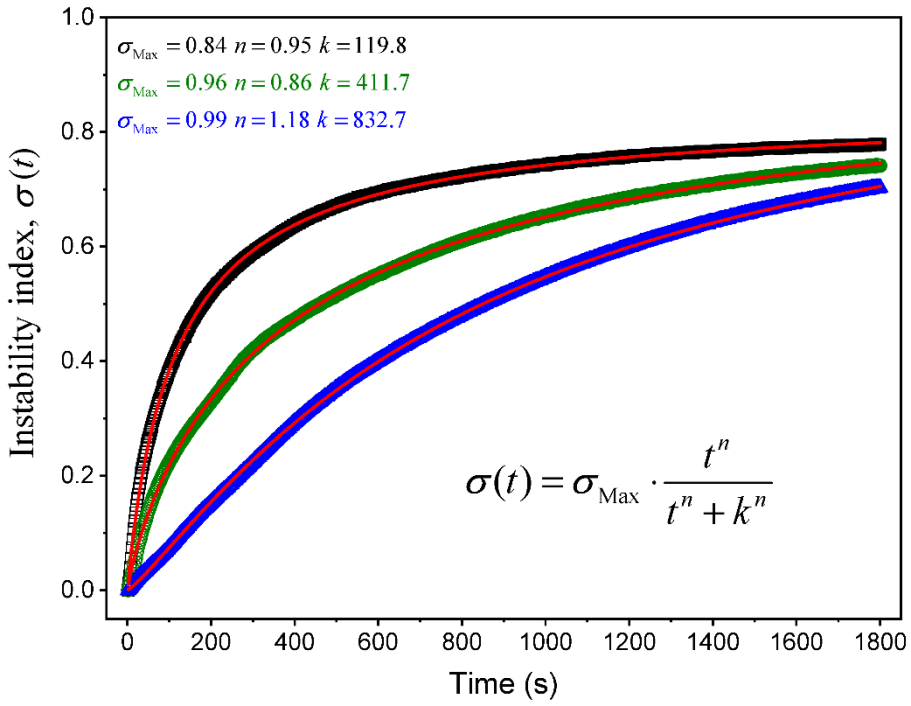

Figure V.3. Fitting of the instability index plots with a hill function. The red fitting curves overlap very well with the measured instability index data points.

Based on the hill function, σ_{Max} is the predicted maximum instability index, k is the time it takes for the instability index to reach half of the predicted maximum instability index since $\sigma(t=k)=0.5\sigma_{Max}$. According to the simulated plots of hill functions and their derivatives shown in **Figure V.4**, n determines the slope and shape of the increasing instability index plots that lower value corresponds to earlier initiation of the destabilization process as indicated by the larger slopes. It should be noted that the fitting parameter σ_{Max} has a theoretical upper limit of 1.0. For similar suspensions, the value of n is usually close to 1 and shows no significant differences, while the value of k provides a single time constant that can be used to differentiate different samples. The time constant, $\tau(\sigma=0.5)$, used in CHAPTER 3 for comparing the colloidal stability of multiple samples is defined similarly. The hill function fitting can prove useful for cross-sample comparison and predicting the destabilization trend of samples.

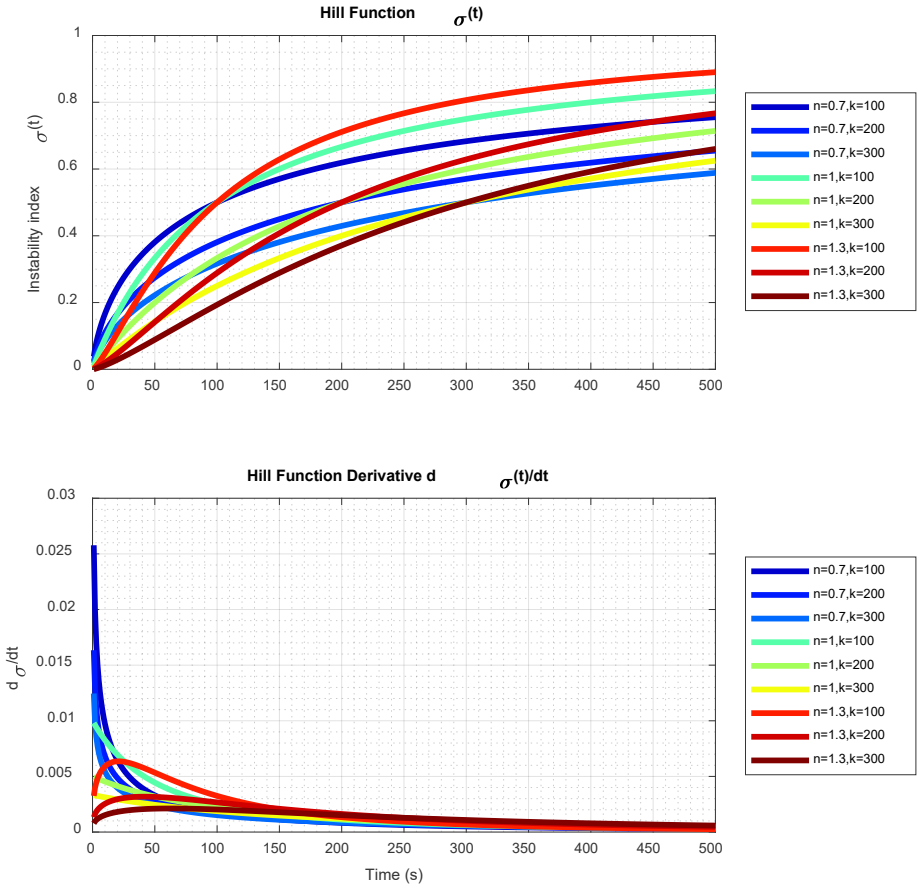

Figure V.4. Fitting parameters of the hill function.

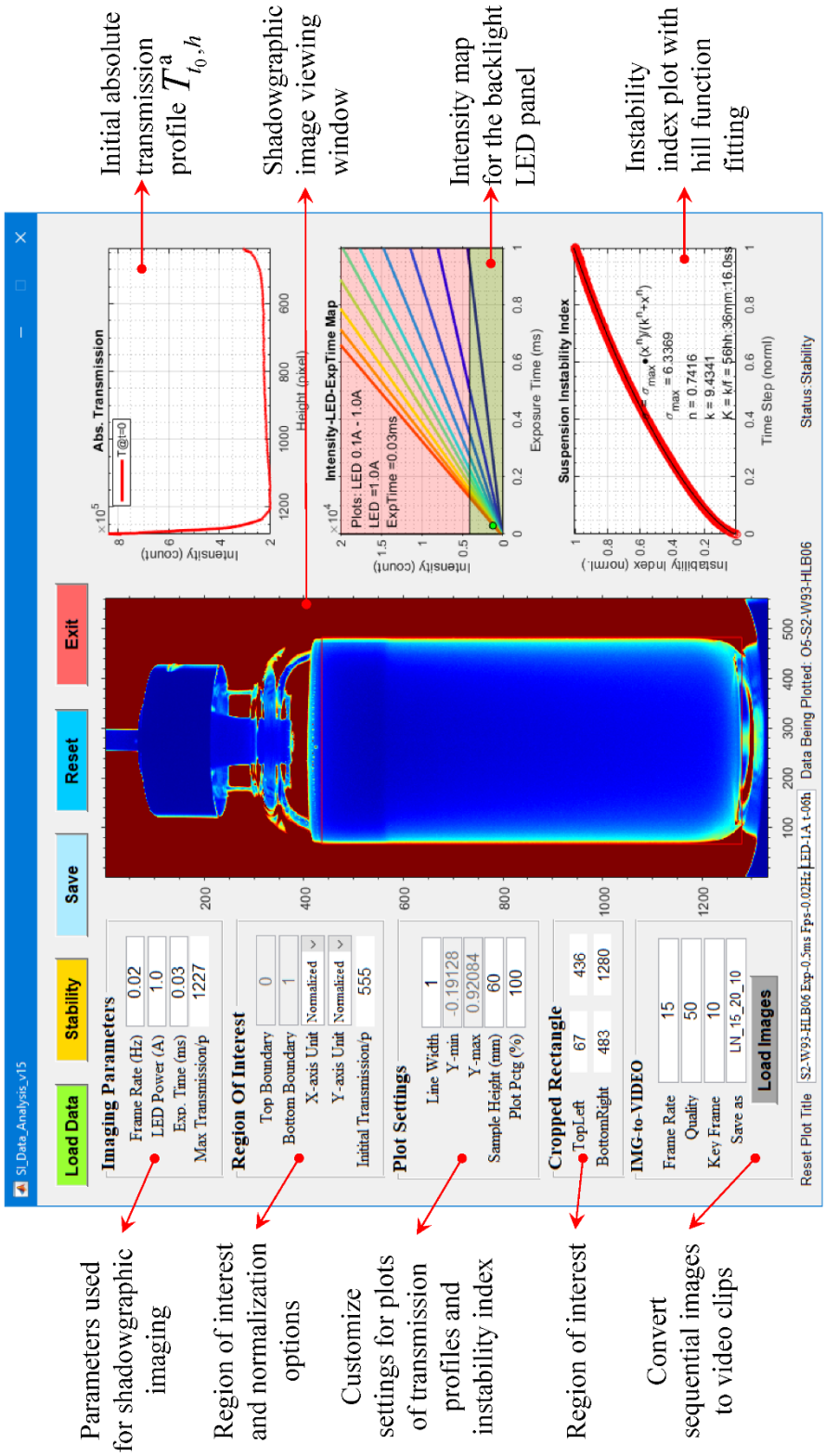

Figure V.5. The front panel of the SI_Data_Analysis GUI code for post data processing.